博士論文

論文題目　Electronic Control of Transport Properties at Oxide Interfaces

（酸化物界面における輸送特性のキャリア制御）

氏　名　李　智蓮

Electronic Control of Transport Properties at Oxide Interfaces

Jiyeon N. Lee

Supervisor: Professor Mikk Lippmaa

Department of Advanced Materials Science
Graduate School of Frontier Sciences
The University of Tokyo

July 2020

Contents

Chapter 1

Introduction

1.1 General introduction

Oxides are a very widely studied class of compounds. The bulk properties of various oxide materials are made use of in many electronic applications. In physics, the study of the electronic behavior of transition metal oxides goes back a century to the seminal works of Verwey, Peierls, Mott, and others that lay the foundations of what we know today as the research field of correlated electron systems.

1.2 Strongly correlated transition metal oxides

Transition metal oxides are good model systems for studying electron correlations [1]. In a transition metal oxide lattice, the nearest neighbor of a transition metal is always an oxygen atom. In the ionic metal-oxygen bonds, the *s*-electrons of the transition metal are transferred to the oxygen ions, and the remaining *d* electrons determine the physical properties of the material. Electrons in the nearly core-like, spatially confined *d*-orbitals are strongly influenced by filling-dependent electron correlation effects. In these materials, primarily the partially filled *d* shells are therefore responsible for the rich physical properties. Famous examples among transition metal oxides are manganites, ruthenates, and cuprates, where fascinating electronic phenomena such as colossal magnetoresistance, Mott transitions, and high-temperature superconductivity appear, respectively. A new field of research, known as "oxide electronics", has arisen to make use of these interesting physical properties or behavior in new functional devices. Rich phase diagrams appear when the *d*-band filling is systematically varied,

as shown in figure 1.1 [2].

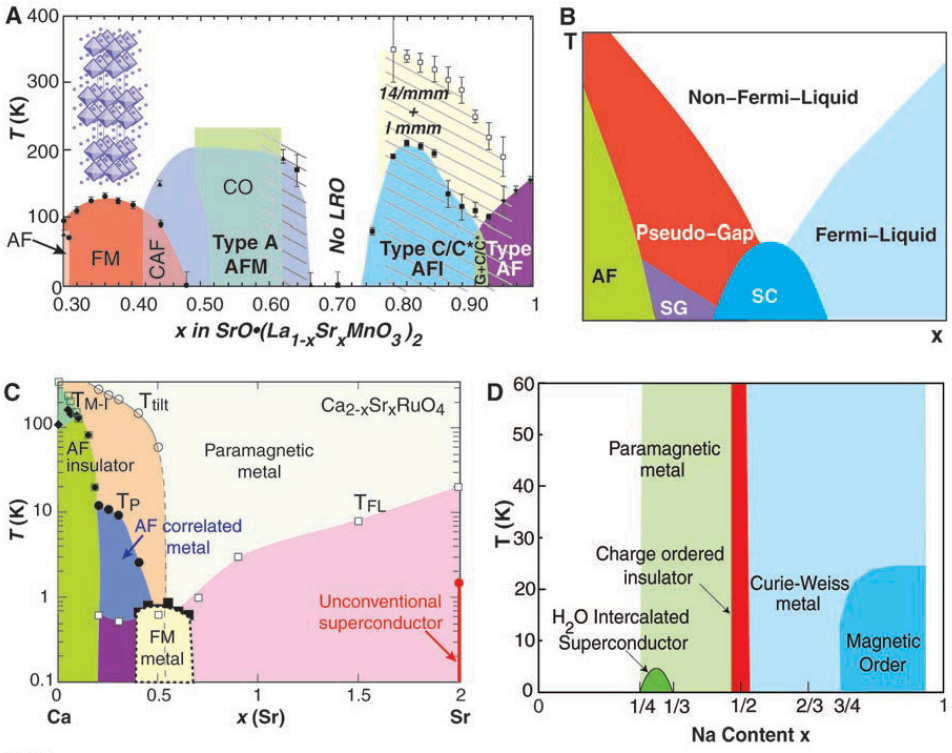

Figure 1.1: Phase diagrams of representative materials from the family of strongly correlated electron systems [2]. (A) Temperature versus hole density phase diagram of bilayer manganites [3]. (B) Generic phase diagram of high-T_c superconductors. (C) Phase diagram of single-layer ruthenates [4, 5], (D) Phase diagram of cobalt oxides [6].

1.3 Layered oxide structures and artificial interfaces

Many of the unique properties of oxides are related to the layered nature of the crystal structures, especially for ternary and more complex oxide phases. With the help of modern thin film growth techniques that allow the structure to be grown one atomic layer or block at a time, the available structure space can be enriched with artificially grown thin film heterostructures where different materials are stacked either in single aperiodic interfaces or in repetitive interfaces of superlattices. This technique is the key to systematic studies of two-dimensional oxide structures.

Among transition metal oxides, perovskites are often the starting point of designing

new artificial structures. Perovskites are special, because of the high structural stability of the octahedrally coordinated transition metal complex. Due to this, perovskites can be constructed out of a very broad combination of elements, tuning either the d-band filling, bond angles or crystal field splitting, but regardless of the variety of elements that can be used, the pseudocubic lattice parameter remains close to 4Å. This means that it is often possible to combine different perovskites in epitaxial heterostructures, essentially creating new artificial lattices.

A similar process may also occur naturally, for example in the Ruddlesden-Popper type lattices with interleaved rocksalt AO and perovskite ABO_3 layers, creating a series of compounds with a general formula of $A_{n+1}B_nO_{3n+1}$, where the A site is usually occupied by a rare-earth or alkali metal ion, and the B site holds a transition metal atom.

Another spectacular group of materials is the family of cuprate high-temperature superconductors, the structure of which is also based on perovskite-like blocks. Perhaps the best-known representative of this group is $YBa_2Cu_3O_7$(YBCO) (Fig. 1.2), the first superconductor with a superconducting transition temperature, T_c, that exceeds the boiling point of liquid nitrogen.

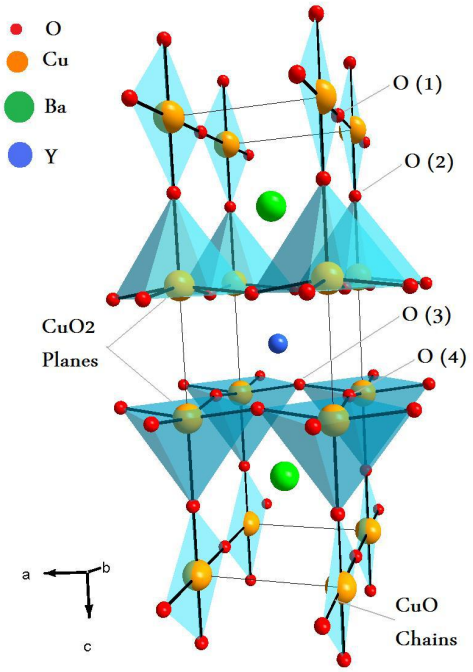

Figure 1.2: $YBa_2Cu_3O_7$ unit cell[7].

The YBCO unit cell consists of a stack of three perovskite unit cells, leading to a *c*-axis lattice parameter of close to 12 Å. There is thus a fine balance between thermodynamically stable 'bulk' phases that can form naturally, and the possibly thermodynamically metastable 'heterostructure' phases formed in a thin film growth process. The heterostructure approach to materials design and study is, of course, important from the point of view of functional devices, such as field-effect transistors, but artificial heterostructures also allow us to isolate individual layers or combinations of layers, which would not be possible in bulk single crystals. In the case of YBCO, for example, it has been shown that Y in the mirror plane at the center of the unit cell is essentially a spacer between two superconducting CuO_2 planes, while the partially oxygen-deficient Cu-O chains control the carrier density and the crystal symmetry through chain-line vacancy ordering [8].

In this sense, a thin film study of artificially designed heterostructure offers a great opportunity to explore the physics of transition metal oxides. Even the most familiar oxides show unusual but occasionally technologically useful electronic and magnetic properties when different materials are stacked up into heterostructures, allowing for systematic studies of two-dimensional oxide structures. The interplay among the electronic degrees of freedom leads to novel emergent phenomena (Fig. 1.3), which are enhanced both by the broken spatial inversion symmetry of the structure itself, and the electron correlations in the low-dimensional electronic systems that can form at interfaces.

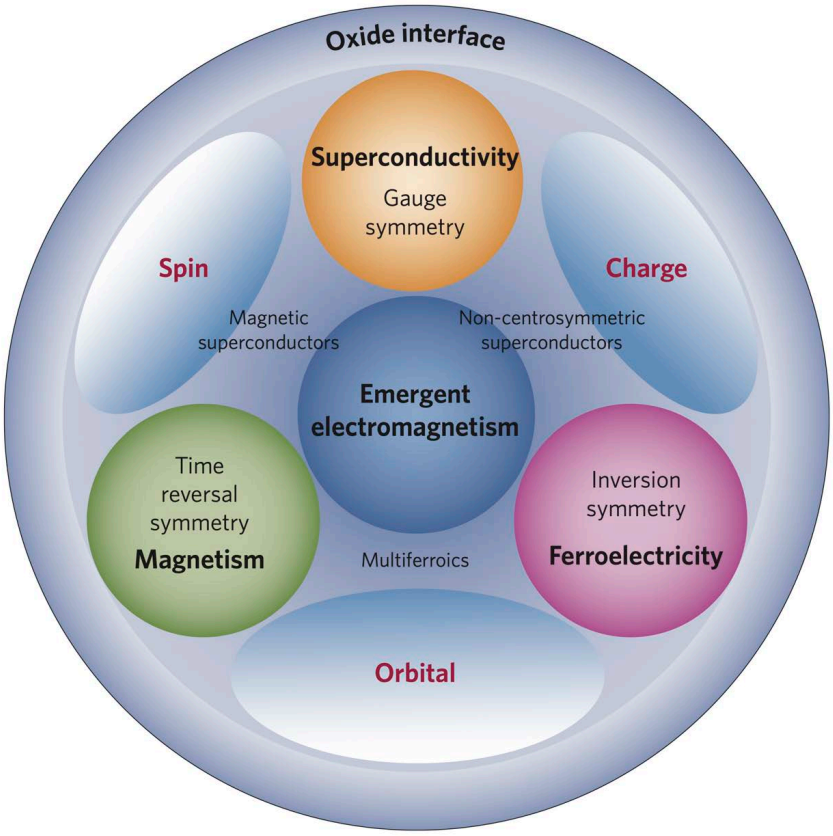

Figure 1.3: Schematic diagram showing the symmetries and degrees of freedom of correlated electrons that can be engineered at oxide interfaces [1].

1.4 Aim of this study

In this thesis work, I explore the transport behavior of carriers accumulated at an interface between two insulators, which, nevertheless, exhibits two-dimensional high-mobility conductivity. The starting point is the most famous perovskite oxide, $SrTiO_3$, which is nominally a d^0 diamagnetic, closed-shell, wide-gap insulator. The delta-doping layer consists of $LaTiO_3$, which dopes the $SrTiO_3$ at the interface by charge transfer. Theoretical studies have suggested that various magnetically ordered phases may exist at such interfaces, depending on a particular choice of model parameters [9, 10].

The main question thus is, if the predicted paramagnetic, metallic, or even ferromagnetic phases actually appear in the two-dimensional accumulation layers in $SrTiO_3$. This study tries to address some of the questions of basic interface physics and develop strategies for developing applications around oxide interfaces. An important aspect of the work is the ability of tuning the carrier density and the electronic phases in these heterostructures by applying an electric field or a magnetic field. Magnetotransport analysis is mainly used to try to find signatures of magnetism derived from the two-dimensional confinement of carriers at the interface.

This study will give a guide for constructing new functional heterostructures and devices. e.g., spin conversion and spin pumping devices from oxide heterostructure (Fig. 1.4).

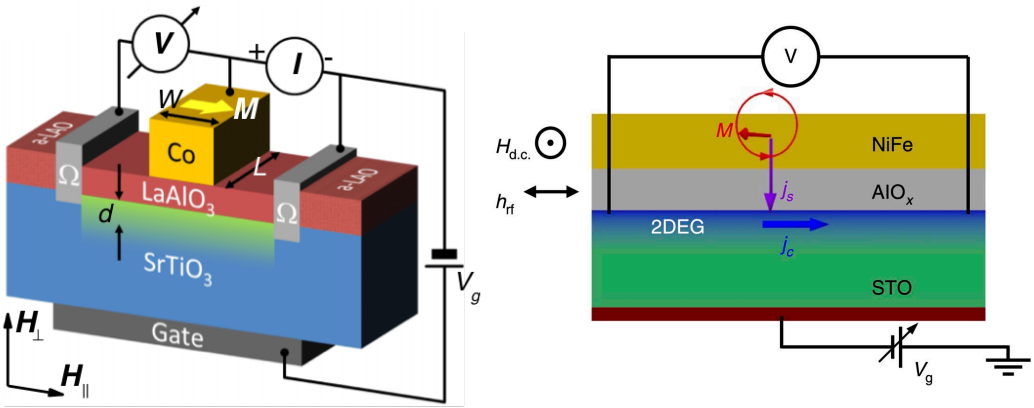

Figure 1.4: (Left) Sketch of the devices for 3-T Hanle measurements with the magnetic field applied perpendicular or parallel to the sample plane. A gate voltage V_g can be applied between the back of the $SrTiO_3$ crystal and the 2DES [11]. (Right) Sketch of the spin-pumping experiment (M is the magnetization) [12].

Chapter 2

Quantum well heterostructure design

2.1 Introduction

When a potential well is sufficiently narrow, and the effective mass of carriers confined by the potential well is sufficiently low, new discrete energy levels can form. A confined carrier system where these discrete energy levels are sufficiently separated in energy is called a quantum well.

The electronic states of quantum wells can be understood by solving the Schrödinger equation for the carriers in the potential wells created by the band discontinuities [13]. The Schrödinger equation in the well with finite energy barriers is,

$$-\frac{\hbar^2}{2m_b^*}\frac{d^2\psi(z)}{dz^2} + V_0\psi(z) = E\psi(z) \ , \tag{2.1}$$

where V_0 is the potential barrier and m_b^* is the effective mass in the barrier. The boundary conditions require that the wave function and particle flux must be continuous at the interface. This gives a series of even and odd parity solutions that satisfy

$$\tan(\frac{kd}{2}) = \frac{m_w^*\kappa}{m_b^*k} \ , \tag{2.2}$$

$$\tan(\frac{kd}{2}) = -\frac{m_w^*k}{m_b^*\kappa} \ , \tag{2.3}$$

respectively. Here, k is the wave vector in the well, given by

$$\frac{\hbar^2k^2}{2m_w^*} = E_n \tag{2.4}$$

and κ is the exponential decay costant in the barrier given by

$$\frac{\hbar^2\kappa^2}{2m_w^*} = V_0 - E_n \ . \tag{2.5}$$

Solutions of Eq. 2.2 and Eq. 2.3 lead to the wave functions which are nearly sinusoidal inside the well, but decay exponentially in the barriers. The wave functions of the $n = 1$ and $n = 2$ levels are sketched in Fig. 2.1(left). Although this model is very simplified, it provides a good starting point for understanding the general properties of quantum confinement. For example, the confinement energy is inversely proportional to the effective mass, which means that lighter particles experience larger effects.

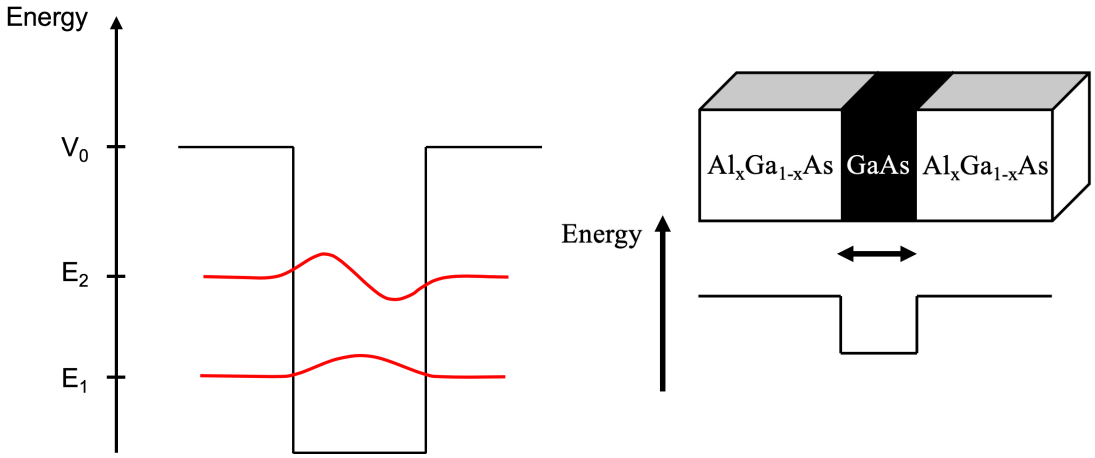

Figure 2.1: (Left) Confined states in a quantum well with a finite barriers of height V_0. The wave functions for $n = 1$ and $n = 2$ are sketched. (Right) A schematic structure of a GaAs / $Al_xGa_{1-x}As$ quantum well.

In practical cases, doping or alloying a host material is the primary method of interest for controlling the height of the confining potentials for a quantum well. Perhaps the best-known example of such a system is a quantum well consisting of gallium arsenide (GaAs) and aluminum gallium arsenide ($Al_xGa_{1-x}As$), as shown in Fig. 2.1 (right). The band gap of the material depends on the alloying level and varies between 1.42 eV ($x = 0$, GaAs) and 2.16 eV ($x = 1$, AlAs).

The idea to confine carriers at particular layers has also been adapted in transition metal oxides, although the high electron effective mass for strongly correlated oxides allows the system to behave differently. Note that for oxides, the Bohr radius of the wave function of carriers is about 1~5 unit cells, and truly two-dimensional conductivity is difficult to achieve. Fig. 2.2 shows a comparison of different varieties of two-dimensional systems and the mechanisms used to induce charge carriers.

A common feature for oxides is charge redistribution or reconstruction, which is the usual approach in semiconductors. A typical example is a heterostructure of ZnO / MgZnO [14], where interface reconstruction is related to a polarity step between ZnO and MgZnO. The doping mechanism at the quantum well produces no dopants in ZnO itself, and the effective mass of carriers in ZnO is relatively low compare to d electron transition metals, thus the mobility of carriers exceeds 10^6 cmV^{-1}s^{-1} [15, 16, 17]. ZnO can support either a two-dimensional electron gas or hole gas, depending on the interface termination.

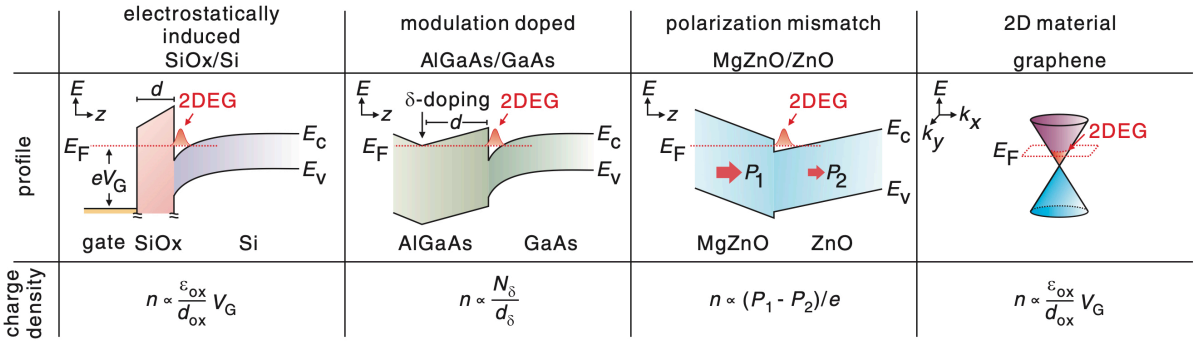

Figure 2.2: A comparison of different varieties of two-dimensional systems and the mechanisms used to induce charge carriers. Here, E_c is the conduction band, E_v is the valence band and E_F is the Fermi energy [18].

Several other oxide heterostructure quantum well systems have also been reported, such as $LaAlO_3$ / $SrTiO_3$ [19], $LaMnO_3$ / $SrMnO_3$ [20], $GaTiO_3$ / $SrTiO_3$ [21], and $LaAlO_3$ / EuO [22]. Among these, the most studied systems is certainly $LaAlO_3$ / $SrTiO_3$ heterostructure, showing several interesting functionalities: high-mobility two dimensional conductivity, apparent ferromagnetism, superconductivity, and strong Rashba-type spin-orbit coupling. At the same time, however, it is a rather complicated system with many unknown properties such as the dimensionality of quantum well, the complicated electronic structure (e.g., orbital character of carriers), the anisotropy of

electronic structure, or the role of defects, deviation of observed and predicted carrier densities, etc.

In this Chapter, starting from the perovskite structure, I explain the physical properties of $SrTiO_3$, and introduce some of the interesting phenomena that appear when $SrTiO_3$ is combined with a thin layer of $LaAlO_3$ or $LaTiO_3$.

2.2 Perovskite materials and heterostructures

Fig. 2.3 shows the unit cell of cubic perovskite oxide lattice represented by the general chemical formula ABO_3, where the A site (shown in blue) is occupied by rare earth or alkaline metal ion, and the B site (shown in green) is a transition metal atom. The lattice can thus be viewed along the [001] direction as consisting of a repeating sequence of AO and BO_2 layers, and the oxygen atoms form an octahedral cage around the B-site transition metal atoms. The physical properties of perovskites are mainly set by the selection of the B-site transition metal, which determines the number of electrons in the d orbitals, while the lattice parameter is determined by the A-site atoms. Due to this, various kinds of perovskite oxides with different physical properties can possess similar lattice constants (a) of about 0.4 nm, supporting the growth of high-quality heterointerfaces with few misfit dislocations.

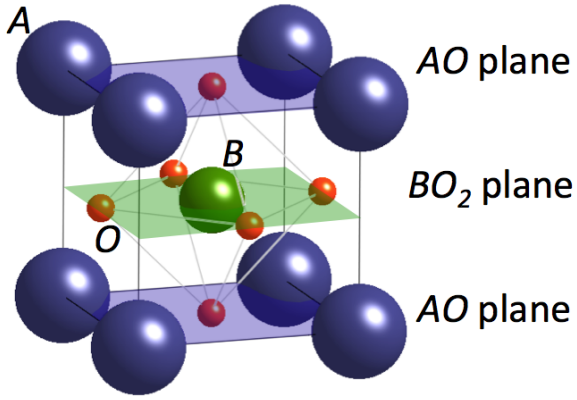

Figure 2.3: The ABO_3 perovskite structure consists of AO and BO_2 layers.

For an ideal perovskite structure in the cubic space group $Pm\bar{3}m$, the B-O distance is equal to a / $\sqrt{2}$, and the following equation between the ionic radii is established,

$$r_A + r_O = \sqrt{2}\,(r_B + r_O)\ , \tag{2.6}$$

where r_N is the ionic radius of atom N [23]. The perfect cubic structure, however, is found in very few cases, and orthorhombic or rhombohedral distortions are generally found along with less common distortions, i.e., tetragonal, monoclinic, and triclinic unit cells, usually containing more than one pseudo-cubic unit [24]. The measure of deviation from the ideal structure can be represented by the Goldschmidt 'tolerance factor' (t) [25], defined as

$$t = \frac{(r_A + r_O)}{\sqrt{2}(r_B + r_O)} \quad . \tag{2.7}$$

Eq. 2.6 tells that for an ideal cubic unit cell, t=1. When $t > 1$ (the A atom is too large to match the BO_2 layer), a hexagonal structure may be formed, and if $0.7 < t < 0.9$ (the A atom is much smaller than needed to fit the B atoms), an orthorhombic or rhombohedral structure is formed. In case of $t < 0.7$, ($r_A \sim r_B$) the perovskite structure may be lost.

With a wide range of available compositions, perovskite oxides offer many interesting possibilities for designing two-dimensional structures where new interface-related electronic phases may appear.

2.3 Physical properties of $SrTiO_3$

$SrTiO_3$ is well known as a substrate material with a prototypical perovskite structure. The main advantage of high-quality epitaxial oxide thin film growth is the availability of a reasonably stable and atomically flat crystal surface obtained by chemical etching and annealing [26]. In the [001] direction, the alternating half unit cell (uc) layers of the perovskite, i.e., SrO and TiO_2 layers, are both charge-neutral if perfect ionic bonding is assumed. The valence states of $(Sr^{2+}O^{2-})^0$ and $(Ti^{4+}O_2^{2-})^0$. The lattice of $SrTiO_3$ is cubic at room temperature with a lattice parameter of 3.905 Å, but an antiferrodistortive transition occurs at 105 K with a rotation of the oxygen octahedra, which makes the crystal slightly tetragonal (D_{4h}) at low temperature. At 4 K, the ratio of c/a ~1.001 [27, 28, 29]. Fig. 2.4 shows the change of the lattice constant of $SrTiO_3$ as a function of temperature, measured by X-ray diffraction.

$SrTiO_3$ is nominally a band insulator with an energy gap of 3.2 eV between the conduction band, which is essentially formed by Ti 3d orbitals, and the valence band, which is fully occupied by oxygen 2p orbitals with a small admixture of Ti d-orbitals [30, 31]. However, due to the ability of $SrTiO_3$ to change the Ti valence state from the nominal 4+ to 3+ and the presence of slight cation nonstoichiometry or impurities in

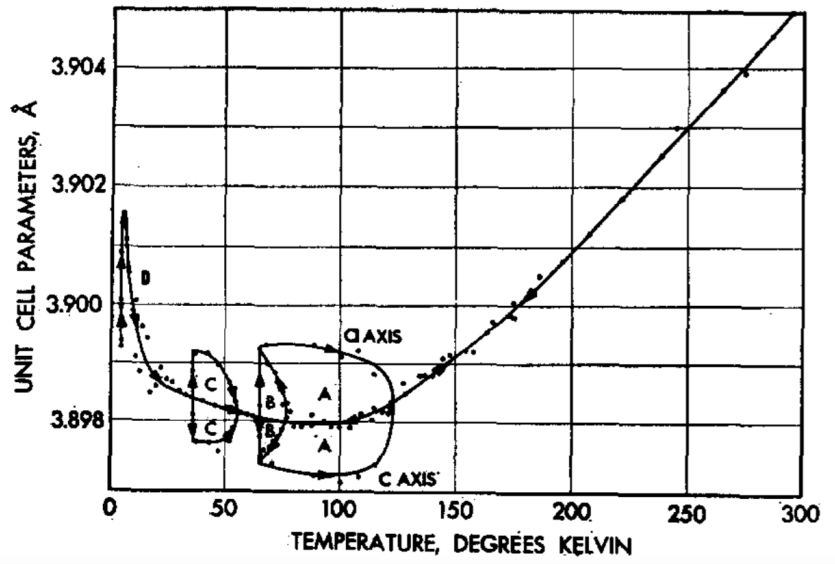

Figure 2.4: Spontaneous lattice distortions in $SrTiO_3$ as a function of temperature [27].

the lattice, the practical crystals always contain oxygen vacancies that lift the Fermi level close to the conduction band bottom.

Even slight doping by introducing either cation substitutions [32] or oxygen vacancies [33] induce a metallic state. Metallic conduction can be achieved at the critical carrier density of $\sim 10^{18}$ cm^{-3}, which is much lower than for most other transition metal oxides, giving a low-temperature Hall mobility in excess of 10,000 cm^2/Vs [34, 35]. Owing to the low critical carrier density of the insulator-metal transition, the carrier density of semiconducting $SrTiO_3$ can be easily modulated by field effect. Superconductivity also is observed in $n \sim 10^{18}$ to 10^{21} cm^{-3} range, as shown in Fig. 2.5 [36]. $SrTiO_3$ thus attracts a great deal of interest for testing various heterostructure and device geometries.

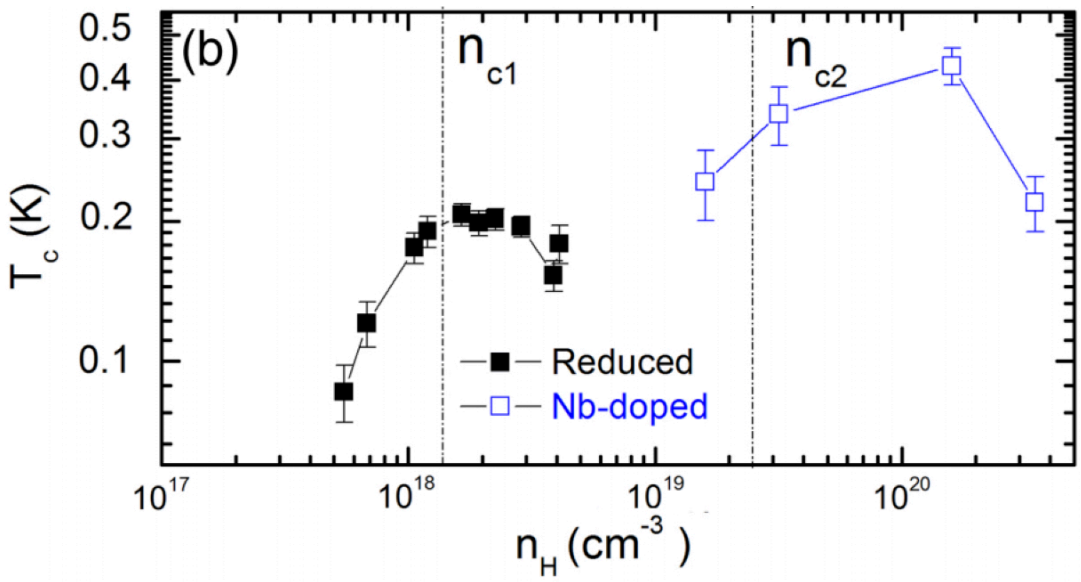

Figure 2.5: Transition temperatures versus charge-carrier concentration in $SrTiO_3$. The horizontal bars denote the temperature range of the transition [37].

$SrTiO_3$ is also famous for its unusual dielectric properties. The bulk dielectric permittivity of $SrTiO_3$ is $\epsilon_r \sim 300$ at room temperature for sintered ceramics [38], but rapidly increases upon cooling and eventually saturates at over 2×10^4 below 10 K. This "quantum paraelectric" state [39] (Fig. 2.6) is understood by considering that the effective temperature is limited by quantum fluctuations, suppressing the ferroelectric transition that would otherwise be expected to occur at around 35 K. Owing to this incipient ferroelectricity, the dielectric response of $SrTiO_3$ becomes sensitive to an external applied electric field [40] or lattice strain [41].

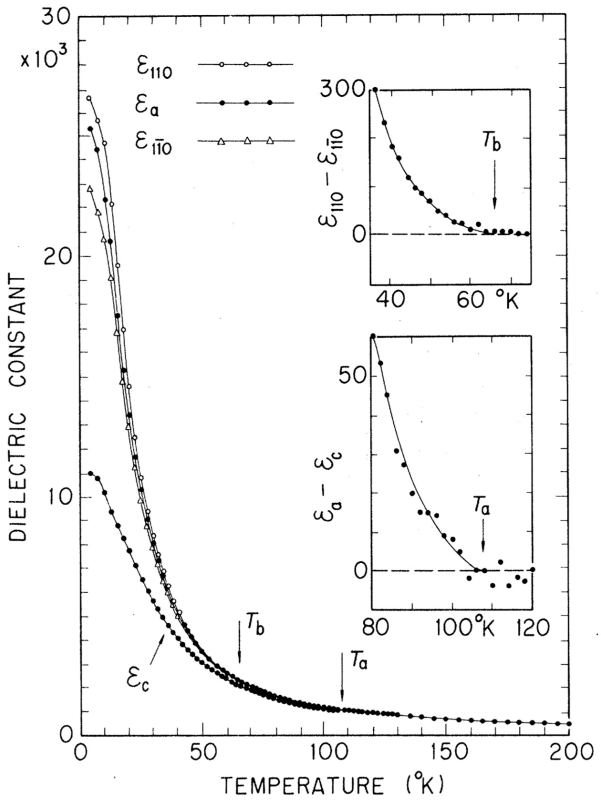

Figure 2.6: Temperature dependence of the dielectric constant of $SrTiO_3$ along different crystal axes [39].

2.4 Physical properties of $LaAlO_3$ and $LaAlO_3$ / $SrTiO_3$ interfaces

2.4.1 $LaAlO_3$

$LaAlO_3$ is a wide-gap band insulator with a band gap of 5.6 eV [42]. The crystal structure is a distorted perovskite ($R\bar{3}c$ space group) with a doubling of the rhombohedral c axis due to a rotation of the oxygen octahedra. For heterostructure description, the structure is often viewed as being a pseudo-cubic with a lattice constant of 3.79Å, and an interior angle of α=90.5°. The dielectric permittivity of bulk $LaAlO_3$ is $\epsilon_r \sim 24$ at room temperature and does not show a strong temperature dependence like $SrTiO_3$ [43]. With this relatively large permittivity, $LaAlO_3$ can be used as a gate insulator in various field-effect device structures [44, 45, 46, 47, 48].

2.4.2 $LaAlO_3$ / $SrTiO_3$ interfaces

In 2004, Ohtomo and Hwang discovered a two-dimensional electron gas at the interface of two band insulators, $SrTiO_3$ and $LaAlO_3$ [19]. This interface structure is experimentally simple to make and is famous for exhibiting high electron mobility exceeding 10,000 cm^2/Vs [19]. It has been demonstrated that two important features exist at this interface, i.e., the metallic conductivity only appears when **more than 4 unit cells of $LaAlO_3$** is grown onto a **TiO_2 terminated** $SrTiO_3$ (001) substrate.

Fig. 2.7 shows the insulator-metal transition by adding layers of $LaAlO_3$ on a $SrTiO_3$ substrate [49]. The carrier density of the system does not depend on the film thickness after the $LaAlO_3$ layer thickness exceeds 4 unit cells but depends on the fabrication process, which will be discussed in Chapter 4. The $SrTIO_3$ substrate termination affects the transport behavior dramatically. At an interface between two perovskite lattices, such as $LaAlO_3$ and $SrTiO_3$, two-layer configurations can exist. For a TiO_2-terminated substrate, the expected atomic layer sequence is AlO_2^- / LaO^+ / TiO_2^0 / SrO^0, which is known as the metallic n-type interface. When a SrO-terminated substrate is used, the layer sequence will be LaO^+ / AlO_2^- / SrO^0 / TiO_2^0, which produces an insulating p-type interface (Fig. 2.8).

The dimensionality of carriers accumulated at a $LaAlO_3$ / $SrTiO_3$ interface has been discussed in several studies. Because of oxygen vacancies that are unavoidably introduced during the film fabrication process, three-dimensional conductivity ($\sim 500\ \mu m$) has been observed in Shubnikov-de-Hass oscillations when heterostructures are grown

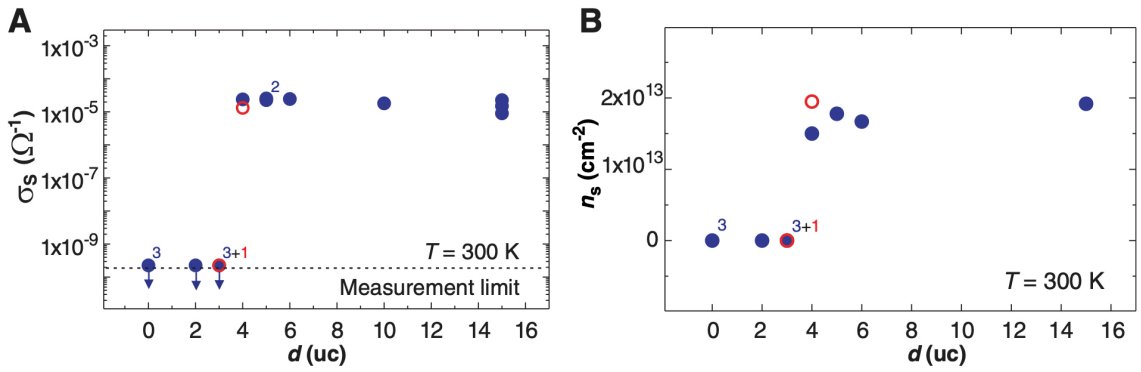

Figure 2.7: Influence of $LaAlO_3$ thickness on the electronic properties of the $LaAlO_3$-$SrTiO_3$ interfaces. (A) Sheet conductance and (B) carrier density of the heterostructures plotted as a function of the number of their $LaAlO_3$ unit cells [49].

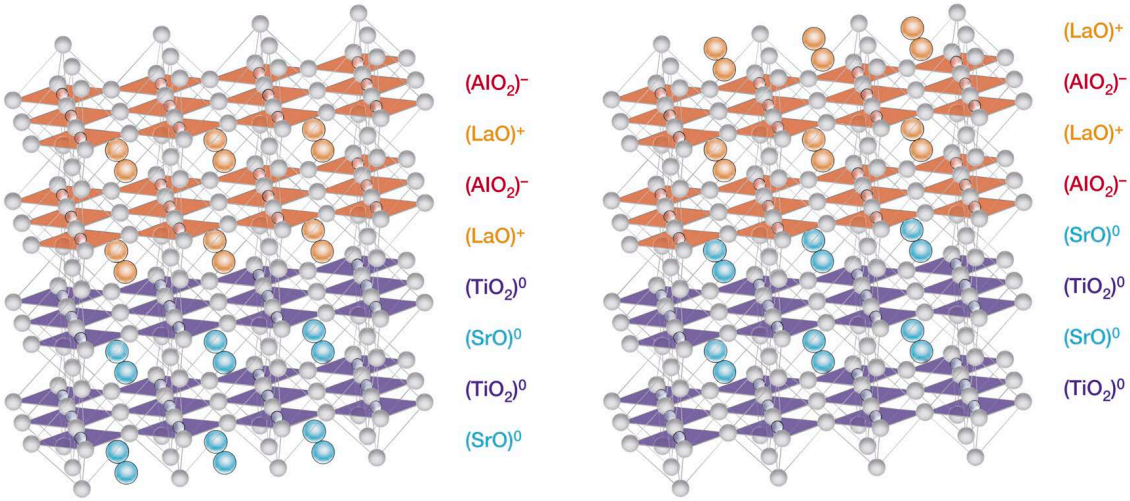

Figure 2.8: (Left) Schematic of the conducting $(LaO)^+$ / $(TiO_2)^0$ interface. (Right) Schematic of the insulating $(AlO_2)^-$ / $(SrO)^0$ interface [19].

at low oxygen pressures, at $P_{O_2} < 10^{-5}$ mbar without oxygen post-annealing process [50]. In contrast, two-dimensional superconductivity has been reported, and the conducting layer thickness has been estimated to be $\sim$ 10 nm at low temperature for samples deposited at 6×10^{-5} mbar and annealed in 400 mbar of oxygen [51]. The oxygen annealing helps to refill isolated oxygen vacancies and thus suppresses oxygen vacancy related bulk conductivity in the $SrTiO_3$ substrate.

The thickness of the conducting layer has been visualized directly by looking at a cross-section sample with a conductive-tip atomic force microscope (CT-AFM) (Fig. 2.9). The spatial resolution of the measurement is limited by the radius of the AFM tip but shows that the conducting layer is no broader than $\sim$ 7 nm when oxygen vacancies are filled by post-annealing in oxygen, while the thickness grows to a few micrometers in samples that have not been oxygen-annealed after film growth [52]. The conducting layer thickness is also a function of temperature since the thickness of an accumulation layer is proportional to the square root of the dielectric permittivity, which diverges at low temperatures in $SrTiO_3$.

The appearance of superconductivity [51, 54] and ferromagnetism [55, 56] make this interface famous in the oxide community. While the superconductivity has been observed systematically in many previous reports, the existence of the ferromagnetism at this interface is still under debate. Fig. 2.10 shows the reported experimental results on observing apparent ferromagnetism at a $LaAlO_3/SrTiO_3$ interface. There is no common reported model of magnetism at this interface, e.g., domain size of the PEEM-MCD measurement is about a few hundred nanometers (Fig. 2.10 (d), which does not match the SQUID measurements that observe apparent 10μm features (Fig. 2.10 (c)).

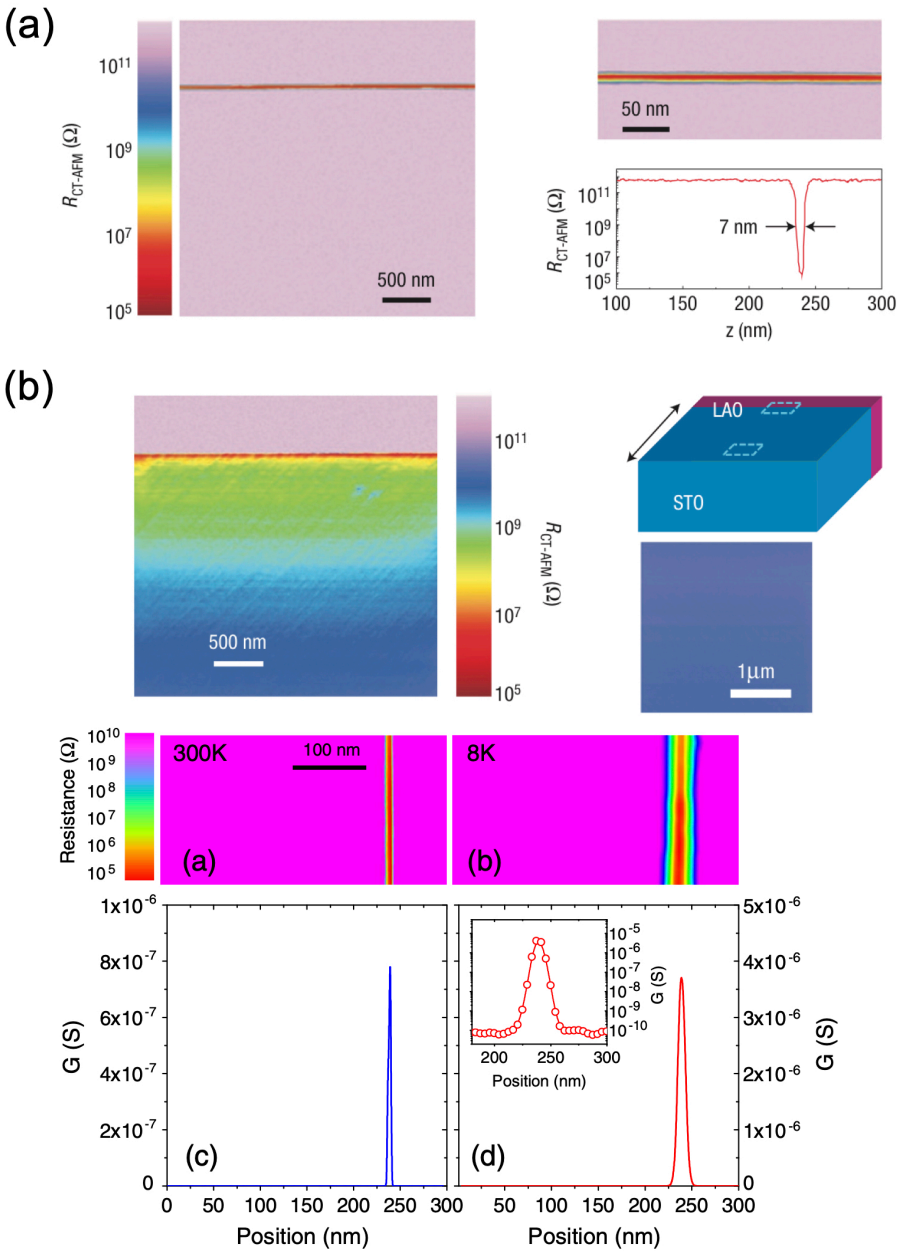

Figure 2.9: Conductive-tip AFM images in cross section geometry. (Upper) (a) Non-annealed $LaAlO_3$ / $SrTiO_3$ interface. (b) In-situ oxygen annealed $LaAlO_3$ / $SrTiO_3$interface. Right panel shows an image in high-resolution mode and profile [52]. (Lower) Collected image at (a) 300K and (b) 8K, and corresponding conductance profiles (c), (d). The inset in (d) shows the same data in logarithmic scale [53].

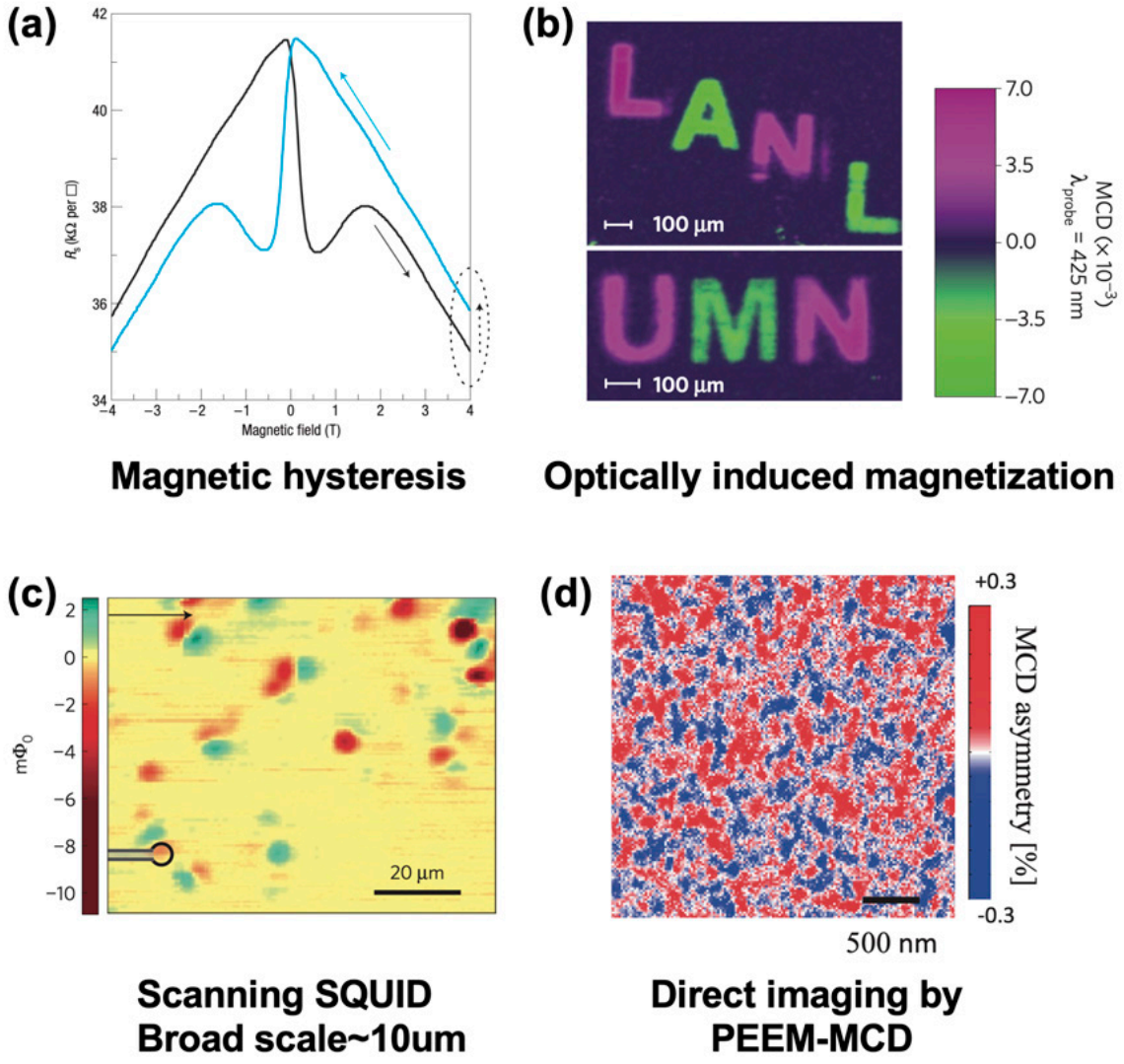

Figure 2.10: (a) Sheet resistance at 0.3 K of an *n*-type $SrTiO_3$ / $LaAlO_3$ conducting interface. The arrows indicate the direction of the measurements (at a rate of 30 mT/s) [57]. (b) A demonstration that magnetic information can be optically written into $SrTiO_{3-\delta}$, stored, and then optically read out [58]. (c) $LaAlO_3$ / $SrTiO_3$ magnetometry image mapping of ferromagnetic order [55]. (d) MCD image of $LaAlO_3$ (6 uc) / $SrTiO_3$. An apparent domain structure was observed. The averaged domain size is about 100 nm [59].

Many theoretical works predict that there would be a large number of electronic subbands, which affects the physical properties of the interface discussed above. Fig. 2.11 shows the shift in the energy levels of Ti 3*d* in different crystal fields of $SrTiO_3$. Without any crystal field, a spherical Ti atom has five-fold degenerate *d*-levels of d_{xy}, d_{yz}, d_{zx}, $d_{x^2-y^2}$, and d_{z^2}. When the Ti atom is surrounded by the oxygen octahedron, the 3*d* orbitals are split into a high-energy doublet (e_g) and a low-energy triplet (t_{2g}). The tetragonal phase transition at 105 K results in a further *d*-level splitting. When a two-dimensional electron gas is formed at the surface or at a heterointerface, the breaking of inversion symmetry produces additional splitting between the e_g and the t_{2g} states on the order of ~ 100 meV and ~ 50 meV, respectively, by assuming an interface composed of at least 90% of Ti^{4+} ions [60, 61].

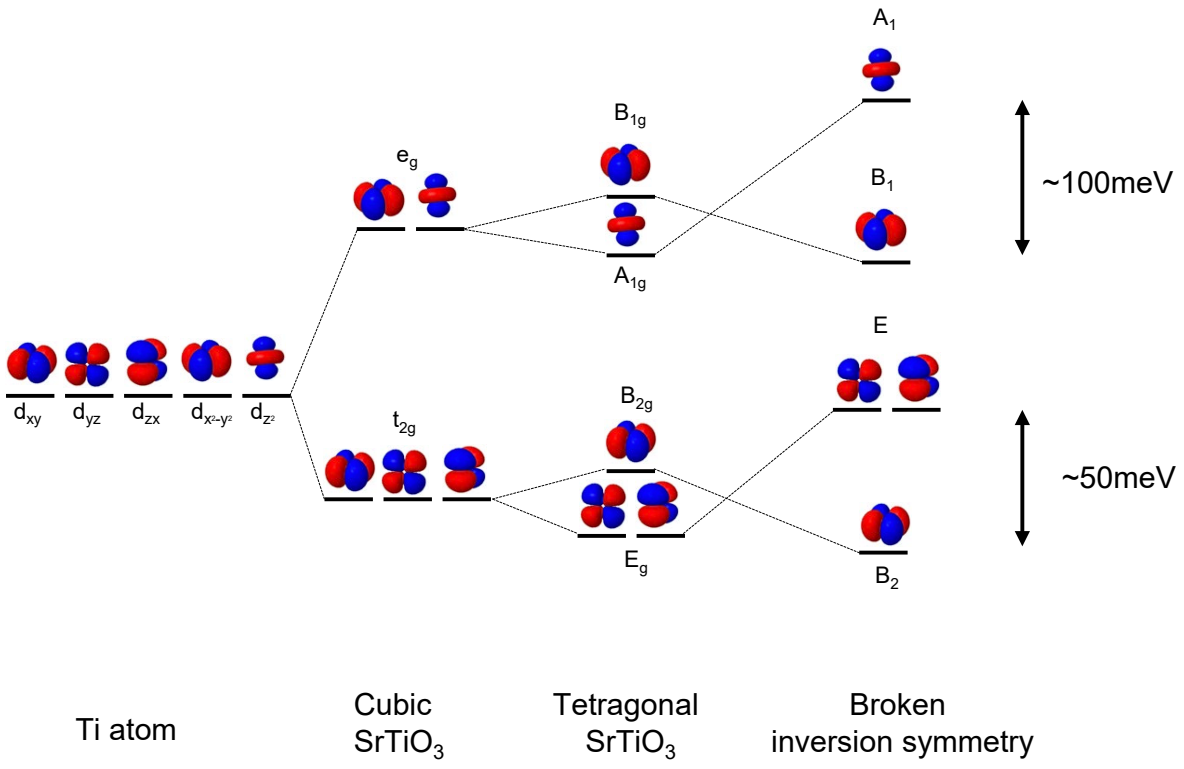

Figure 2.11: Energy of the Ti 3*d* orbitals in the presence of different crystal fields.

Recently, a special point in transport of $LaAlO_3$ / $SrTiO_3$ system is observed where transitions in which the number of bands crossing the Fermi level increases, i.e., Lifshitz point [62]. By filling up the electronic structure near the Lifshitz point, the spin-orbit interaction from the broken inversion symmetry at the interface is expected to

drastically change, as shown in Fig. 2.12.

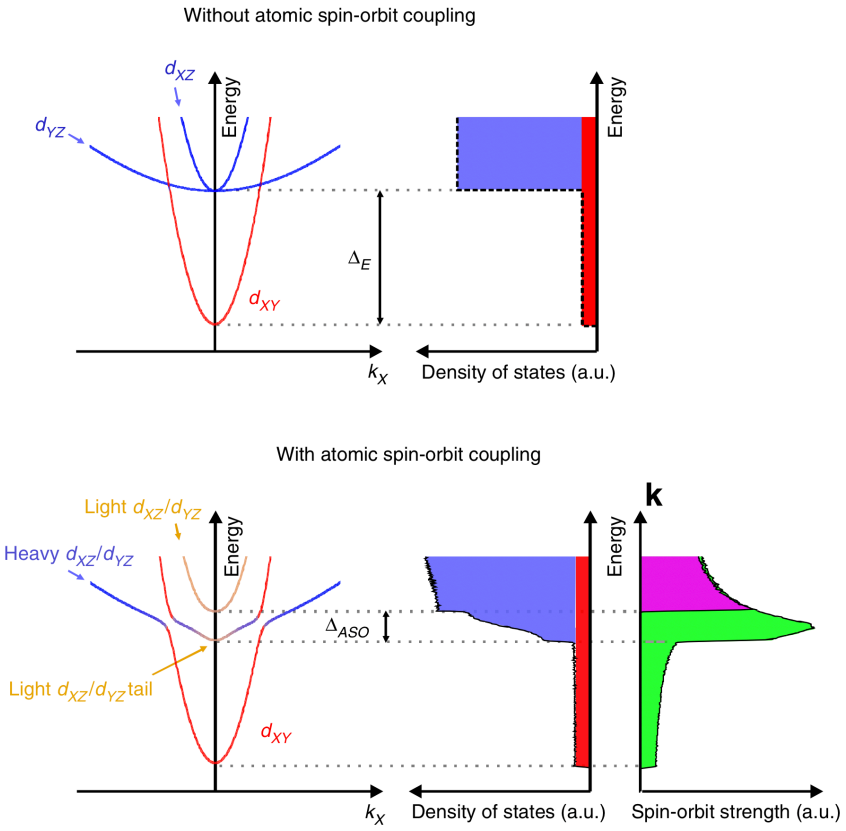

Figure 2.12: (Upper) *d*-orbital energy bands of $SrTiO_3$ near its interface with $LaAlO_3$ without atomic spin-orbit coupling. Schematic density of state diagram versus energy is illustrated in the right-hand panel. (Lower) Calculated band structure, density of states, and spin-orbit coupling strength when atomic spin-orbit interactions exist [63].

2.5 Mechanisms for the conduction at the $LaAlO_3/SrTiO_3$ interface

To identify the origin of the electron gas and the quantum confinement has proven to be a very complicated issue, because multiple problems are linked together such as the polar nature of the $LaAlO_3$ layer, the possibility of various electronic and structural relaxation mechanisms, and the dielectric and electronic properties of the $SrTiO_3$ substrate itself [19, 64, 65, 66, 67, 68].

The two following scenarios have been proposed for the origin of the conducting layer at the interface: (1) A doping mechanism related to the intrinsic polar discontinuity (polar catastrophe) and electronic reconstruction; (2) a doping mechanism due to extrinsic off-stoichiometry such as the introduction of oxygen vacancies in $SrTiO_3$ or due to cation intermixing.

2.5.1 The intrinsic electronic reconstruction scenario

This scenario is related to the polar discontinuity at the interface, giving an elegant explanation for the observed conductivity difference between the *n*-type (SrO^0 / TiO_2^0 / LaO^+ / AlO_2^-) and the *p*-type (TiO_2^0 / SrO^0 / AlO_2^- / LaO^+) interfaces.

Figure 2.13 describes the charge accumulation mechanisms due to the polarity discontinuity. When a polar lattice is combined with a non-polar material in an epitaxial interface, an internal electrostatic potential along the out-of-plane direction appears in the polar lattice, and the potential grows in proportion to the polar layer thickness [64]. To avoid this potential build-up(Fig. 2.13 (a), (b)), also known as a polar catastrophe, the charge can be transferred from the top of the polar layer to the interface when the number of polar layers exceeds a critical thickness t_c [69]. For a polar $LaAlO_3$ on $SrTiO_3$,

$$t_c = \frac{\epsilon_0 \epsilon_{LaAlO_3} \Delta E}{e P^0_{LaAlO_3}}, \tag{2.8}$$

where ϵ is the dielectric permittivity, $\Delta E \sim 3.3$ eV is the difference of energy between the valence band of $LaAlO_3$ and the conduction band of $SrTiO_3$, e is the electron charge, and $P^0_{LaAlO_3}$ is a formal polarization of $LaAlO_3$.

For reasonable permittivity and polarization values, this equation gives an estimated critical thickness of $t_c \sim 3.5$ unit cells, which matches the experimental result of 4 unit cells. When the $LaAlO_3$ thickness reaches t_c, the internal potential increase in the

$LaAlO_3$ becomes large enough to bring the valence bands of $LaAlO_3$ to the same level with the $SrTiO_3$ Ti $3d$ conduction band and a Zener breakdown occurs, transferring charge to the interface. Above t_c, electrons will be transferred progressively from the surface to the interface until the internal electric field divergence is eliminated. The accumulated carriers in the Ti $3d$ conduction band lead to metallic conductivity at the interface [69].

By adding more $LaAlO_3$ layers, the charge transfer from $LaAlO_3$ to $SrTiO_3$ converges to half a carrier per two-dimensional unit cell, at which point the accumulated charge no longer increases [64, 70]. As a result, half an electron is transferred for the n-type interface grown on a TiO_2-terminated $SrTiO_3$ surface. Conversely, half a hole would ideally be transferred for the p-type interface. The Ti valence state can change from 4+ to 3.5+ as shown in Fig. 2.13(c), however, there is no possible mixed-valence state that would allow a half a hole to be injected into the $SrTiO_3$ substrate. The crystal is assumed to respond by injecting oxygen vacancies into the terminating SrO layer of the $SrTiO_3$ substrate.

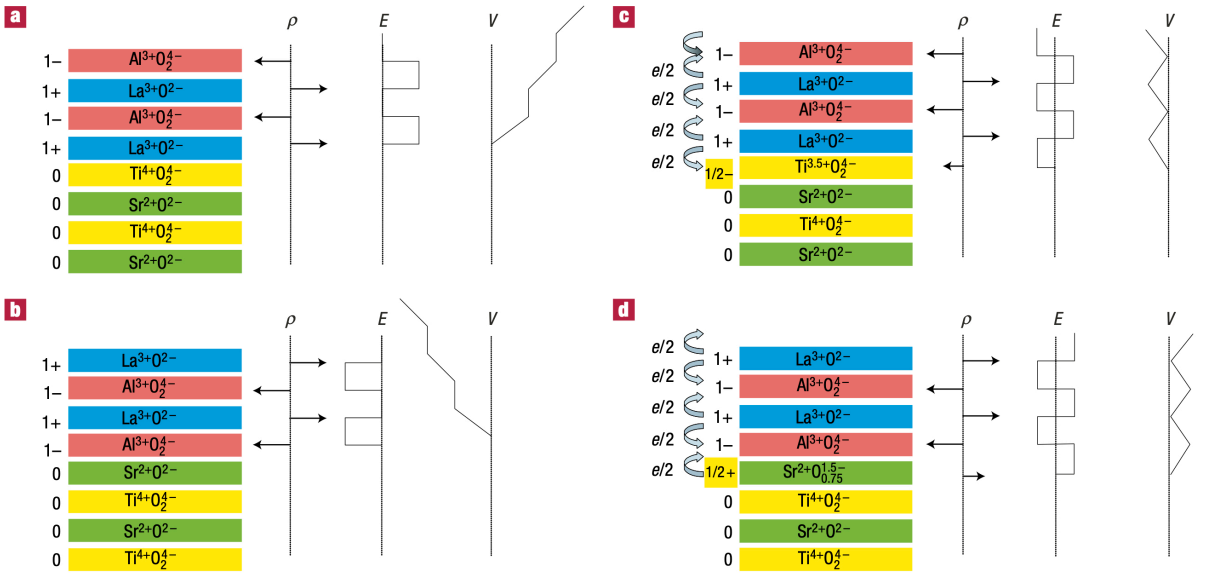

Figure 2.13: The polar catastrophe model illustrated for atomically abrupt (001) interfaces between $LaAlO_3$ and $SrTiO_3$ [64].

The electronic reconstruction scenario shows good agreement with many experimental results, i.e., the observation of the critical thickness phenomenon [49, 71], the ability to control the interface conductivity by manipulating the surface with a scanning

probe microscope [72], or by covering the surface with polar adsorbates [73].

This model assumes the presence of an ideal interface without any defects, which is unlikely to be true for an oxide heterostructure grown by pulsed laser deposition. Extrinsic effects, such as cation defects, may explain why the experimental carrier density is up to one order of magnitude lower [74, 75, 76] than the expected value of $0.5e^-$ per planar unit cell , or $\sim 3.3 \times 10^{14}$ cm^{-2}.

2.5.2 The extrinsic defects-related scenario

Although the intrinsic polar discontinuity mechanism appears to give a good match with many experimental results, there are still inconsistencies.
1. Lower carrier density than expected.
2. Core-level shift of $LaAlO_3$ by X-ray photoemission spectroscopy is smaller than the energy shift predicted by the polar catastrophe model [65, 77, 78, 79]
3. Amorphous $LaAlO_3/SrTiO_3$ is also conducting [80], as are heterostructures grown on $SrTiO_3$(110) surfaces [81, 82].

Due to these somewhat controversial issues, another scenario of extrinsic defects-related mechanism has been suggested. Additionally, it is experimentally difficult to construct a perfect crystalline interface, especially for a polar/non-polar heterostructure. Cation intermixing on the length scale of a few unit cells has been observed in high-resolution transmission electron microscope (TEM) images [66, 83, 84].

Cation intermixing

Reconstruction of atomic structure at the $LaAlO_3/SrTiO_3$ interface may occur by the formation of antisite cation defects (La $\leftrightarrow$ Sr, Al $\leftrightarrow$ Ti), which can also resolve the polar catastrophe problem. Metallicity in the system is robust because bulk $SrTiO_3$ becomes conducting even at very low dopant densities, and thus even a very small number of defects could, in principle, lead to a metallic interface. Artificially intermixed interfaces have been studied to test this mechanism [69], however, the intermixed films do not show the expected increase of conductivity with the $LaAlO_3$ layer thickness.

Oxygen vacancies

Oxygen vacancies are the most common dopants in $SrTiO_3$. Oxygen vacancies can donate carriers to the Ti 3*d* band and may also form local electronic defects, depending on whether the vacancy carries a charge of -2 or -1. Oxygen vacancies can thus lead to

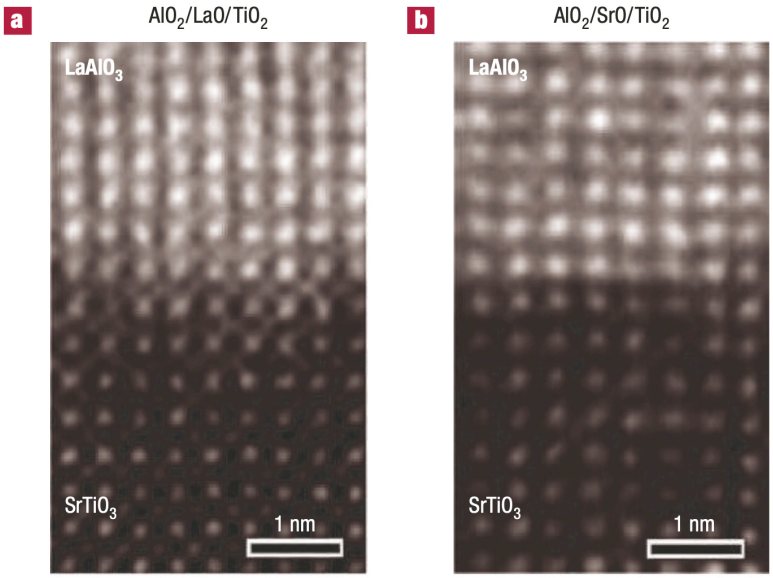

Figure 2.14: High-angle annular dark field-scanning TEM image of (a) *n*-type interface, (b) *p*-type interface [64].

changes in electronic, magnetic, and optical properties of $SrTiO_3$ [85, 86]. Thus, oxygen vacancies have been considered as a possible source of the conductivity in $LaAlO_3$ / $SrTiO_3$ interfaces [87, 88].

2.6 Physical properties of $LaTiO_3$ and $LaTiO_3$ / $SrTiO_3$ interfaces

2.6.1 $LaTiO_3$

Similar to $SrTiO_3$, $LaTiO_3$ is another perovskite-type oxide in the (*Pbnm*) space group (Fig. 2.15), and a textbook example of Mott-Hubbard insulator with antiferromagnetic order [89]. The nominal valence state of Ti^{3+} allows one electron in the $3d$ t_{2g} shell, which means that the layers making up the crystal are polar $(La^{3+}O^{2-})^+$ and $(Ti^{3+}O_2^{2-})^-$. However, the Mottness is strongly sensitive to the chemical composition [90], such as slight cation doping or oxygen vacancies. The phase diagram of bulk $LaTiO_3$ shows that slight doping by introducing extra oxygen causes the Mott gap to close (Fig. 2.16) and results in metallic conductivity. Various phases, such as semiconducting, metallic,

and ferroelectric insulator states, can appear at room temperature [91].

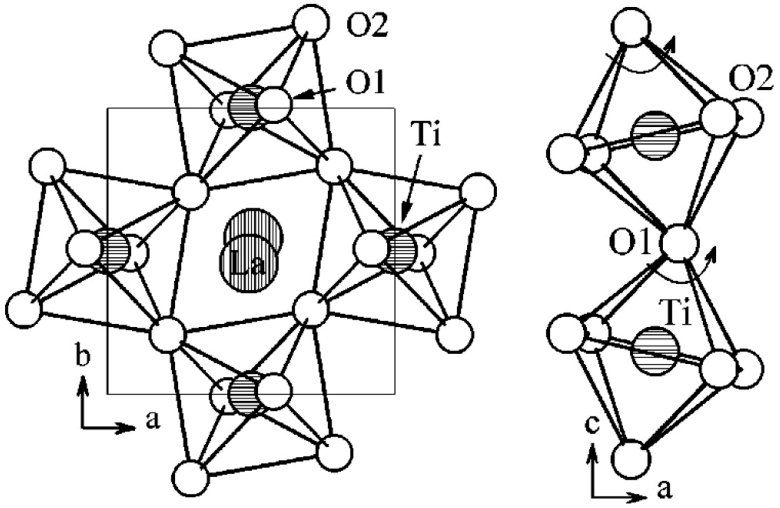

Figure 2.15: Crystal structure of $LaTiO_3$ in space group *Pbnm*, O2 and O1 denote the oxygen in the a, b planes and the apical point, respectively. The left part shows four octahedra connected in the a, b plane, the right part a pair of neighboring octahedra along the c axis direction [92].

Due to the relatively larger ionic radius of La, the lattice constant is 3.97 Å. The $LaTiO_x$ lattice can accept additional oxygen in the range of $3 \leq x \leq 3.5$, gradually forming the $La_2Ti_2O_7$ phase by the inclusion of shear planes. Meanwhile, weak ferromagnetism has been observed below 140 K for the oxygen content between $x = 3.0$ and 3.1 [93]. The lattice parameters also change with the oxygen content in bulk $LaTiO_x$ [94]. When the oxygen content (x) reaches 3.5, the nominal Ti valence reaches 4+, and the electronic properties change from a Mott insulator (Ti^{3+}) to a band insulator (Ti^{4+}). The phase diagram is shown in Fig. 2.16. The $La_2Ti_2O_7$ phase has a monoclinic structure, and it is a stable ferroelectric oxide [91].

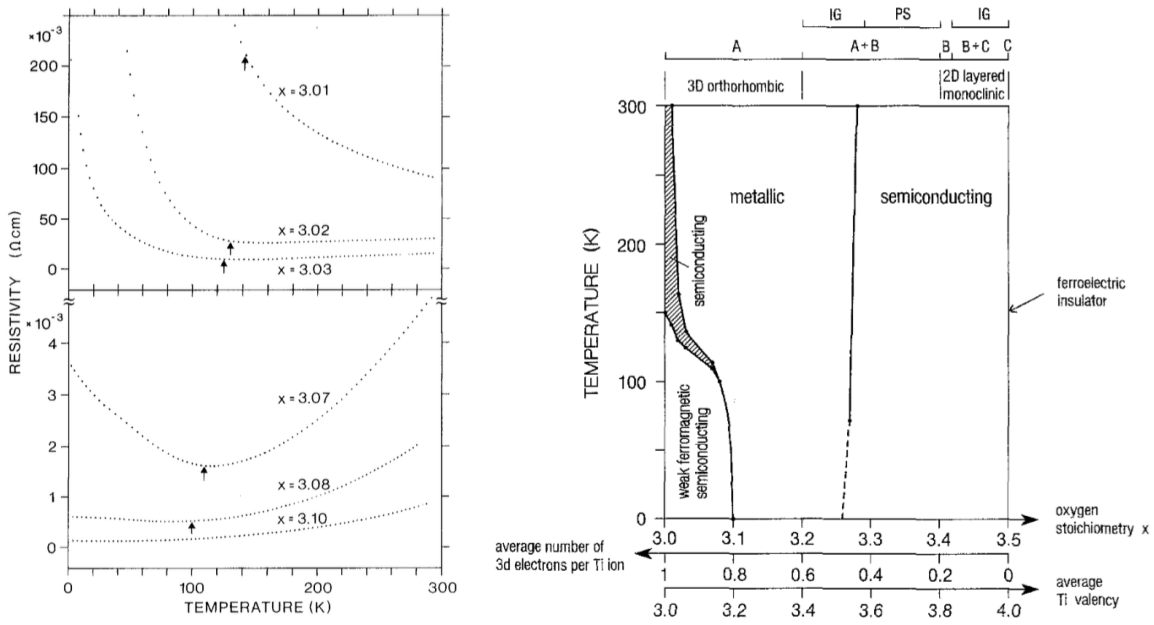

Figure 2.16: (Left) Temperature dependent conductivity of $LaTiO_x$. Slight doping by introducing extra oxygen x causes the Mott insulator state of stoichiometric $LaTiO_3$ to be broken. Phase diagram of $LaTiO_x$. (Right) Heavy doping with oxygen creates a band insulator Ti^{4+} phase. The metallic and semiconducting labels refer to $d\rho \,/\, dT > 0$ and $d\rho \,/\, dT < 0$, respectively, where ρ is the resistivity [91].

2.6.2 $LaTiO_3$ / $SrTiO_3$ interfaces

As explained above, the Mott insulator $LaTiO_3$ has an odd number of electrons per unit cell, and the Coulomb repulsion that localizes the *d* electrons is the key to the formation of a band gap. However, when such a material would be combined with a band insulator, the symmetry can be broken, leading to a metallic state.

In this thesis work, the focus is on the interface between $LaTiO_3$ and $SrTiO_3$, i.e., one or more charged $(LaO)^+$ layers replace some of the SrO layers in an otherwise continuous Ti-O network of the $SrTiO_3$ lattice, as shown in Fig. 2.17.

The lattice constants of the two materials are relatively well matched, with a = 3.91 Å for $SrTiO_3$ and a = 3.97 Å for $LaTiO_3$ (Table 2.1). Since carriers are accumulated in $SrTiO_3$, similarly high carrier mobility that has been observed at $LaAlO_3$ / $SrTiO_3$ interfaces can also be achieved in this system. At the same time, however, the origin of metallicity at this interface is different from the polar catastrophe of $LaAlO_3$ / $SrTiO_3$, since the *B*-site lattice consists entirely of titanium ions without polar divergence issues.

Materials	Lattice constant(Å)	In-plane strain	Out-of-plane strain
$SrTiO_3$	3.905		
$LaTiO_3$	3.97	-1.6%	+3.4%
$LaAlO_3$	3.79	+3.0%	-5.8%

Table 2.1: Lattice constants of $SrTiO_3$, $LaTiO_3$, and $LaAlO_3$. Compared to the $SrTiO_3$ substrate, $LaTiO_3$ and $LaAlO_3$ films may be strained.

Theoretical studies have shown that various ordered phases may exist in the $LaTiO_3$ / $SrTiO_3$ heterostructures by applying different electron filling and interaction strength. Orbitally ordered or disordered phases, with either para-, ferro- or antiferromagnetic character have been predicted to exist for some model parameter values [10]. The rich phase diagram is due to the effect of the large ferroelectric-like distortions of the TiO_6 octahedra, which substantially affect the Ti *d*-electron density [9]. In addition to magnetic phases, charge ordering has been suggested by Pentcheva *et al.* to occur at the interfaces of ideal $LaTiO_3$ / $SrTiO_3$ superlattices to avoid highly charged d^0 ions from being nearest neighbors [95], as shown in Fig. 2.19. Density functional theory (DFT) predicted that a sharp potential well around a single $LaTiO_3$ layer extends to a distance of up to 2 nm [96, 97, 98]. A metallic state was found at the interface whose extent strongly depends on the dielectric constant of the material [99]. The importance of lattice relaxations has also been reported [9, 100].

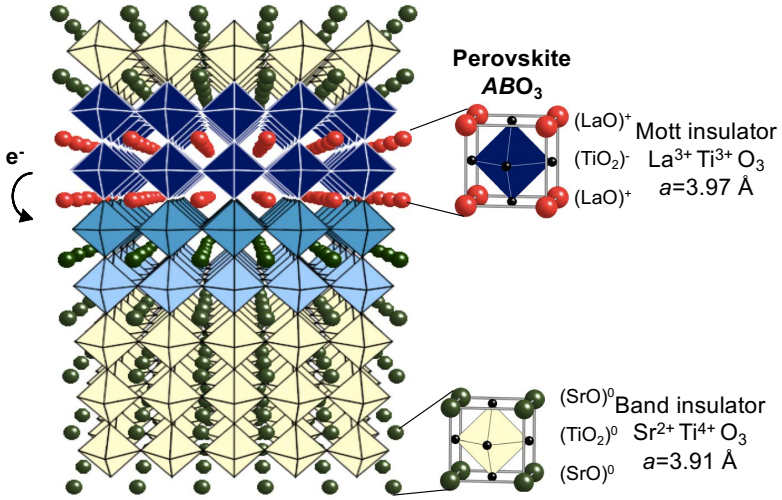

Figure 2.17: $LaTiO_3$ / $SrTiO_3$ interface

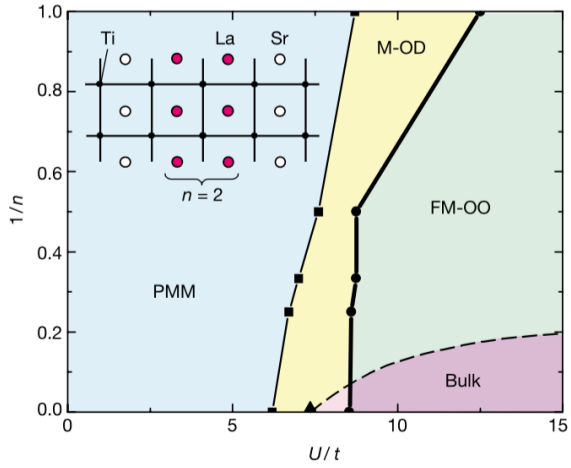

Figure 2.18: Ground-state phase diagram computed in Hartree-Fock approximation as a function of the on-site Coulomb interaction U and the inverse of the La layer number n. (PMM : paramagnetic metal with no orbital ordering, M-OD : orbitally disordered magnetic state, FM-OO : fully polarized ferromagnetic state with (00π) orbital order, Bulk : ferromagnetic spin order and G-type $(\pi\pi\pi)$ antiferro-orbital order bulk state [10].

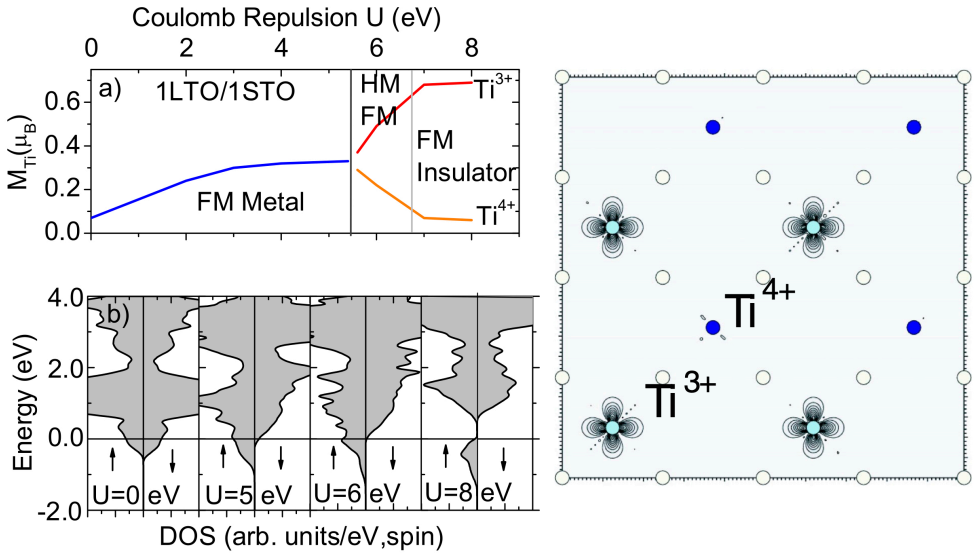

Figure 2.19: (Left) For the ($LaTiO_3$, $SrTiO_3$) = (1, 1) superlattices, (a) phase diagram of the Ti moments in a transverse c2×2 cell vs the on-site Coulomb repulsion strength U on the Ti $3d$ orbitals. HM: half metallic, FM: ferromagnetic. (b) 45° checkerboard charge density distribution of the occupied $3d$ states in the charge-ordered TiO_2 layer in the FM (1, 1) multilayer. Orbital ordering due to d_{xy} orbital occupation is apparent. The positions of O, Ti^{3+}, and Ti^{4+} ions are marked by white, light blue, and dark blue circles, respectively [95].

These reports have shown that electronic phases with very different physical properties can exist in oxides confined to thin layers compare to what is observed in bulk form, even when the same materials are used.

Scanning transmission electron microscopy-electron energy-loss spectroscopy(STEM-EELS) mappings of $LaTiO_3$ / $SrTiO_3$ heterostructures have shown that when one or two layers of $LaTiO_3$ are embedded in $SrTiO_3$, additional carriers appear in the Ti $3d$ conduction band in the vicinity of the (La,Sr)TiO_3 layer (Fig. 2.20) [101]. The spread of the extra electrons can be seen in the fractional Ti^{3+} signal($\sim$ 0.4), which is considerably wider than that of the physical La doping layer. The width of the doped layer is determined by carrier accumulation in $SrTiO_3$. This has important implications for transport in such doped heterostructures.

These superlattices were found to be conducting, with a variation by the superlattice periodicity (n, m) in $[(LaTiO_3)_n/(SrTiO_3)_m]$ (Fig. 2.21). The measured Hall carrier density is $\sim$ 0.48 e^-/uc and mobility is $\sim$ 3 cm^2/Vs at 300 K [101, 102]. These values are similar

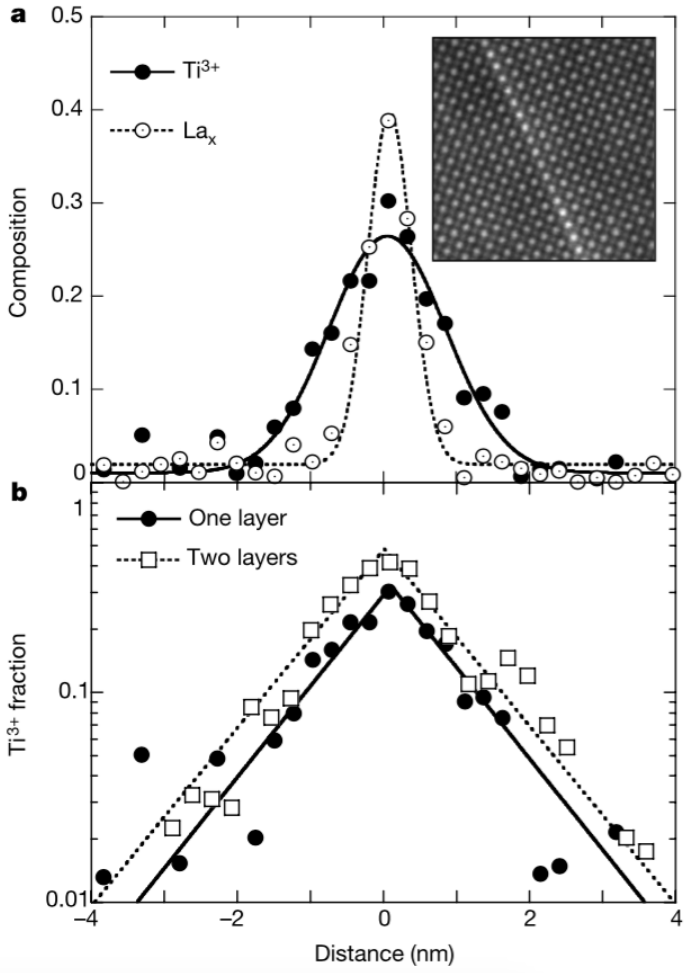

Figure 2.20: redSpatial distribution of the cation composition signal in the vicinity of the $LaTiO_3$ single layer and bilayer [101].

to bulk $La_xSr_{1-x}TiO_3$ crystals [103]. Takizawa *et al.* measured ultraviolet photoemission spectra (UPS) and observed a Fermi edge, indicating that metallic states exist [104]. Infrared spectroscopic ellipsometry was used to obtain a sheet carrier density per interface of about 2×10^{14} cm^{-2} ($\sim$ 0.34 e^-/uc), with a mobility of $\sim$ 3 cm^2/Vs at 300 K [105].

At low temperatures, a strong non-linear Hall resistance has been reported at this superlattice interfaces [106], which is similar to the $LaAlO_3$ / $SrTiO_3$ interfaces [76]. This can be attributed to the presence of a carrier density depth profile and the variation of carrier mobility with distance from the interface (Fig. 2.22).

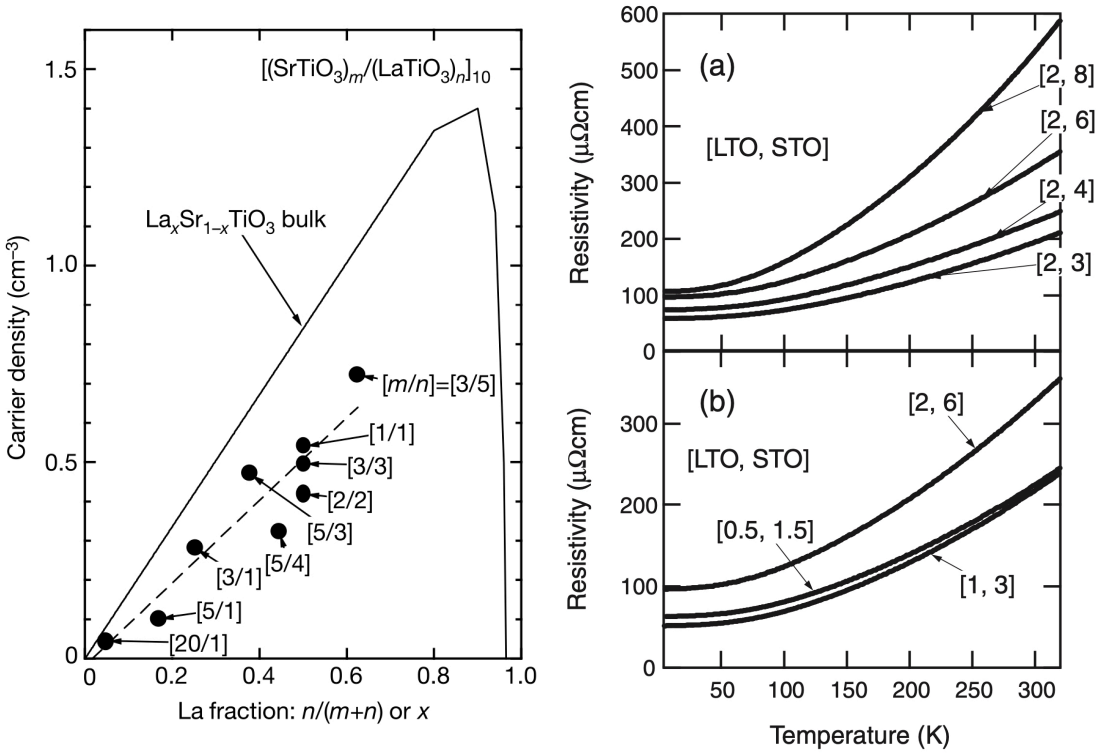

Figure 2.21: (Left) The carrier density from Hall effect measurements for various superlattices of $[(SrTiO_3)_m / (LaTiO_3)_n]_{10}$, compared with bulk $La_xSr_{1-x}TiO_3$ [101]. (Right) Resistivity of superlattice films as a function of temperature. (a) The thickness of the $LaTiO_3$ layers was fixed at 2 unit cells. (b) Superlattice period was changed while maintaining the average composition of $La_{0.25}Sr_{0.75}TiO_3$.

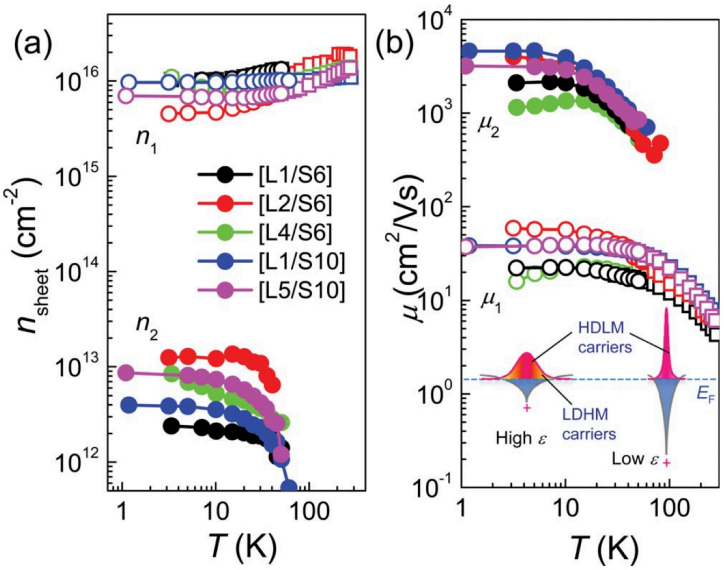

Figure 2.22: The temperature dependence of (a) sheet carrier densities (n_1, n_2) and (b) mobilities (μ_1, μ_2), assuming a two-channel conduction in various $LaTiO_3$ / $SrTiO_3$ superlattices [106].

2.6.3 Delta-doped heterostructures design

In conventional semiconductors, confining carriers in a narrow region has been very successful by putting a thin layer of high dopant concentration, i.e., delta-doping [107, 108]. It has been shown in oxides that even a fractional-layer doping layer embedded in a host matrix materials can give rise to fascinating new physical properties [109].

For $SrTiO_3$ based heterostructures, Mihara *et al.* have grown thin $LaTiO_3$ films on $SrTiO_3$ substrates and measured the resistivity of the interfaces from room temperature to 4 K [110]. Interestingly, after *ex situ* oxygen annealing, which was used to eliminate oxygen vacancies, a 60Å $LaTiO_3$ film was completely insulating. However, when a thin, insulating $LaTiO_3$ film was covered (capped) with $SrTiO_3$, the film became metallic (Fig. 2.23 (left)). The measured metallicity was increased by adding more $LaTiO_3$ layers between the $SrTiO_3$ layers, as shown in Fig. 2.23 (right). They also showed that the metallic conductivity of $LaTiO_3$ films did not appear when the films were grown on $NdGaO_3$ substrates. This indicates that this conductivity originated from the $SrTiO_3$ substrate, not the $LaTiO_3$ film itself.

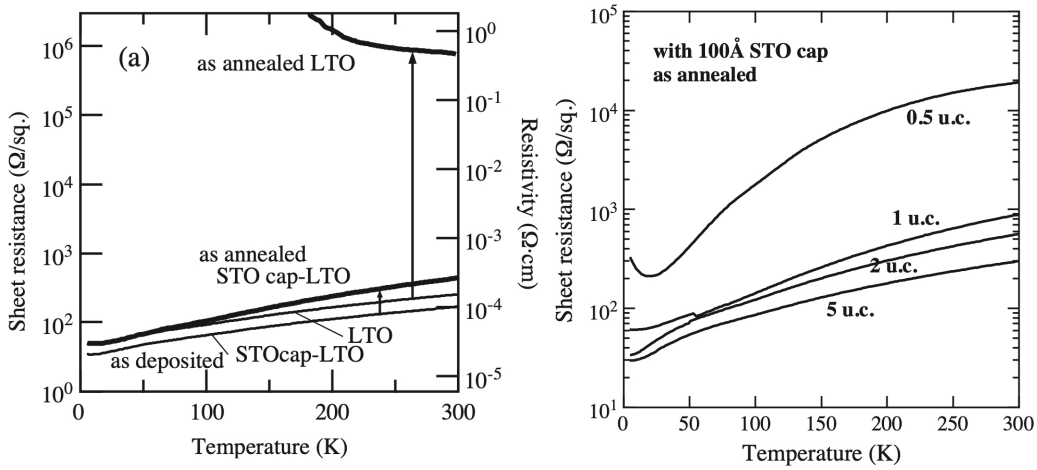

Figure 2.23: (Left) Sheet resistance of a 60 Å $LaTiO_3$ film on $SrTiO_3$. An uncapped film became insulating after annealing in air, while a capped film remained metallic. (Right) Sheet resistance of capped $LaTiO_3$ layers as a function of temperature [110].

Only very thin $LaTiO_3$ layers are used in the heterostructures studied in this work. In this case, the formation of the non-perovskite phases is suppressed by epitaxial strain, and the perovskite structure with an atomically flat surface can be maintained up to a thickness of about 5 unit cells. Since the $LaTiO_3$ layer is in most heterostructures

only a single unit cell layer thick, a Mott insulator state cannot form since the effective valence of the Ti atoms in this layer is higher than 3+ due to charge transfer and the d band occupation is thus between d^0 and d^1. Such ultrathin $LaTiO_3$ layers should thus be viewed as LaO delta-doping layers in a wide-gap semiconductor $SrTiO_3$, rather than an interface between a band insulator and a Mott insulator.

Capping layer effect

The heterostructures were capped with a $SrTiO_3$ layer that was grown immediately on top of the $LaTiO_3$ film. In order to eliminate the oxygen vacancies created during film growth, the heterostructures were post-annealed in air. However, it is possible that the post annealing may cause oxidation of the $LaTiO_3$ film, forming the $La_2Ti_2O_7$ phase [110].

Another reason for the capping is the existence of an insulating dead layer. The strong surface depletion that has been observed to occur on the surface of metallic La-doped thin films [111] (Fig. 2.24). The thickness of the surface depletion layer d_0 is

$$d_0 = \sqrt{\frac{2\epsilon(T)\epsilon_0 V_B}{en}}, \tag{2.9}$$

where ϵ and ϵ_0 are the $SrTiO_3$ and vacuum dielectric constants, respectively, and V_B is the surface pinning potential. To eliminate the surface depletion effect, an approximately 10 nm (25 u.c.) thick $SrTiO_3$ capping layer is required.

The presence of a depletion barrier in oxides is also reported in other heterostructures. When a La^{3+} was inserted at a controlled distance from a non-doped $CaHfO_3$ or $CaHfO_3/SrTiO_3$ interface, the insulator-metal transition occurred as a function of the layer thickness, as shown in Fig. 2.25.

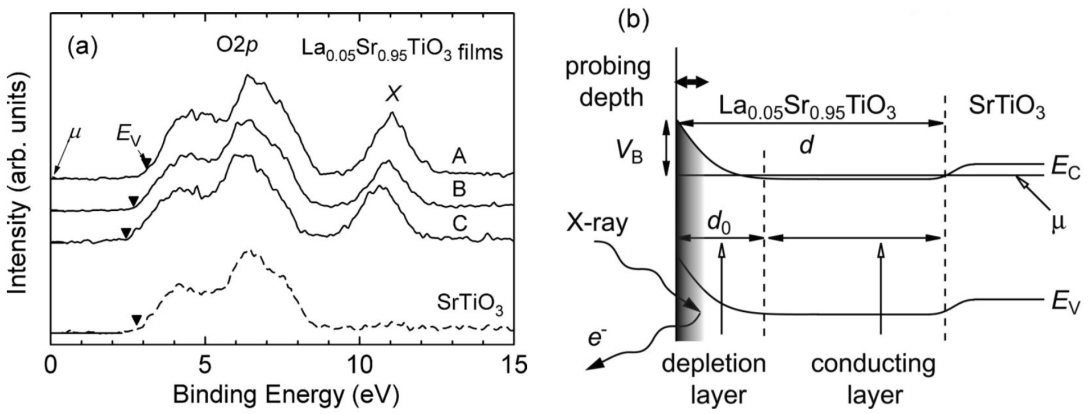

Figure 2.24: (a) XPS spectra near the valence-band maximum for a 1500 Å $La_{0.05}Sr_{0.95}TiO_3$ film. Samples A, B, and C were grown in 10^{-6} Torr, 10^{-5} Torr and 10^{-4} Torr of O_2, respectively. (b) Schematic band diagram of a $La_{0.05}Sr_{0.95}TiO_3$ film. The depletion layer is thicker than the XPS probing depth of ~ 20 Å[111].

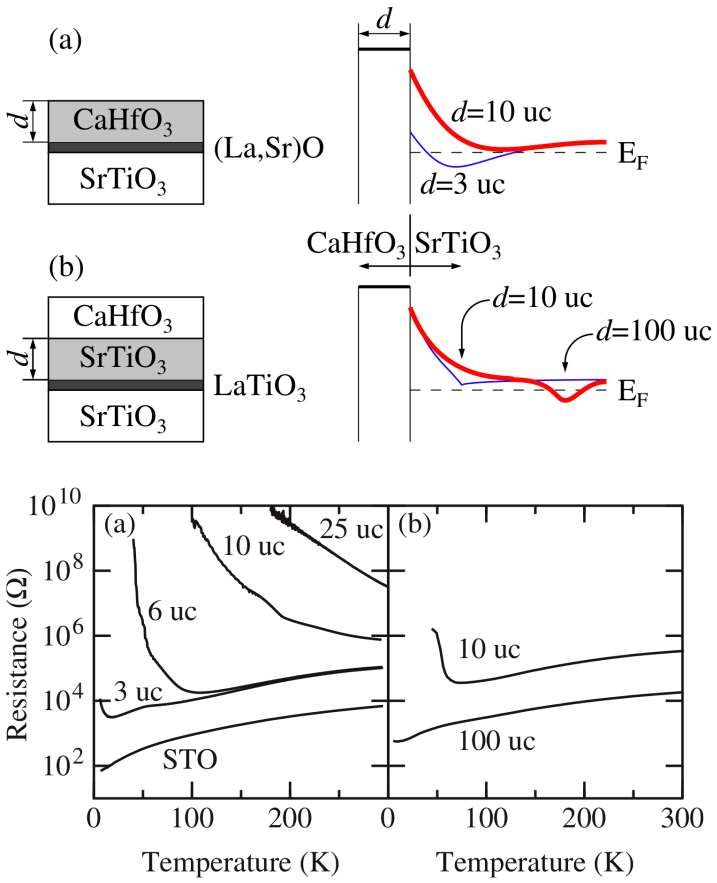

Figure 2.25: Structure of delta-doped heterostructures. (a) The $CaHfO_3$ cap layer thickness d was varied to change the level of carrier depletion in the doping layer, as illustrated in the conduction band edge diagram for d = 3 uc and d = 10 uc cases in the right panel. (b) The $SrTiO_3$ spacer layer thickness was varied, placing a $LaTiO_3$ delta-doping layer at a depth of 10 or 100 uc from the interface. Lower panels show the resistance measurements of the same heterostructures as above. [112]

The properties of the accumulated carriers in $SrTiO_3$ in the vicinity of the $LaTiO_3$ layers have been studied in detail by Ohtsuka *et al.* [113]. Through magnetotransport measurements (Fig. 2.26), they concluded that there are two types of carriers in the $LaTiO_3/SrTiO_3$ heterostructures; low-mobility carriers close to the $LaTiO_3$ layer and high-mobility carriers distributed deep in the $SrTiO_3$ substrate. The non-linearity was enhanced at low temperatures, and could be affected by the $LaTiO_3$ layer thickness, the $SrTiO_3$ thickness, or the film fabrication process.

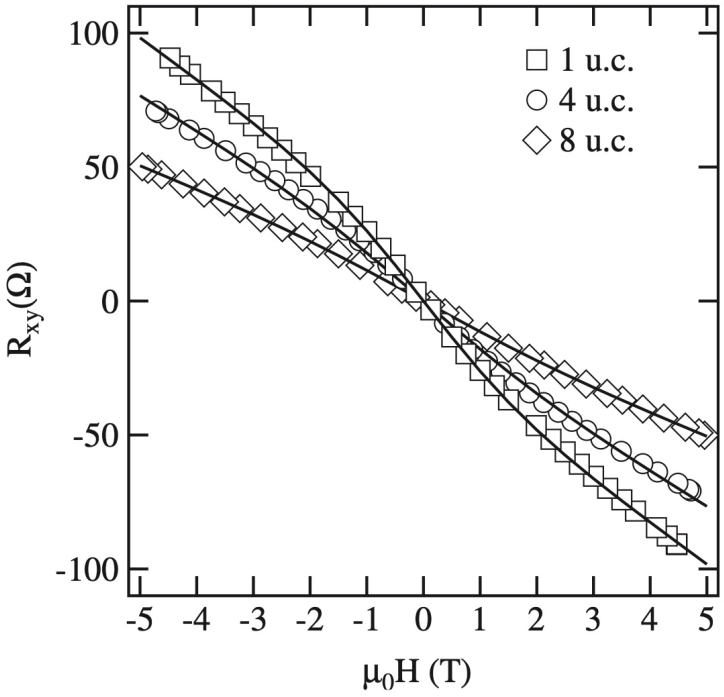

Figure 2.26: Hall resistance and two-layer fitting results for 1, 4, and 8 unit cell $LaTiO_3$ layers embedded in $SrTiO_3$, measured at 5 K [113].

As shown in Fig. 2.27, the quantum wells are formed in the vicinity of the $LaTiO_3$ layer, and the thickness of the $LaTiO_3$ doping layer and the $SrTiO_3$ capping layer determine the number of carriers in the quantum well, the quantum well width, and the asymmetry of the confining potential. The heterostructures were deliberately deposited at a very low temperature of 500°C to minimize La/Sr interdiffusion and to obtain a defect-rich $SrTiO_3$ capping layer with low dielectric permittivity that does not diverge at low temperatures. This leads to an asymmetric spread of carriers around the $LaTiO_3$ layer as illustrated in Figs. 2.27(a) and (b), and any carriers that are doped into the low-crystallinity $SrTiO_3$ cap layer have sufficiently low mobility to be neglected in transport

analysis.

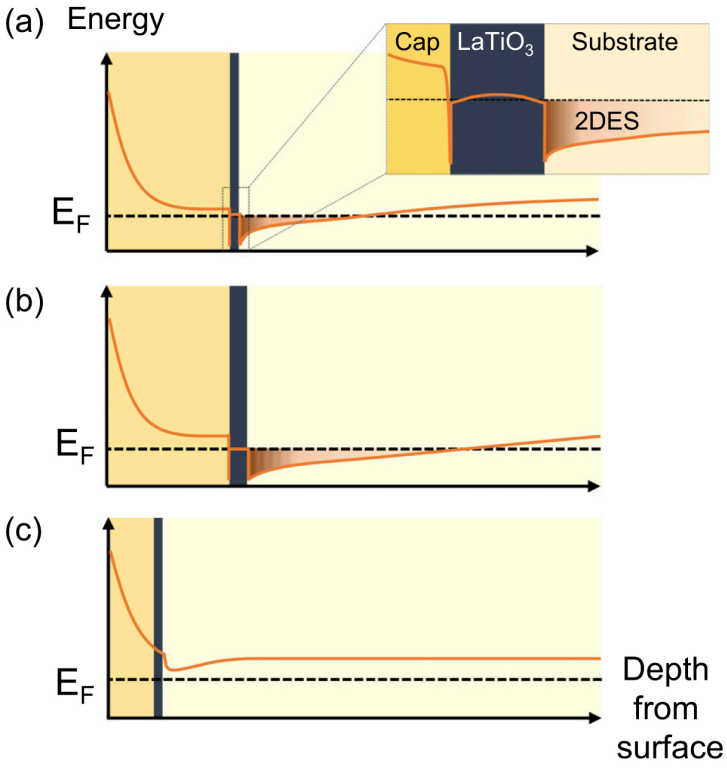

Figure 2.27: Expected conduction-band edge potential diagram in $SrTiO_3/LaTiO_3/SrTiO_3$ structures

Chapter 3

Sample growth and characterization

3.1 Introduction

Growing high-quality oxide films requires accurate control over film composition, oxygen pressure, and the growth temperature, among other parameters. Since the discovery of high-T_c superconductivity in 1987, techniques to grow oxide thin films have seen rapid development [114, 115]. Pulsed laser deposition (PLD) is one such technique, and it is suitable for fabricating atomically smooth oxide films with accurately-controlled complex cation stoichiometry. A combination of a very broad range of available growth temperatures and oxygen pressures makes this technique particularly useful for oxide film growth. Over the past several decades, PLD systems have been developed that provide a base pressure on the order of 10^{-9} Torr and can thus be used to grow films in contaminant-free gas environments, even at very low oxygen pressures, i.e., in highly reducing conditions. The maximum useful ambient gas pressure is about 1 Torr of O_2 or even ozone, providing strongly oxidizing growth conditions. Epitaxial and highly crystalline materials can be grown at up to about 1400°C. More interestingly, due to the high kinetic energy of the atoms delivered to the film surface in a PLD plasma plume, crystalline films of some oxides can be grown even at room temperature. Besides offering a wide process parameter space, PLD is also a very versatile technique because many different materials can be grown in a single PLD chamber simply by switching between multiple pelletized ceramic sources.

In this Chapter, I describe the process of oxide thin film growth using the PLD technique, and the measurement techniques used for characterizing the thin film samples. Combined with *in situ* reflection high-energy electron diffraction (RHEED) monitoring, accurate control of the film thickness becomes possible, and the PLD system can be

used to construct heterostructures with high reproducibility. Besides counting RHEED intensity oscillations, the film thickness was cross-checked with the help of a stylus-profilometer and atomic force microscopy (AFM). Transport and magnetotransport measurements were performed in conventional dark conditions, under light illumination, or in the presence of an applied electric field.

3.2 Sample fabrication

3.2.1 Pulsed laser deposition instrumentation

Pulsed laser deposition is a versatile method for growing small-area high-quality oxide films. A high-energy pulsed laser beam is used to ablate a ceramic target of the desired material, forming a plasma plume that carries the ablated atoms to the growing film. Due to the high instantaneous temperature at the focus point on the target surface, the evaporation is nearly stoichiometric, which means that for many materials, the target composition can be the same as the desired film. The great advantage of this stoichiometric material transfer is that the target material can be synthesized by conventional bulk ceramic techniques, and no special stoichiometry control is necessary during the film growth process. The PLD growth process is thus much simpler than, e.g., molecular beam epitaxy(MBE), where each source flux needs to be accurately controlled for complex oxide growth.

A schematic illustration of the PLD system is shown in Fig. 3.1, showing the path of the pulsed laser beam, the position of the ablation target pellet, the substrate, the beam path of the RHEED system, the position of the RHEED imaging phosphor screen, the entry direction of the substrate heating laser, the pyrometer used for sample temperature measurement, and an oxygen pressure adjustment valve.

A pulsed KrF excimer laser (ThinFilmStar, Tui Laser, λ = 248 nm), which corresponds to a photon energy of 5 eV, was used to ablate the target materials. The photon energy is sufficiently high to be strongly absorbed by most oxides, facilitating efficient energy transfer from light to target and stoichiometric evaporation. A synthetic quartz viewport is used for laser beam entry, and the focusing is done with a single plano-convex lens. The excimer pulse length is relatively long ($\sim$ 20 ns) and is typically focused on a spot that gives an energy density of $\sim$ 1 J/cm^2 on the target surface. The laser pulse is long enough for the evaporation to proceed through thermal energy transfer to the target and to the plume, rather than multiphoton absorption as would

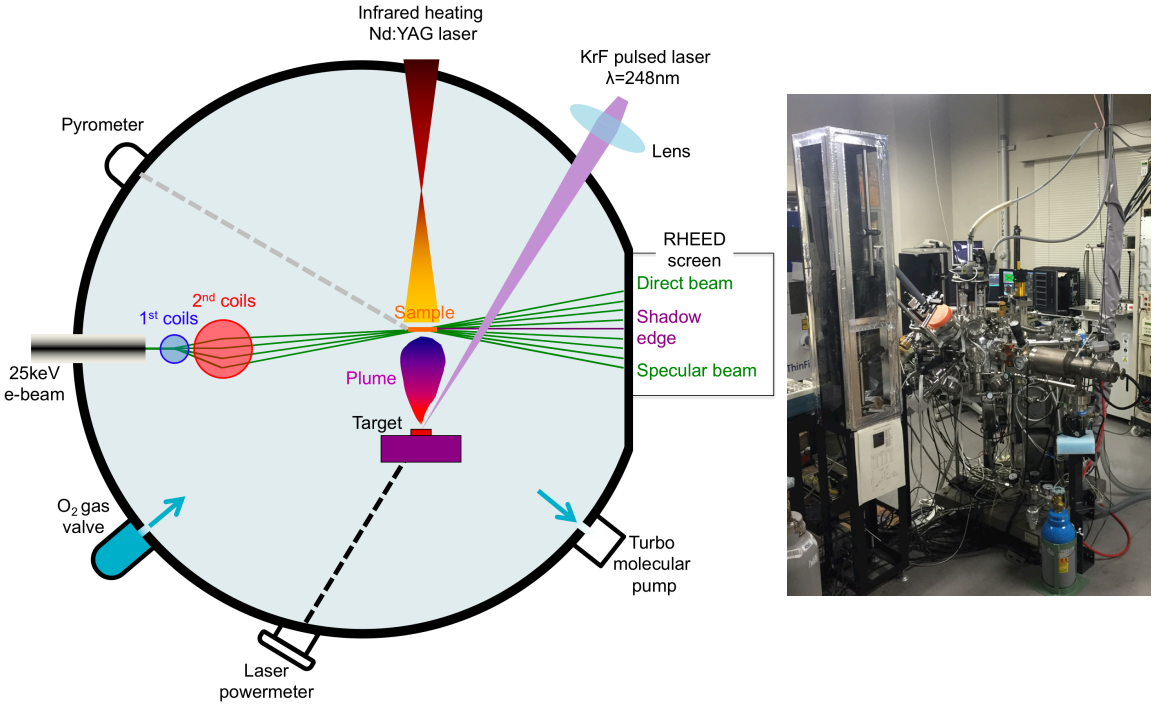

Figure 3.1: (Left) Schematic diagram of the major components of the PLD chamber. (Right) A photograph of the deposition system.

happen for a picosecond laser. In general, this longer pulse length helps to avoid the formation of solid particles or liquid droplets being ejected from the target, although the repeated melting and cooling of the target surface may lead to target surface composition changes. Fortunately for the film growth experiments described in this work, such minor stoichiometry deviations are not critical, and no further parameter tuning was necessary for stoichiometry adjustments (Fig. 3.2). The film growth experiments were done at a fixed laser fluence of close to 0.6 J/cm^2. The fluence was determined by measuring the laser pulse energy just before each deposition with a pyroelectric energy monitor, which was located at an exit viewport. The target was moved out of the laser path for energy monitoring, and the laser beam was allowed to pass through the chamber for energy measurement. This technique is critical to correctly compensate for the gradual coating of the laser entry viewport by the ablated film material. When the energy loss becomes too large, the viewport can be removed and cleaned.

The ablation fluence is the primary process parameter for controlling the deposition rate. The fluence was adjusted so that 20 to 100 ablation shots were required to grow a single perovskite unit cell layer. This mode of operation gives highly accurate control

over the layer thicknesses.

The ablation produces a transient, highly-luminous directional plasma plume [116] that expands outward from the target material surface and expands rapidly in the low-pressure ambient gas. Evaporated ions can reach kinetic energy of up to about 100 eV in the ablation plume. This kinetic energy has to be considered when selecting film growth process conditions. On the one hand, the high kinetic energy may lead to film surface re-sputtering and structural defects in the film. On the other hand, the high kinetic energy allows epitaxial films to be grown at lower substrate temperatures because the surface mobility of a high-energy adatom is sufficiently high. Avoiding higher growth temperatures effectively eliminates bulk cation diffusion, which is beneficial for fabricating very thin films or delta-doping layers. If necessary, the kinetic energy of the ablated atoms can be reduced by gas-phase collisions when higher ambient gas pressure is used [117]. In this work, energy moderation was not used and the growth of heterostructures at the lowest possible temperature was used instead to minimize bulk diffusion effects.

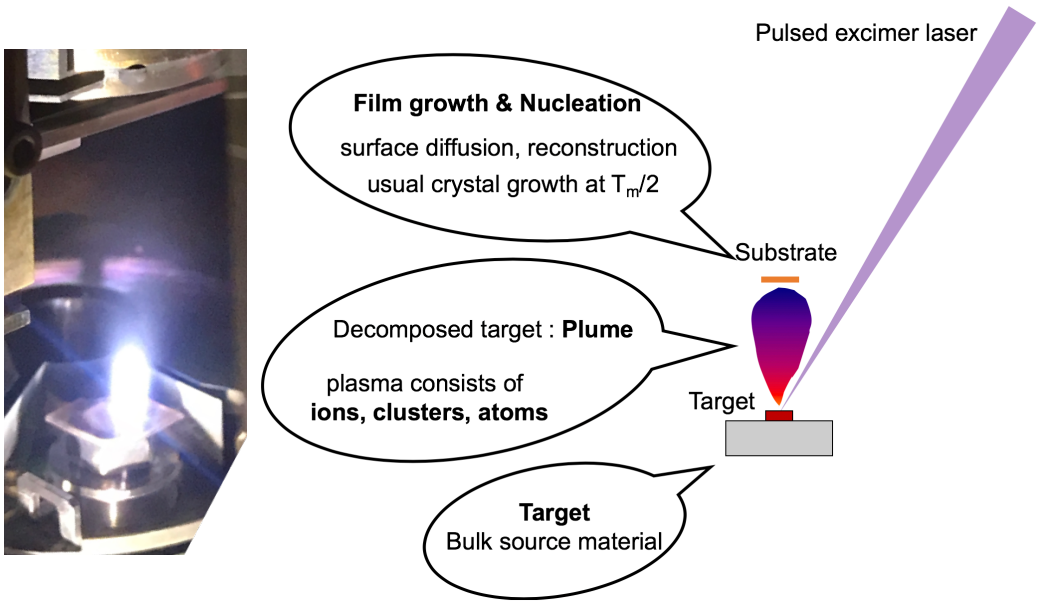

Figure 3.2: (Left) A photograph of the plasma plume inside a PLD chamber during thin film growth. (Right) Schematic diagram of the PLD technique.

The crystallinity of an oxide thin film generally depends on (1) the growth temperature and (2) the oxygen partial pressure inside the chamber, which affects the surface atom diffusion rate. In the PLD system described here, the substrate was heated with

a 140 W near-infrared fiber-coupled diode laser[118], introduced into the chamber through a simple pyrex viewport. The heating spot size and position were adjusted with a three-lens collimating optic attached to the top flange of the chamber. Figure 3.3 shows the position and size of the heating laser on a sapphire diffuser mounted at the sample position for optical alignment. For film growth, a SiC block was used as a laser light absorber and heat spreader. The substrate crystals were attached to the SiC block with platinum paste to improve the thermal conductivity between the substrate and the SiC susceptor. Laser spot adjustments were made to obtain homogeneous heating of the SiC susceptor within the substrate area. As shown in Fig. 3.4, half-ball ruby spacers were used as heat insulators between the heat-absorbing SiC susceptor block and the stainless steel body of the sample holder. The SiC susceptor block temperature was monitored with an optical pyrometer, which monitors infrared emission in the range of 2 to 2.5 μm. A LabVIEW program (Fig. 3.5) maintains the set substrate temperature by adjusting the heating laser power under PID control, allowing to heat the sample up to about 1200 °C in an oxygen ambient and provides rapid heating or cooling rates of over 100 degrees per second.

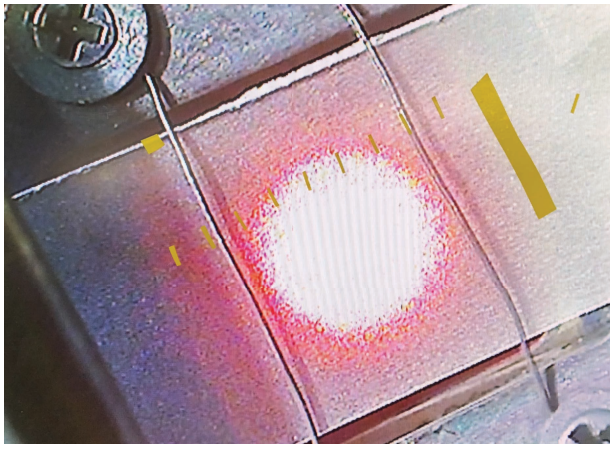

Figure 3.3: Heating laser spot on a semi-transparent sapphire diffuser used for heating laser focusing and positioning.

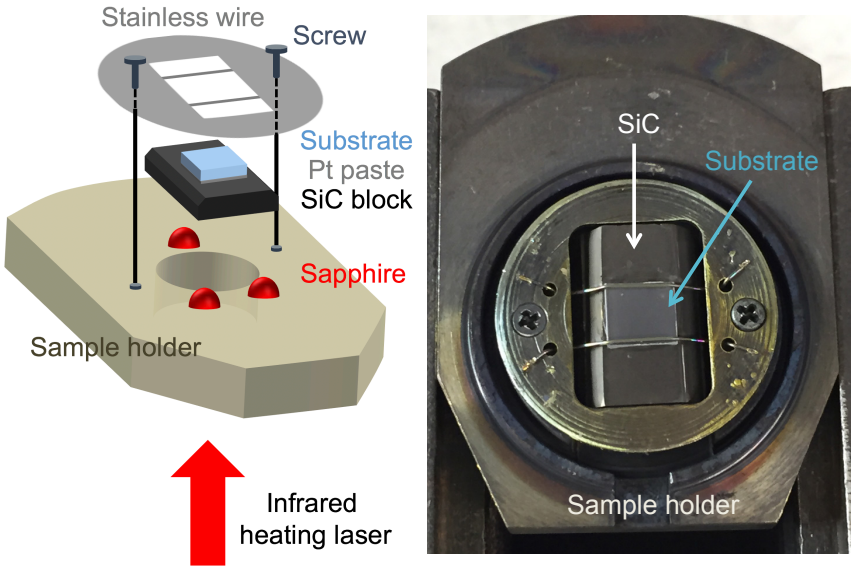

Figure 3.4: Sample holder construction and a photograph of a $SrTiO_3$ substrate mounted in the sample holder.

Figure 3.5: LabVIEW control panel for monitoring and controlling the PLD process parameters.

• **Reflection high-energy electron diffraction (RHEED)**

The chamber was equipped with an *in situ* surface monitoring system using reflection high-energy electron diffraction (RHEED), operated at 25 kV. The intensity of the specular beam was captured with a charge-coupled device (CCD) video camera during a deposition for real-time analysis. These high energy electrons have a wavelength of about $\lambda = h/\sqrt{2m_0eE}$ ~8 pm, which is much smaller than the lattice constant of 0.4 nm. Additionally, the electron beam hits the sample surface at grazing incidence, usually at an angle of about 2° from the sample surface. As a result, the electron penetration depth is only a few atomic layers, and diffracted or reflected electrons contain mostly surface-specific information of the film structure.

Figure 3.6 shows a schematic diagram of the RHEED system with two sets of beam deflection coils. The measurement point on the sample surface can be adjusted by using this magnetic deflection coil system. The first set of coils is on the RHEED electron gun. The second set of coils is located close to the point where the electron beam enters the vacuum chamber, allowing the incident angle of the beam to be changed rapidly under computer control. This system can be used to obtain the surface information over the entire area of a 10 mm substrate by scanning the beam position laterally. The beam movement is synchronized with the camera, which means that the diffraction monitoring software can provide a quasi-real-time view of growth over the whole substrate surface.

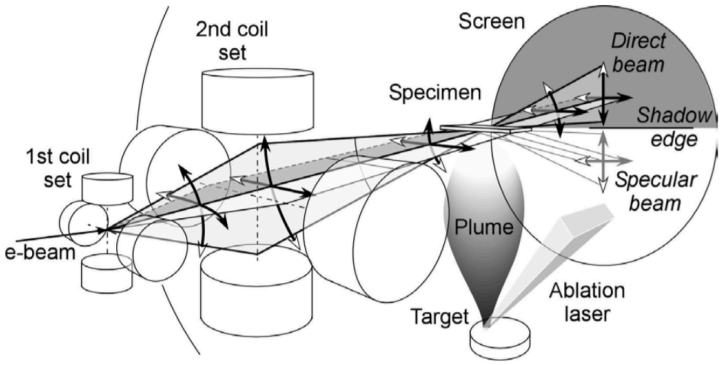

Figure 3.6: Schematics of the scanning RHEED system. The electron beam passes through two sets of deflection coils, enabling flexible beam direction steering including lateral, rocking, and in-plane rotation scans [119].

The diffraction pattern can be used to determine the morphology and the level of disorder at the sample surface. As shown in Fig. 3.7, when a surface has finite domain

size, and the size of domains is smaller than the coherence length of the electron beam, the RHEED patterns reflect the local atomic-scale disorder in the diffraction patterns [120].

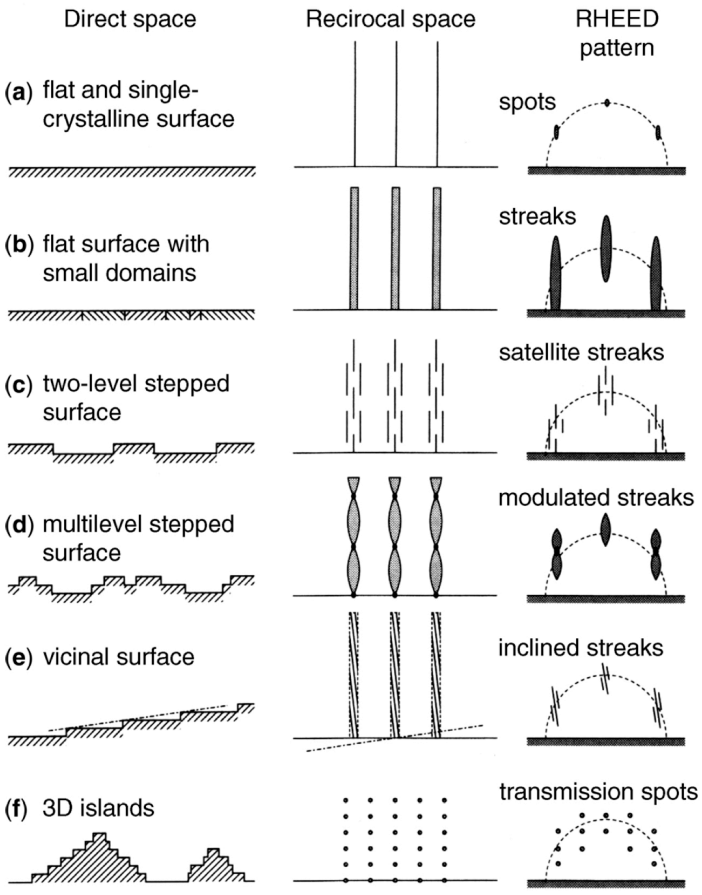

Figure 3.7: Schematics of various kinds of realistic surfaces, in real-space morphology, in reciprocal space, and their RHEED patterns [120].

Another type of information that can be extracted from a RHEED image is the roughness of the sample surface. To a good approximation, the intensity of the specular reflection spot is proportional to the surface flatness. During layer-by-layer crystal growth, the surface roughness varies periodically, once for each unit cell layer that is grown (Fig. 3.8), and the diffraction intensity oscillations can be used to determine the thickness of the film simply by counting the number of oscillations [121]. In PLD, generally, a single unit cell layer is deposited in a few tens of ablation shots, which allows fractional coverage control of an atomic layer with an accuracy of about 5

percent.

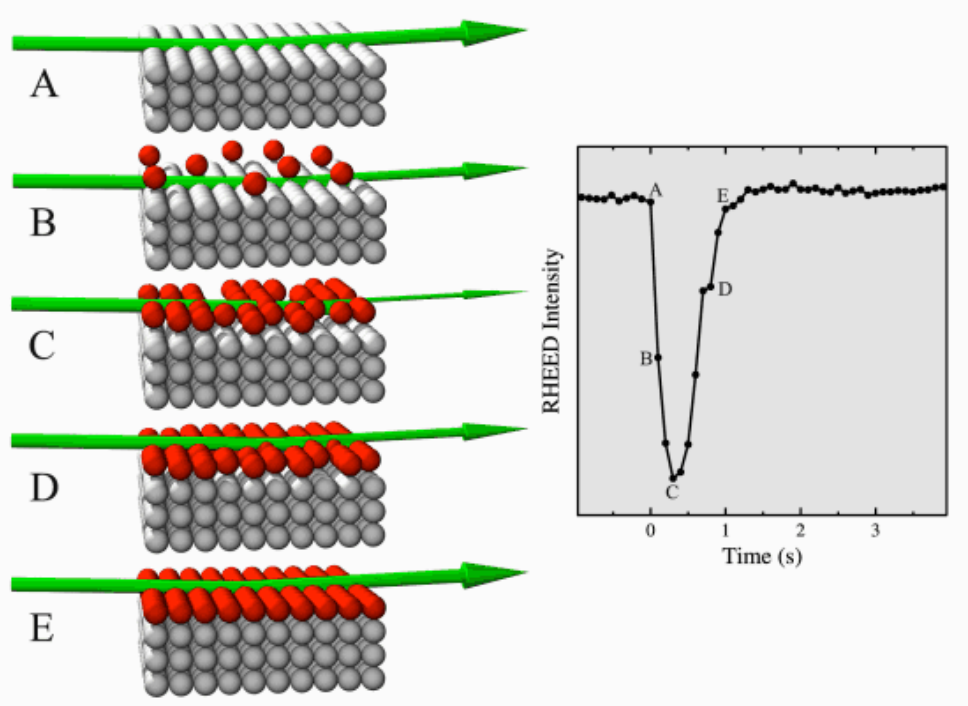

Figure 3.8: RHEED specular beam intensity as a function of surface roughness during the growth of a single unit cell layer of homoepitaxial $SrTiO_3$ [122].

3.2.2 $SrTiO_3$ substrate preparation

To study the behavior of carriers in two-dimensional interface layers in heterostructures, the starting substrate crystal surfaces need to be atomically flat with a regular step-and-terrace surface morphology. Additionally, for $SrTiO_3$ heterointerfaces, it has been reported that the transport properties are strongly dependent on the terminating atomic layer of the perovskite structure. The whole procedure of sample fabrication is illustrated in Fig. 3.9, including surface preparation, film fabrication, and post-annealing.

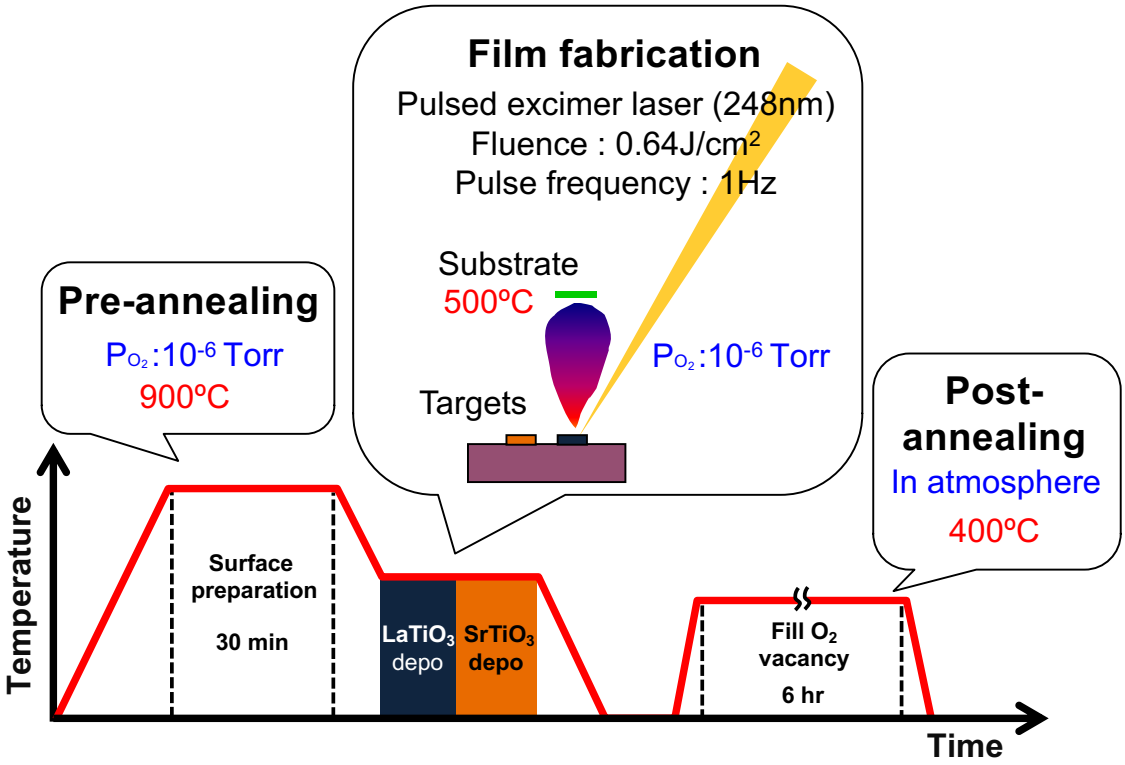

Figure 3.9: Time-temperature diagram of the pre-annealing, deposition, and post-annealing procedures for heterostructure fabrication.

All thin film sample used in this study were deposited on 0.2° miscut $SrTiO_3$ (001) single crystal substrates from Shinkosha. The miscut substrates were used to maintain a uniform surface terrace width and a consistent step edge direction for all samples. The expected step terrace width is 0.4 nm / tan(0.2°) ≃ 110 nm, which is clearly observed in AFM images that will be discussed later. The substrates were chemically etched in buffered NH_4F-HF (BHF) to eliminate segregated Sr and to obtain a uniform TiO_2 termination layer [26, 123]. The purchased substrates size was 15 mm × 15 mm × 0.5 mm.

This thickness of the $SrTiO_3$ substrate is suitable for direct back-gating experiments at low temperatures without further processing.

The supplied $SrTiO_3$ substrates were cleaned twice in acetone for 5 min each under ultrasonic agitation. The washed substrate crystals were blow-dried in nitrogen, attached onto the polycrystalline SiC susceptor blocks by platinum paste (Fig. 3.4) and dried at 200°C for 30 minutes.

Before deposition, the substrates were pre-annealed in the deposition chamber at 900 to 950°C and an oxygen pressure of 10^{-6} to 10^{-5} Torr for 10 to 30 min until a streak-free RHEED pattern was obtained. High-temperature pre-annealing removes carbon contamination from the surface, and recrystallizes the $SrTiO_3$ substrate surface, forming straight step edges that are separated by atomically flat terraces as shown in Fig. 3.10 [124].

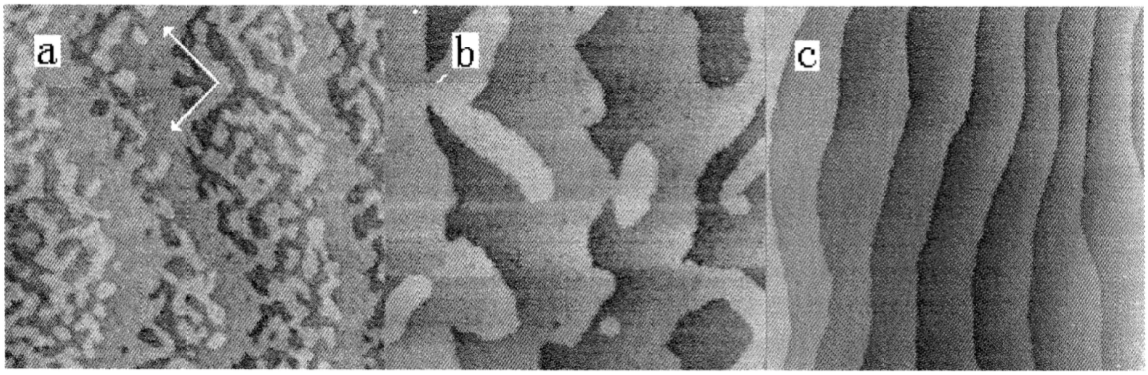

Figure 3.10: $SrTiO_3$ step edge structure at (a) 630°C, (b) 721°C, and (c) 793°C as measured by scanning tunneling microscopy. Image width is 115 nm in (a) and (b), and 265 nm in (c) [124].

The RHEED patterns change systematically during pre-annealing, as shown in Fig. 3.11. The as-supplied substrate shows sharp diffraction spots on the 0-order Laue circle, indicating that the surface is flat and has low structural disorder. Unfortunately, this surface is not thermally stable and has to be recrystallized by annealing. Upon increasing the temperature above 500°C, the spots turn into broader streaks, which shows that the surface structure is starting to change, forming small domains on the surface, while on average, the surface remains flat. The surface crystallization process can be completed by heating the substrate at 900°C for a few minutes. Sharp diffraction spots are then quickly recovered, indicating that an atomically well-ordered surface has been obtained. It should be noted that these numbers apply for the particular 0.2°

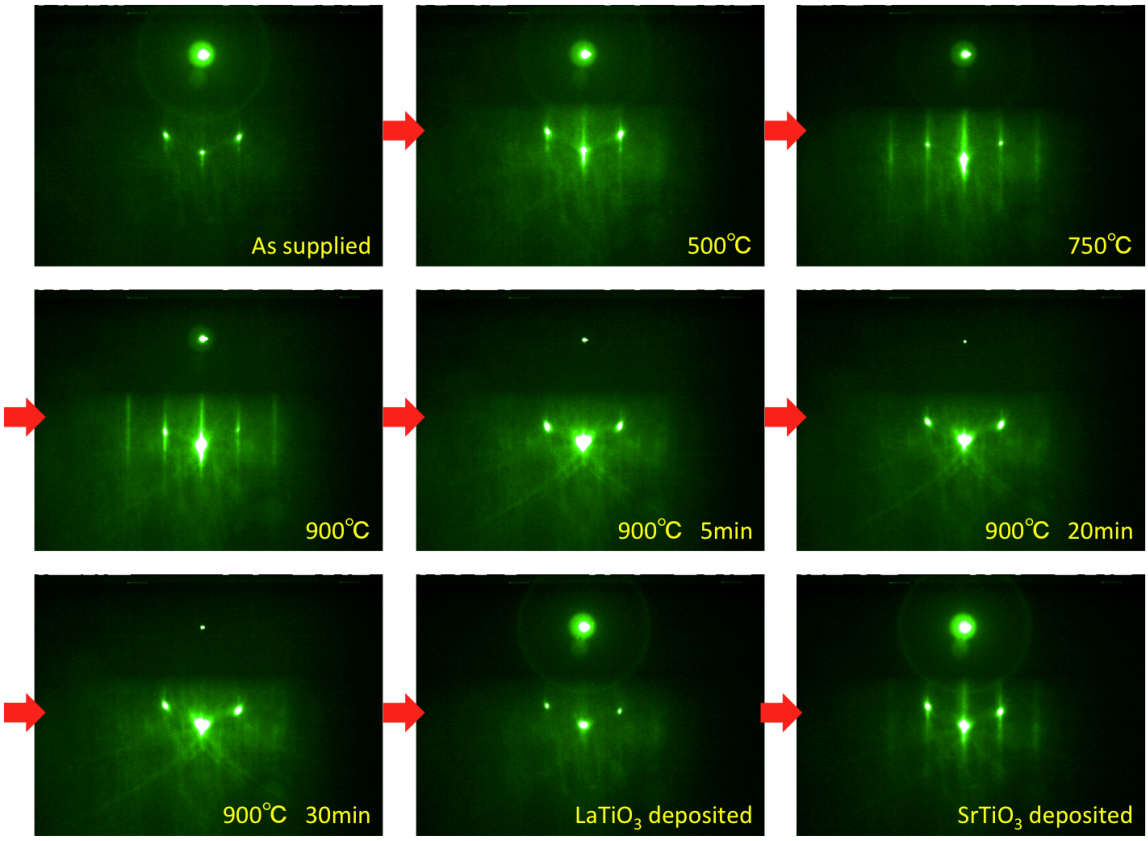

Figure 3.11: A sequence of RHEED images recorded during the substrate pre-annealing and heterostructure growth.

miscut substrates with a 110 nm terrace width. For lower miscut angles, the terraces would be wider, and either longer annealing times or higher temperatures would be needed, which would, however, increase the density of Sr vacancy related defects.

After deposition, the intensity of the entire RHEED pattern becomes slightly weaker and a streak pattern reappears. This level of surface disorder corresponds to the typical layer-by-layer growth mode of a thin film. The substrate annealing temperature has a significant effect on the resistivity of the heterostructures, as will be discussed later.

3.2.3 $LaTiO_3$ deposition

Thin $LaTiO_3$ doping layer were grown on the pre-annealed $SrTiO_3$ substrates. The substrate temperature was maintained at 500°C during the entire deposition at an oxygen pressure of 10^{-6} Torr. A sintered $La_2Ti_2O_7$ polycrystalline target was ablated

with a KrF pulsed laser at a pulse rate of 1 Hz and a fluence of 0.6 J/cm^2.

As discussed in Chapter 2, the physical properties of $LaTiO_x$ ($3 \leq x \leq 3.5$) are sensitive to the oxygen content[91]. The optimal growth conditions for the $LaTiO_3$ growth by PLD have been reported in several papers[125, 126, 102]. In this thesis work, the film growth parameters were selected based on the phase diagram [126] shown in Fig. 3.12. The boundary between $LaTiO_3$ and $La_2Ti_2O_7$ is located at oxygen pressure of $\sim 1 \times 10^{-4}$ Torr. Ohtomo *et al.* noted that below $\sim$ 6 unit cells of $LaTiO_x$, perovskite layers can be stabilized that are completely free of (110) faults, which is the reason why the maximum $LaTiO_3$ layer thickness in this work was set at 5 unit cells. The film thickness was measured by monitoring RHEED specular intensity oscillations during deposition. The layer-by-layer growth mode was confirmed by observing RHEED specular beam intensity oscillations as shown in Fig. 3.13.

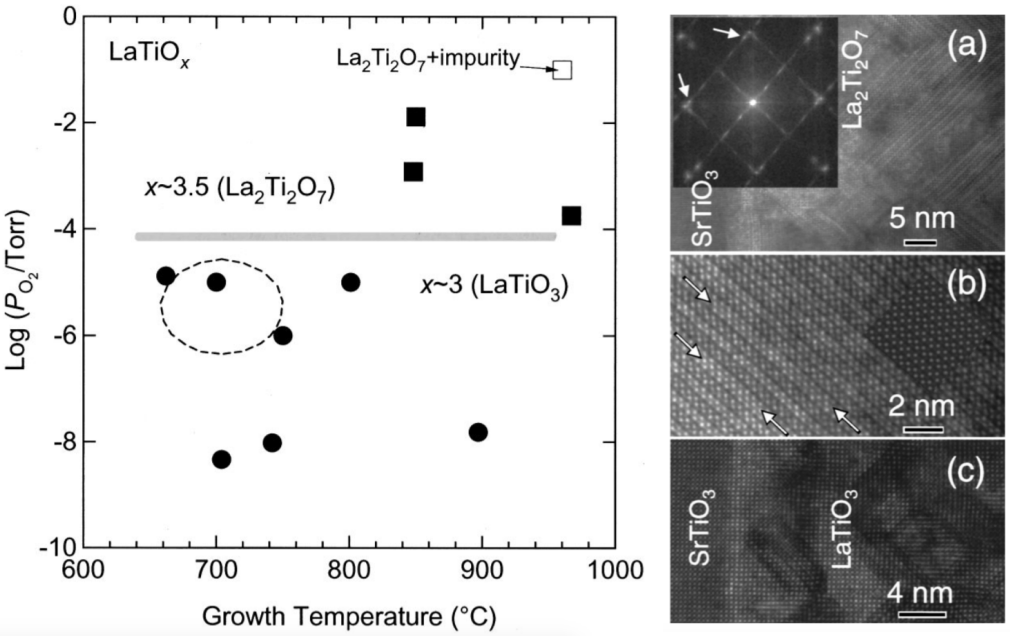

Figure 3.12: (Left) Growth phase diagram for the oxygen partial pressure and growth temperature for $LaTiO_3$ (circles) and $La_2Ti_2O_7$ (squares). The gray line marks the optimal growth conditions for $LaTiO_3$. (Right) ADF-TEM images of $La_2Ti_2O_7$ [(a) and (b)] and $LaTiO_3$ (c) thin films. Faults in the $La_2Ti_2O_7$ film are marked with arrows [126].

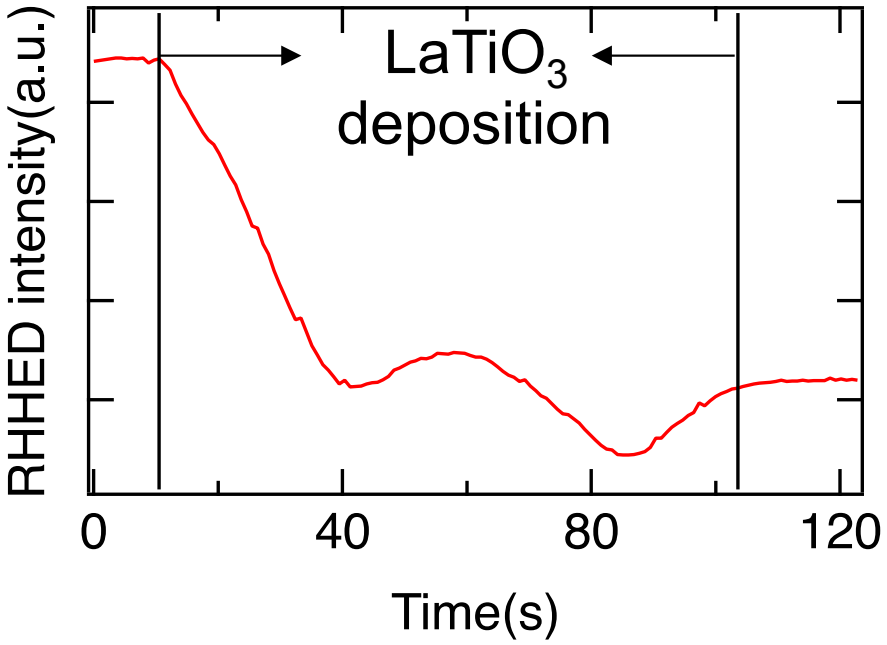

Figure 3.13: RHEED specular beam intensity oscillation observed during the initial growth of 2 unit cells of a $LaTiO_3$ film.

3.2.4 Cap $SrTiO_3$ deposition and post-annealing

The heterostructures were capped with a $SrTiO_3$ layer that was grown immediately on top of the $LaTiO_3$ film. In order to eliminate the oxygen vacancies created during film growth, the heterostructures were post-annealed in air. Although it is possible that the post annealing $LaTiO_3$ films may cause oxidation the formation of the $La_2Ti_2O_7$ phase [110], this is not expected to be a problem for the ultrathin layers discussed in this work. The effect of oxygen annealing on the transport properties of $LaTiO_3$ films is shown in Fig. 3.14, which shows that capping of $LaTiO_3$ films is necessary to avoid strong surface depletion that has been observed to occur on the surface of metallic La-doped $SrTiO_3$ thin films [110, 111]. To eliminate these effects, an approximately 10 nm (25 u.c.) thick $SrTiO_3$ capping layer is required.

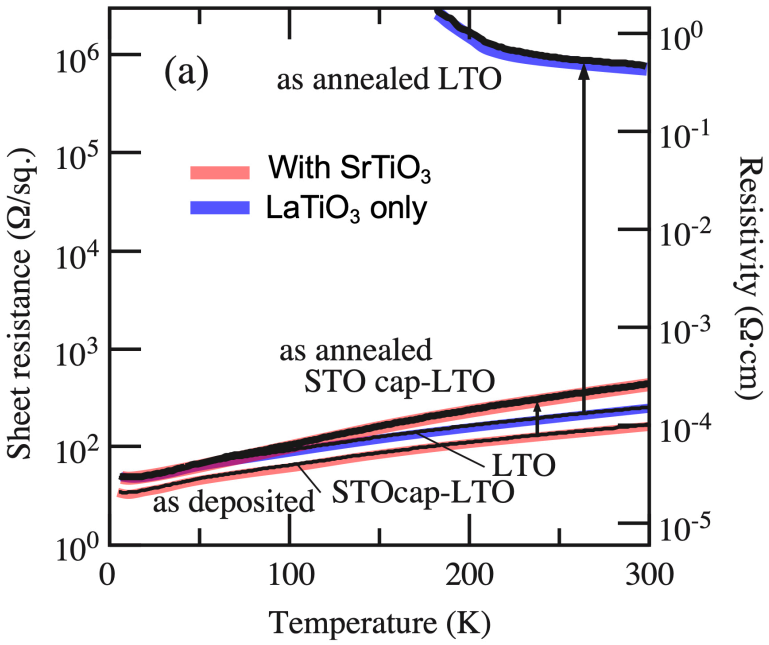

Figure 3.14: Sheet resistance of 60 Å $LaTiO_3$ films on $SrTiO_3$. An uncapped film became insulating after annealing in air, while a capped film remained metallic [110].

The same deposition conditions as used for the $LaTiO_3$ film growth were used for the $SrTiO_3$ cap layer growth. The substrate temperature was maintained at 500°C during the entire deposition time at an oxygen pressure of 10^{-6} Torr. A sintered $SrTiO_3$ single crystal target was ablated with a KrF pulsed laser at a pulse rate of 1 Hz and a fluence of 0.6 J/cm^2. The layer-by-layer mode growth was confirmed by observing RHEED specular beam intensity oscillation shown in Fig. 3.15. The growth rate was approximately 45 pulses/uc for $LaTiO_3$ and 25 pulses/uc for the $SrTiO_3$ cap layers.

Finally, the films were post-annealed in air at 400°C for 6 hours in a furnace to fill the oxygen vacancies created during the heterostructure growth.

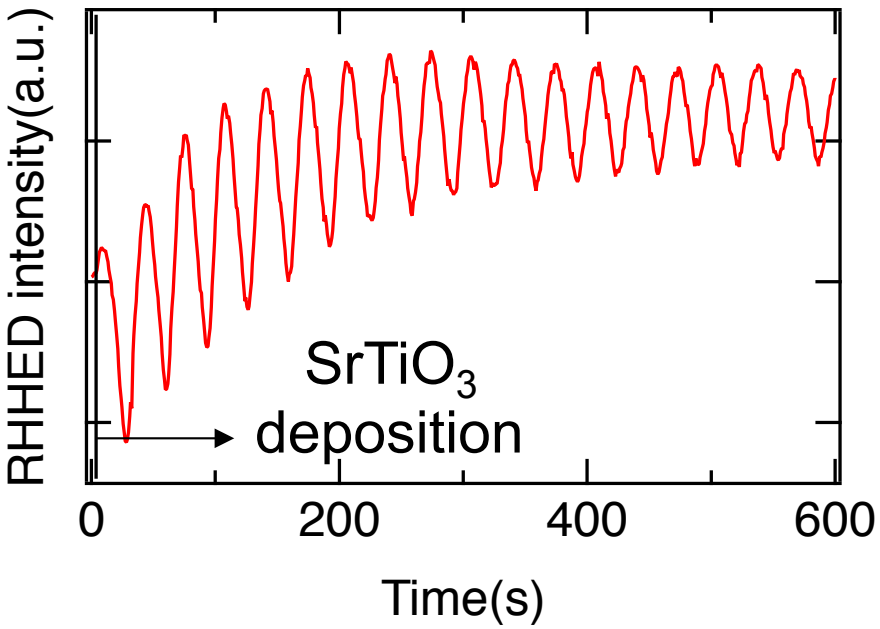

Figure 3.15: RHEED specular beam intensity oscillation during the initial growth of 800 pulses (approximately 27 unit cells) of the $SrTiO_3$ cap layer.

3.3 Characterization of the sample

3.3.1 Atomic force microscopy

Atomic force microscopy (AFM) is a form of scanning probe microscopy that senses the interatomic forces between a probe tip and a sample and can be used to visualize surface features with atomic-scale resolution. A Shimadzu SPM-9600 microscope(Fig. 3.16) was

used in both contact mode and non-contact mode in this work. The spatial resolution of this microscope is about 10nm. Schematic illustration of the operation of an AFM is shown in Fig. 3.17.

Contact mode

Contact mode AFM detects the contact force between the tip of the cantilever and the sample. When scanning in a horizontal direction, the vertical deflection of the cantilever is maintained at a preset value that defines the desired contact force. The sample height is adjusted under PI control to maintain the desired contact force. The sample height data as a function of the scan position is used to construct the surface topography image. Surface chemical contrast can be obtained by monitoring the lateral friction force that the tip is subjected to during a scan over the sample surface.

Non-contact mode

In non-contact mode measurement, the AFM cantilever vibrates near the sample surface close to its resonant frequency. The distance between the AFM tip and the surface is maintained at a constant value by monitoring the amplitude of the vibration, which depends on the interaction strength between the tip and the surface. The topography image is constructed in the same way as for the contact mode operation. Additionally, the oscillation phase can be recorded, which is sensitive to sharp edges on the surface and can also detect changes in the chemical composition of the surface.

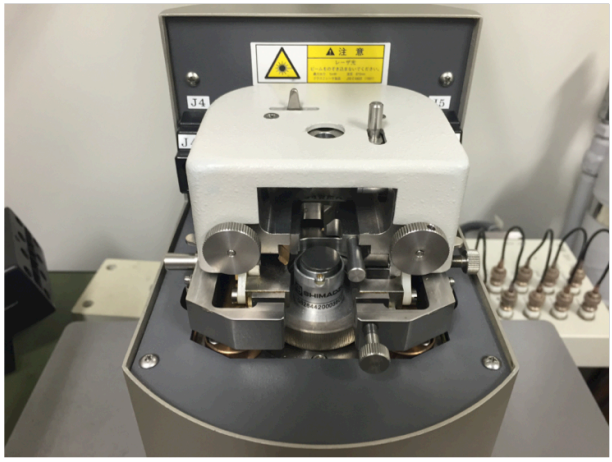

Figure 3.16: Shimadzu SPM-9600 microscope.

Fig. 3.18 shows AFM images of heterostructures consisting of 2 unit cells of $LaTiO_3$ grown on $SrTiO_3$ substrates and capped with a 25 u.c. layer of $SrTiO_3$. The substrates were annealed at various temperatures between 750°C and 950°C to obtain a regular

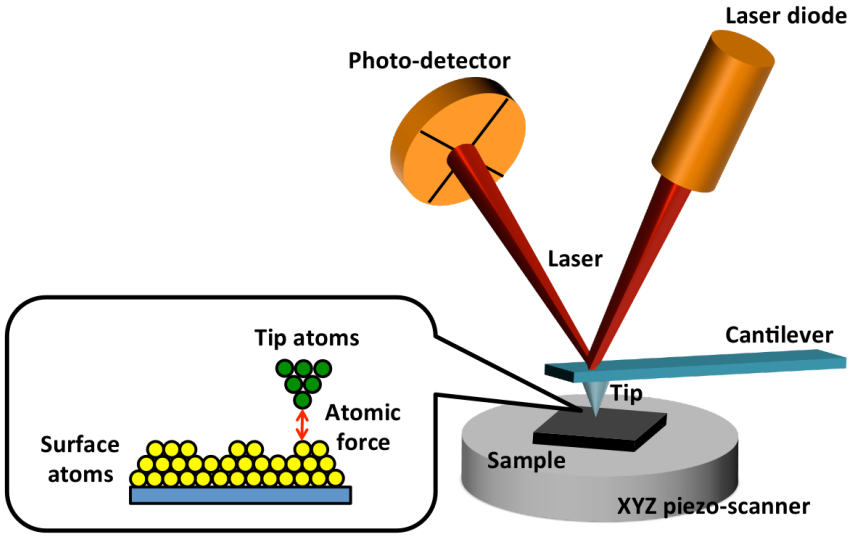

Figure 3.17: Schematic illustration of the operation of an atomic force microscope.

step structure. The annealing time was 10 minutes at an oxygen pressure of 10^{-6} Torr. The AFM image of the sample pre-annealed at 750°C is smooth, but the step edges are meandering. This problem can be solved by increasing the annealing temperature to 850°C. It should be noted that while AFM images have atomic-scale vertical resolution, the lateral resolution is on the order of 10 nm and true atomic-scale surface order cannot be ensured purely on the basis of AFM images. Previous STM studies have shown how the surface morphology changes on the atomic scale during $SrTiO_3$ annealing (Fig. 3.10). At low temperature, the mobility of surface atoms is not sufficient for macroscopic step edge rearrangement. From the measured AFM images, I find that an annealing temperature higher than 900°C is required to obtain atomically smooth regular heterostructure morphologies. Even higher temperatures may produce even sharper surface images, but too high annealing temperature should also be avoided to avoid the formation of Sr or O vacancies in the surface layer of the substrate. Surface defects can promote cation interdiffusion and thus increase disorder at the heterostructure interface. I therefore selected the following pre-annealing process parameters: 900°C, 30 minutes in oxygen at 10^{-6} Torr.

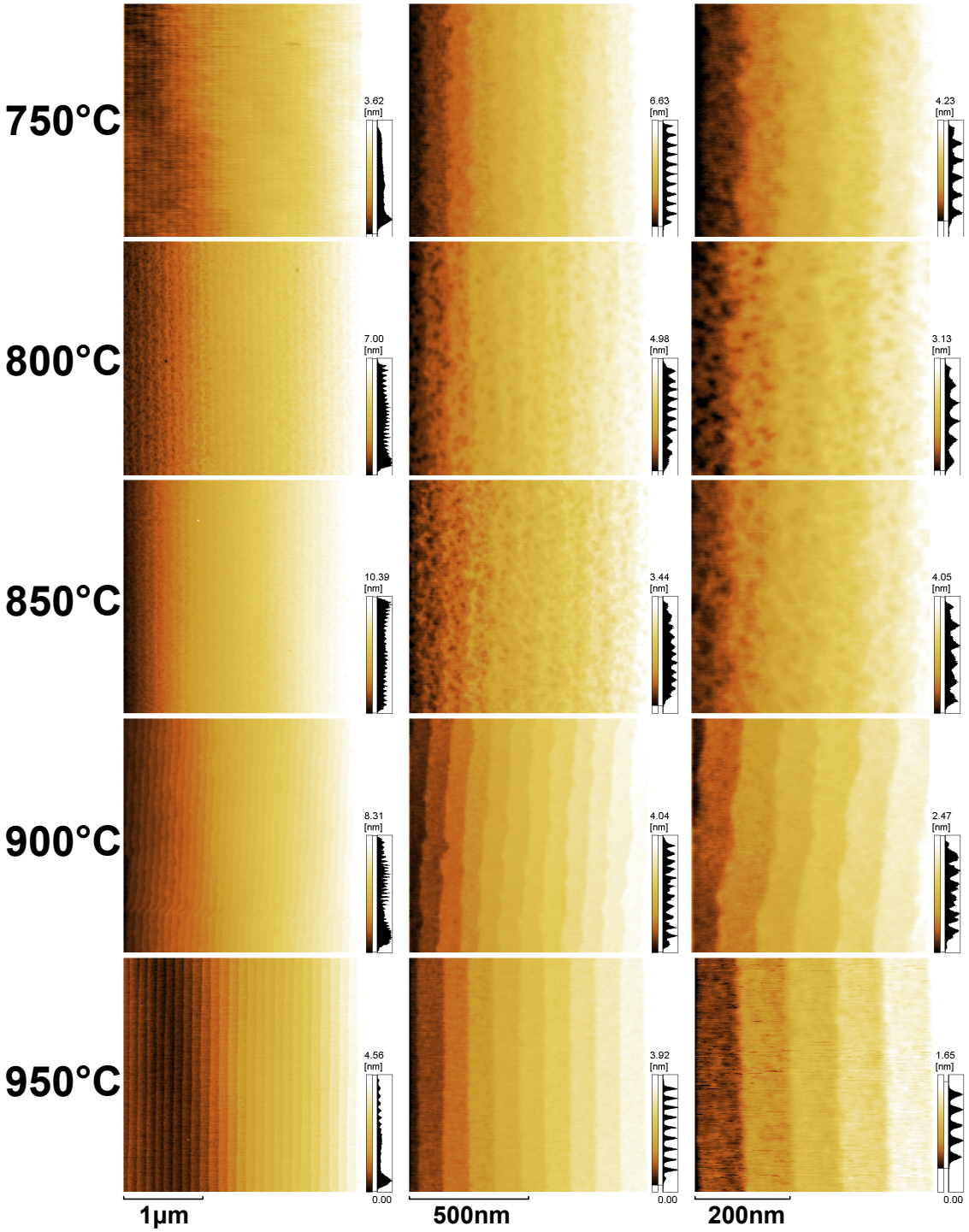

Figure 3.18: AFM surface images of capped heterostructures grown on $SrTiO_3$ substrates that had been pre-annealed at several temperatures between 750°C and 950°C for 10 minutes.

3.3.2 Surface profiler

A stylus profilometer is an instrument used for film thickness measurement. In this measurement, a sharp scanning tip is dragged across the sample surface while measuring the height or trench profile of the sample. The difference from a scanning probe microscope is that the profilometer measures a single line scan at a lower resolution than an AFM, but can determine the height variations over centimeter distances and micrometer heights.

When a thin film sample is deposited through a stencil mask, the sample will have some regions where the substrate surface is exposed. The film thickness can be determined from the step height at the edge of such a stencil mask pattern. Fig. 3.19 shows a photograph and a surface step viewing of the stylus profilometer, Dektak 6M, used in this work.

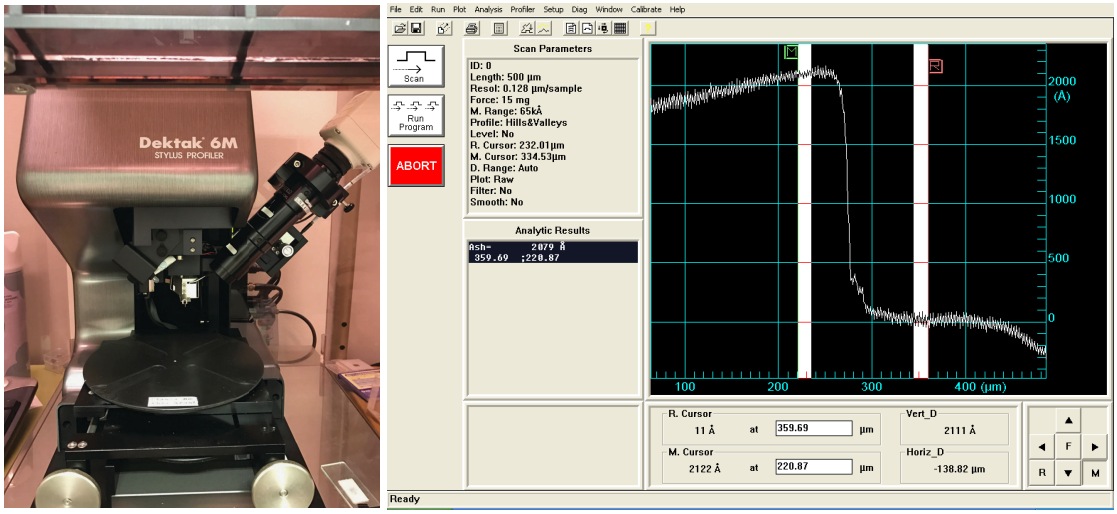

Figure 3.19: A photograph and a surface step viewing of the Dektak 6M profilometer.

3.4 Transport and magnetotransport measurements

3.4.1 Transport

The fabricated heterostructures were attached to 44-pin ceramic packages by double-side tape for low-temperature measurement. Because of the moderately low resistance values of $\sim 200\ \Omega$ at low temperature, a four-point measurement technique was used to eliminate the influence of the contact resistance. Aluminum wires were connected

to the conducting interfaces with an ultrasonic wedge wire bonder 7476D (West-Bond). The pressure of the wire bonder is sufficient to crack the sample surface and make contact between the bonding wire metal and the conducting buried interface through the $SrTiO_3$ capping layer. The work function of aluminum is 4.1 eV, close to the electron affinity of $SrTiO_3$(~4.0 eV[127]). Thus aluminum wires can form an Ohmic contact with the *n*-type $SrTiO_3$ crystal. After bonding, the ceramic package was attached to a low-temperature dipping probe and slowly dipped into a liquid helium vessel to measure transport behavior down to 4.2 K.

3.4.2 Magnetotransport

The magnetoresistance and Hall effect were measured in a superconducting magnet cryostat (Physical Property Measurement System, PPMS : Quantum Design Inc. (Fig. 3.20)) The sample environment in the PPMS allows temperature control in the range from 2 K to 300 K and magnetic field of up to ±9 T can be applied.

The Hall bars were formed by cutting into the heterostructure surfaces with a mechanical milling machine (FP-21T : MITS Electronics Inc.) using a diamond point pen cutter (Fig. 3.21). The milling machine was set to cut lines into the sample surface to a depth of few μm, which is sufficient to penetrate through the conducting layer deep into the insulating substrate. Since the delta-doped $LaTiO_3$ thickness is just few atomic layers, the orientation of the substrate surface steps may affect the current flow. To investigate this effect, two perpendicularly directed Hall bars were cut in each sample with the current flow direction in the two Hall bars being either parallel or perpendicular to the surface steps. The step direction was determined for each sample by AFM measurement.

Figure 3.20: Physical property measurement system.

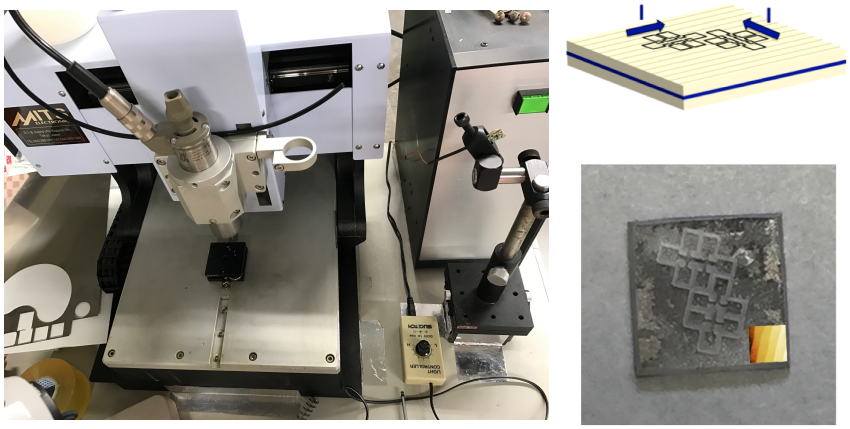

Figure 3.21: Mechanical milling machine and Hall bar geometry.

3.4.3 Back-gating

The back-gating experiments were performed with the help of Osada laboratory, Institute for Solid State Physics. A copper sheet was attached onto the 44-pin ceramic packages as the back-gate electrode and the heterostructure samples were mounted on the copper sheet with silver paste (Fig. 3.22). After making contact to the heterostructure by Al wire bonding, the ceramic package was inserted into a low-temperature dipping probe and slowly dipped into a liquid helium vessel, cooling the sample down to approximately 4.2 K.

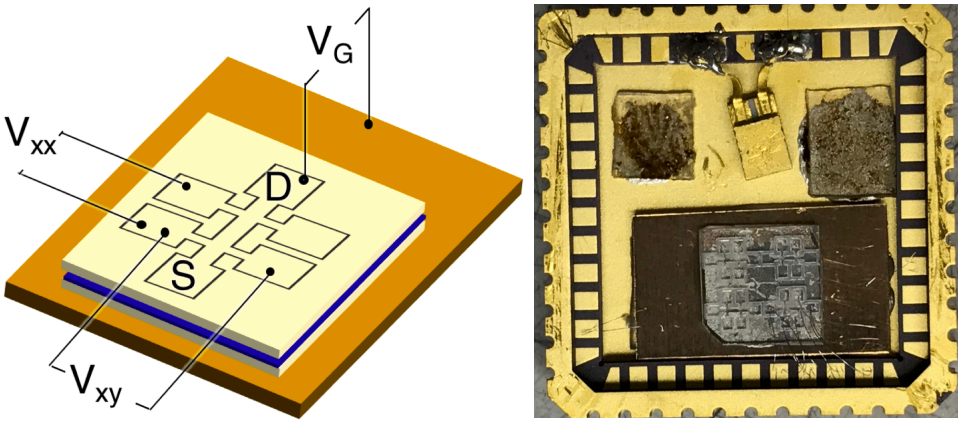

Figure 3.22: (Left) Sample configuration and gate biasing circuit. The Drain electrode was grounded. (Right) A photograph at the sample on a ceramic carrier.

3.4.4 Light illumination

In gated transport measurements, carriers that normally accumulate close the interface may be trapped at defect sites in the substrate. Such trapped carriers can be released by thermal or optical excitation. Transport measurements were therefore also done under light illumination in an optical cryostat. The excitation wavelength was between 300 ~ 1200 nm, obtained from a Xe lamp and a monochromator. A photograph of the cryostat and the large optical window can be seen in Fig. 6.2. In this vacuum chamber, the sample temperature could be reduced to 10 K.

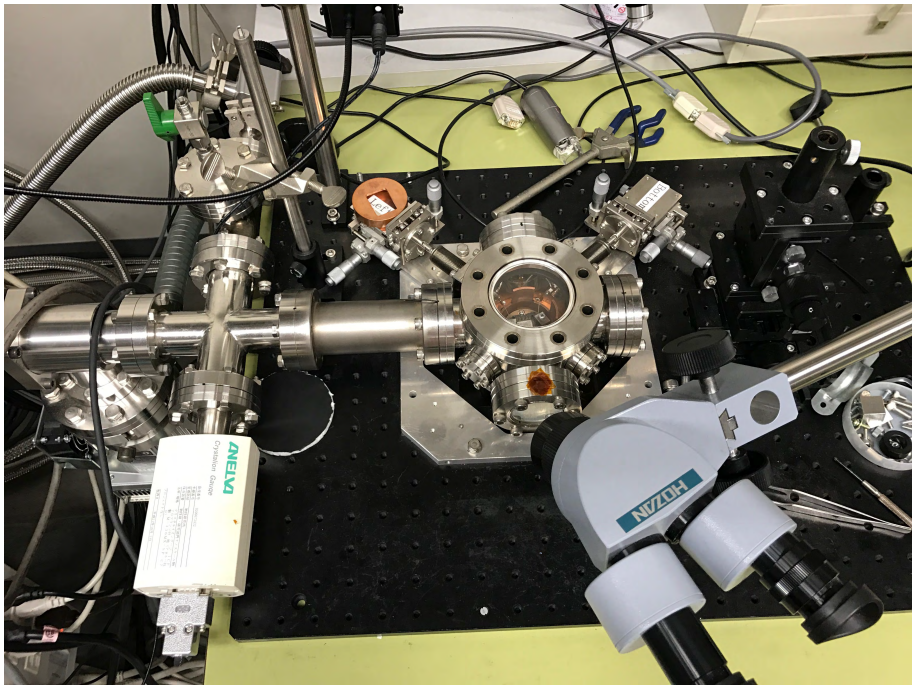

Figure 3.23: A photograph of the optical cryostat used in carrier detrapping experiments.

Chapter 4

Transport properties of $LaTiO_3/SrTiO_3$ interfaces

4.1 Introduction

This Chapter describes the conductivity found at $LaTiO_3/SrTiO_3$ heterointerfaces. Particular attention in this Chapter is paid to the film thickness dependence, i.e., changing the La doping level and utilizing the effect of surface depletion through the change of the $SrTiO_3$ capping layer thickness.

As discussed in Section 2.6.3, the conductivity in the $LaTiO_3/SrTiO_3$ system can be tuned from a metallic to an insulating state by a simple adjustment of the total number of La atoms in the delta-doping layer, i.e., the total carrier number. I also show that small changes in the pre-annealing conditions of a $SrTiO_3$ substrate can have a dramatic effect on the low-temperature sheet resistance of the heterostructures, which means that the transport characteristics are strongly affected by point defects in the topmost unit cell layer of the $SrTiO_3$ substrate.

This part of the work was recently published in Applied Physics Letters [128].

4.2 $LaTiO_3$ thickness effects

The main aspects of the delta-doped heterostructures are shown in Fig. 4.1. The source of the carriers in the otherwise insulating $SrTiO_3$ layers is the substitution of one or more atomic SrO layers in the $SrTiO_3$ lattice with LaO layers. Since La always exists in a 3+ state in the perovskite lattice, it is obvious that the total number of carriers in the

system must be equal to the number of La atoms, which is known from the deposited $LaTiO_3$ layer thickness with a precision of about 5%.

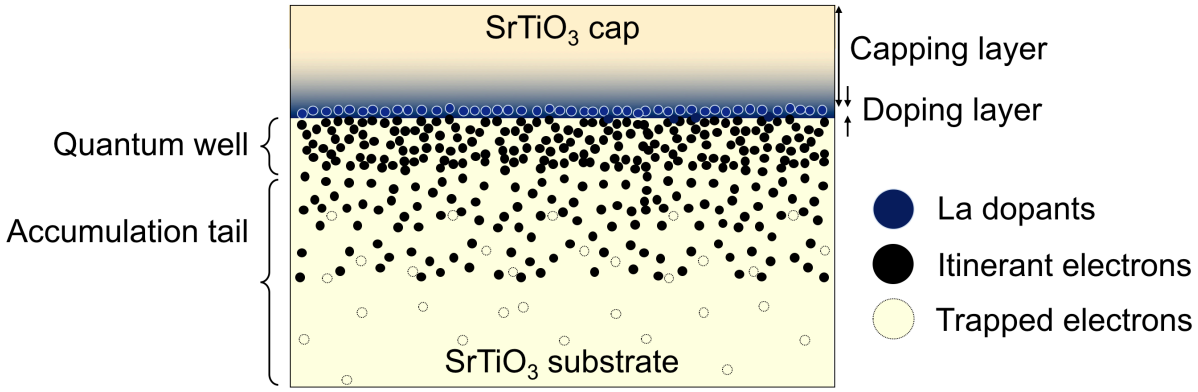

Figure 4.1: $LaTiO_3/SrTiO_3$ heterostructure.

As was discussed in the materials Section, the presence of the $SrTiO_3$ capping layer is essential for avoiding surface depletion effects and for metallic conductivity to be observed. To discuss how the La content of the structure affects the transport behavior, all heterostructures discussed here were capped with a 25 unit cell (10 nm) $SrTiO_3$ layer, which is sufficiently thick to eliminate the effect of surface depletion on the heterostructure transport.

As was shown in Chapter 3, all interfaces discussed here are two-dimensional in the sense that the initial substrate surfaces are atomically flat with a step-and-terrace morphology and the same morphology is replicated on the capped heterostructure surface. This means that any structural roughness at any of the interfaces cannot extend beyond a single atomic layer, which corresponds to 2Å.

One of the motivations of this thesis work was to study the effect of the sheet carrier density on the appearance of possible magnetic or charge order effects at the interface. It is thus useful to start by discussing the lower La doping limit at which metallic conductivity appears in $LaTiO_3/SrTiO_3$ heterostructures.

As shown in Fig. 4.2, all heterostructures with nominal $LaTiO_3$ layer thicknesses of 0.5 unit cells or more were metallic and exhibited a T^2 temperature dependence, as expected for electron-doped $SrTiO_3$. For doping layers with fractional coverage below about 0.5 unit cells, the analysis of doping level-dependent conductivity must take into account the spatial inhomogeneity of the doping layer. Since the heterostructures were grown at a very low temperature of 500°C to avoid bulk diffusion, it means that

lateral surface diffusion is also limited and at low layer coverages, it is likely that the interface consists of metallic nanoscale islands separated by non-metallic regions that may exhibit insulating or possibly hopping conduction. The transition to insulating state that can be seen in the lower panel of Fig. 4.2 is thus likely not a simple Mott-type critical doping level transition, but rather a percolative transition that occurs at a coverage of about 0.3 unit cells.

Since spatial inhomogeneity adds additional complications to the analysis of the transport behavior, only doping layers with coverages of more than 0.5 unit cells were explored further in this work.

For $LaTiO_3$ layer thicknesses above 0.5 unit cells, all heterostructures were metallic and by comparing simply the room-temperature resistivities, the conductivity increases in proportion to the La doping level.

The low-temperature behavior is shown in the inset of the upper panel of Fig. 4.2 and the sheet resistance drop with increasing La doping level replicates the room-temperature behavior. In this set of heterostructures, low-temperature upturns or hints of localization were seen.

For larger $LaTiO_3$ layer thicknesses, the sheet resistance values saturate. For thicker $LaTiO_3$ layers, there is also a risk of nucleating the $La_2Ti_2O_7$ phase [126], which would lead to the loss of surface flatness. The study was thus limited to a maximum doping layer thickness of 5 unit cells.

The resistance ratio between 300 K and the 4 K is about 40 $\sim$ 80, which is significantly smaller than for homogeneous oxygen-deficient $SrTiO_3$ films where the residual resistance ratio can reach $\sim$ 1000, but within the range of values expected for highly-doped Nb:$SrTiO_3$ or La:$SrTiO_3$ films [129, 130]. The residual sheet resistance values of all heterostructures are in the mΩ range which appears to be about an order of magnitude higher than single crystal values, although direct comparison of bulk resistivities is difficult due to the unknown thickness of the conducting layer in a heterostructure.

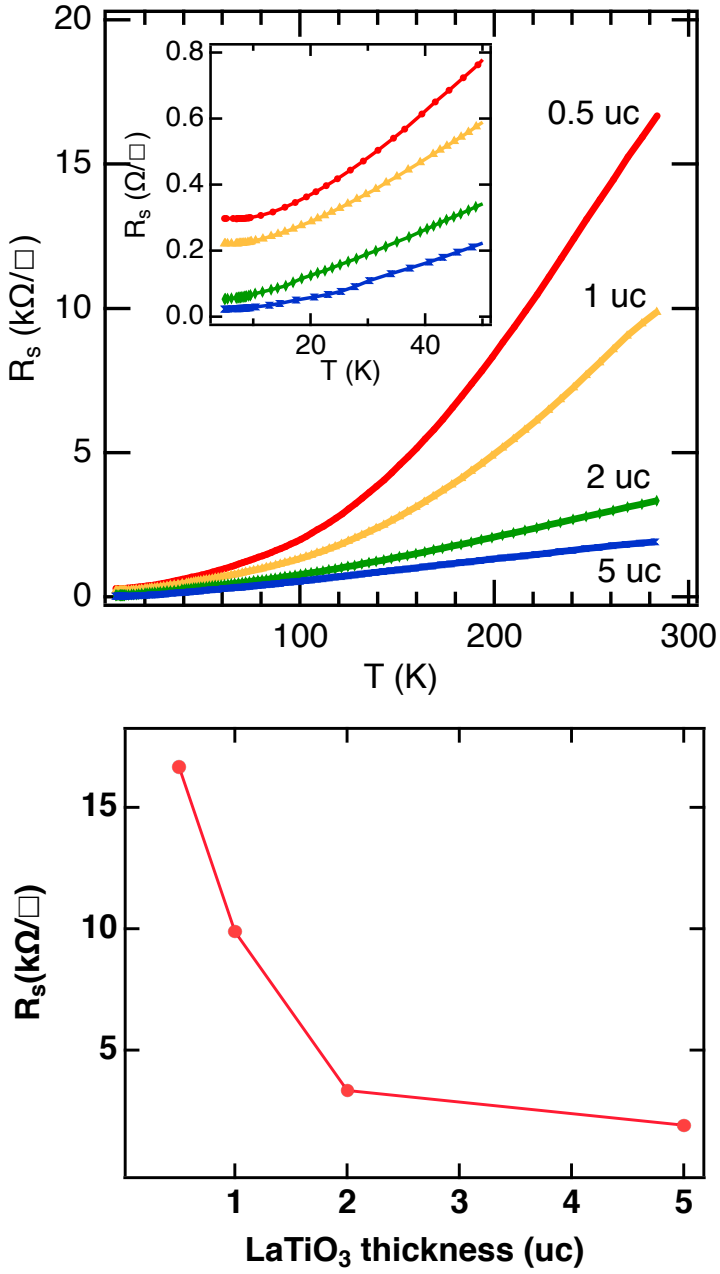

Figure 4.2: (Upper) Temperature dependence of sheet resistance for various $LaTiO_3$ layer thicknesses. The $SrTiO_3$ cap layer thickness was 25 uc. A magnified view of the low-temperature resistance is shown in the inset. (Lower) Extracted sheet resistance values vs $LaTiO_3$ thickness, measured at 300 K.

4.3 $SrTiO_3$ thickness effects

A common feature of $SrTiO_3$ thin films is the phenomenon of surface depletion[111, 131]. As shown in Fig. 4.3, reducing the capping layer width will deplete carriers from the quantum well, leading to an insulating ground state. A gradual reduction of conductivity appears once the cap layer thickness is reduced below 20 uc. A semiconductor-like behavior can be observed for a 10 uc cap layer, but below this thickness, the heterostructures are highly insulating. The microscopic origin of the surface depletion effect has not been determined, but possible reasons are surface cation vacancies or the ubiquitous coating of all surfaces exposed to air with several monolayers of water, which naturally creates a depletion layer on the surface of an *n*-type semiconductor.

Although the need for a capping layer may appear as a nuisance, masking the true characteristics of the heterostructure, the data shown in Fig. 4.3 also suggests a possible use for the effect, namely controlled tuning of the carrier density and perhaps carrier distribution in the $LaTiO_3/SrTiO_3$ heterostructure. Wide-range tuning of carrier density has been demonstrated for the $LaAlO_3/SrTiO_3$ heterostructure with the help of top gating [132], but if such gating is done with a physical gate electrode, the $LaAlO_3$ layer has to be relatively thick, on the scale of 20 unit cells, to prevent leak current injection from the gate electrode to the heterostructure channel. Another option is to use electronic double layer gating with a liquid electrode, but this is incompatible with many practical heterostructure device designs. On the other hand, depletion tuning by changing the thickness of a capping layer is trivially simple. As shown here, the $SrTiO_3$ cap layer thickness can be set to any desired value with better than unit cell precision by simply counting RHEED oscillations during the film deposition.

As shown by the room-temperature sheet resistance plot in the inset of Fig. 4.3, the conductivity behavior no longer depends on the cap layer thickness beyond $\sim$ 20 uc. A conclusion from this data is that the depletion layer thickness in the $SrTiO_3$ cap layer is about 20 unit cells, or about 8 nm.

Due to the strongly temperature-dependent permittivity of $SrTiO_3$, a closer look was taken at the low-temperature transport behavior of heterostructure with various cap layer thicknesses. The $LaTiO_3$ layer thickness was fixed at 2 unit cells for all of these samples. Even when the room temperature sheet resistance values are similar to each other, the plots in Fig. 4.4 show that the low-temperature sheet resistances do not vary systematically with the cap layer thickness, although there is a significant spread of resistance values, with a factor of $\sim$ 2 difference between the lowest and the highest values.

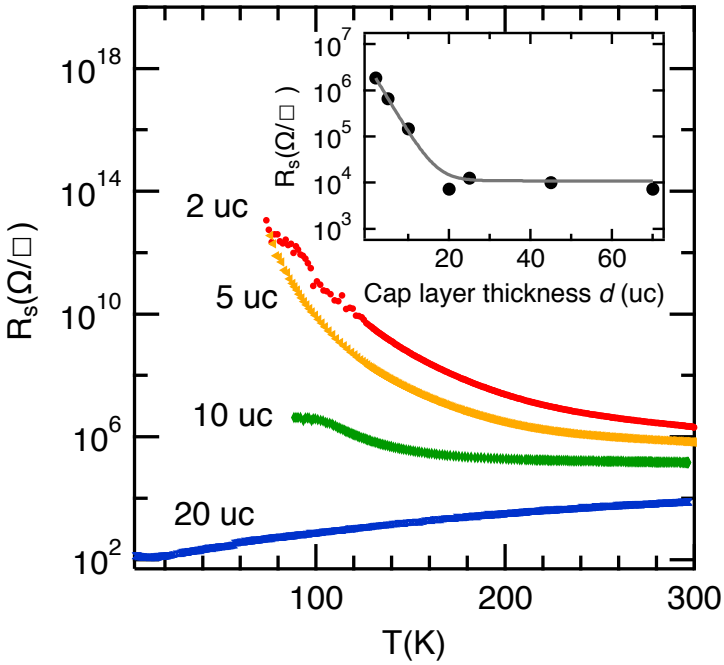

Figure 4.3: Temperature dependence of sheet resistance for heterostructures with various $SrTiO_3$ cap layer thicknesses. The $LaTiO_3$ layer thickness was 1 uc. The inset shows the room temperature sheet resistance as a function of the cap layer thickness. The 2 uc and 5 uc samples were measured in a 2-point geometry, all other samples in a 4-point setup.

There is a clear qualitative difference between the low-temperature resistivity behaviors of the individual heterostructures with some samples (30, 40, and 70 uc $SrTiO_3$) showing a slight resistance upturn below 20 K. One mechanism that can explain such behavior is the Kondo effect, which has been studied in metals doped with magnetic impurities. The $LaTiO_3$ heterostructures may support a magnetic impurity model if La ions at the interface produce Ti atoms with a single unpaired electron in a two-dimensional interface layer.

4.4 Substrate preparation effects

The heterostructures were grown by PLD as described in Chapter 3. The $SrTiO_3$ (001) substrates were annealed at high temperature to obtain flat terraces and approximately equidistant single unit cell steps.

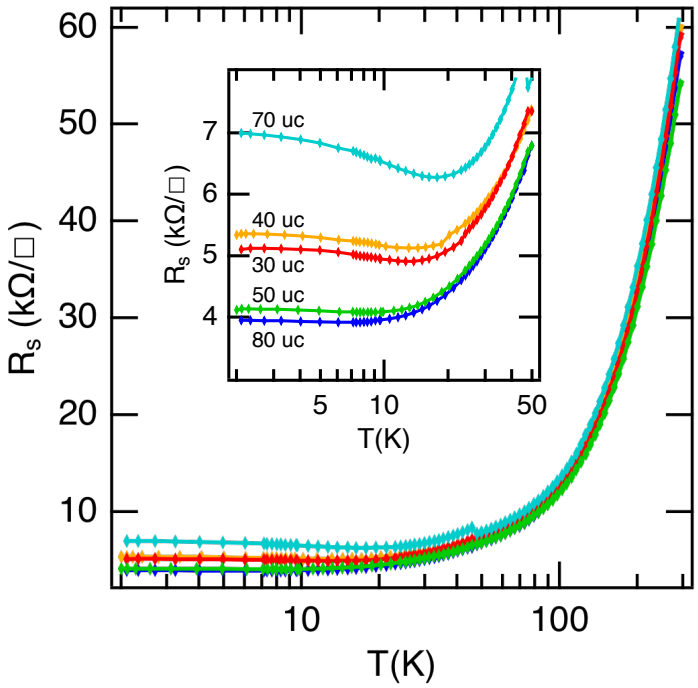

Figure 4.4: Low-temperature sheet resistance behavior for heterostructures with various $SrTiO_3$ cap layer thicknesses. All substrates were pre-annealed until a sharp RHEED pattern was observed.

However, at the same time, long annealing at high temperature and reduced oxygen pressure certainly produces oxygen vacancies in the substrate, which may result in the low-temperature sheet resistance difference that was shown in Fig. 4.4. It is thus necessary to examine the role of the substrate surface preparation as a possible causes for the variation of the low-temperature transport characteristics of the quantum wells.

When preparing a $SrTiO_3$ substrate for film growth, the surface of the substrate has to be recrystallized by moderate heating at low oxygen pressures of below 1 mTorr to prevent Sr segregation [133, 123]. The substrate pre-annealing for all samples was done at 10^{-5} Torr at temperatures between 900°C and 950°C until a sharp streak-free RHEED patterns were observed, usually in about 20 minutes. It should be noted that these numbers apply for the particular 0.2° miscut substrates with a 120 nm terrace width. For lower miscut angles, the terraces would be wider, and either longer annealing times or higher temperatures would be needed.

The substrate annealing temperature has a significant effect on the resistivity of the heterostructures, as shown in Fig. 4.5 (left). An increase of the annealing temperature

from 900°C to 950°C reduced the room-temperature resistance by nearly a factor of three. The annealing time has a similar effect, but the most dramatic change is visible at low temperatures, as shown in Fig. 4.5 (right), increasing the annealing time from 20 to 30 min decreased the 2 K sheet resistance by a factor of ten.

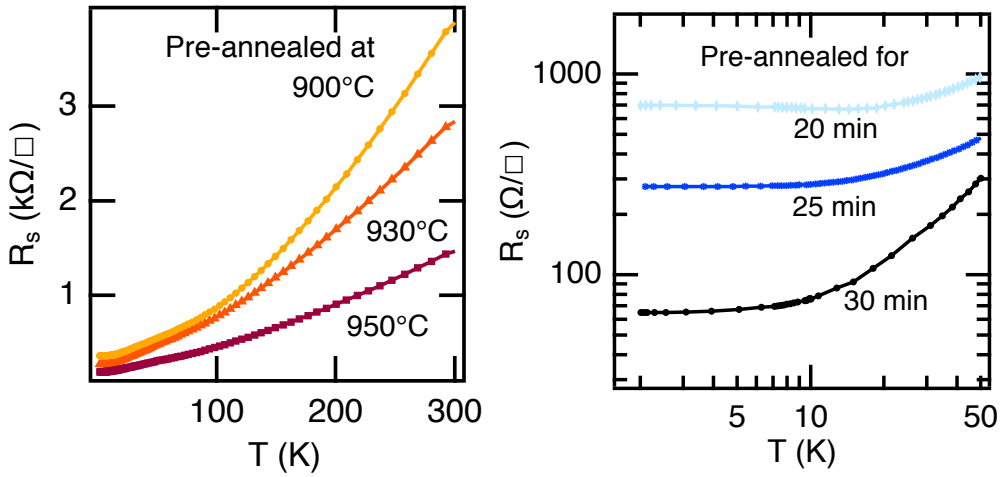

Figure 4.5: (Left) The effect of the substrate pre-annealing temperature on the sheet resistance. (Right) The effect of the substrate pre-annealing time at 900°C.

This behavior appears to be related to the formation of Sr vacancies or oxygen vacancy clusters in the surface layer of the substrate. [133, 134]

4.5 Summary

As a summary of this Chapter, the conductivity of delta-doped $LaTiO_3$ heterostructures can be tuned from a metallic state to an insulating state by a simple adjustment of either the number of La atoms in the doping layer or by adjusting the thickness of a $SrTiO_3$ cap layer. The heterostructures are found to be highly sensitive to minute changes in the $SrTiO_3$ substrate pre-annealing conditions. Several samples show a Kondo-like effect, which may result from Ti atoms with a single unpaired electron, although further work would be needed to prove this.

Chapter 5

Magnetotransport properties of $LaTiO_3$ / $SrTiO_3$

5.1 Introduction

In this Chapter, I discuss the magnetotransport properties of $LaTiO_3$ / $SrTiO_3$ heterostructures. A set of metallic samples was used in these experiments, with samples differing by the number of embedded $LaTiO_3$ layers, i.e., the total carrier number. Hall effect and magnetoresistance were evaluated at several temperatures and magnetic field configurations.

Due to the action of an external magnetic field on electric current, the transport properties of a material may change as a function of the applied field. A typical examples is the Hall effect, which was discovered in the 19th century but is still actively studied, extending the concept to quantum effects. Basically, the Hall effect is caused by the Lorentz force which forces particles carrying current to be subjected to cyclotron motion when a perpendicular magnetic field is applied relative to the direction of the current flow [135].

The equation of motion for a charged particle is in this case

$$m^* \frac{d^2\mathbf{r}}{dt^2} + \frac{m^*}{\tau}\frac{d\mathbf{r}}{dt} = q[\mathbf{E} + (\mathbf{v} \times \mathbf{B})] \ , \tag{5.1}$$

where m^* is the effective mass, τ is the relaxation time, q is the charge of a particle, $\mathbf{E}$ is the electric field, $\mathbf{v}$ is the velocity of the charged particle, and $\mathbf{B}$ is the magnetic field. In a simple metal, m^* and τ are assumed to be isotropic and under steady-state conditions,

$d\mathbf{v}/dt = d^2\mathbf{r}/dt^2 = 0$, which leads to

$$\frac{m^*}{\tau}\mathbf{v}_d = q[\mathbf{E} + (\mathbf{v}_d \times \mathbf{B})] \ , \tag{5.2}$$

where $\mathbf{v}_d$ is the drift velocity. When a magnetic field is applied along the z-axis, multiplying each of the components by the carrier density n and charge q gives the current density $\mathbf{j}$=nq$\mathbf{v}_d$, which can be written in a matrix form as

$$\begin{pmatrix} j_x \\ j_y \\ j_z \end{pmatrix} = \frac{nq^2\tau}{m^*}\left[\begin{pmatrix} E_x \\ E_y \\ E_z \end{pmatrix} + \begin{pmatrix} v_{d,y} \\ -v_{d,x} \\ 0 \end{pmatrix} B_z\right] = \frac{nq^2\tau}{m^*}\begin{pmatrix} E_x \\ E_y \\ E_z \end{pmatrix} + \frac{q\tau}{m^*}\begin{pmatrix} j_y \\ -j_x \\ 0 \end{pmatrix} B_z \ . \tag{5.3}$$

To simplify this, the zero-field conductivity σ_0, and the the classical cyclotron frequency ω_c are defined as

$$\sigma_0 = \frac{nq^2\tau}{m^*} \ , \tag{5.4}$$

and

$$\omega_c = -\frac{qB_z}{m^*} \ , \tag{5.5}$$

respectively. Using these definitions, Eq. 5.3 can be simplified to

$$\begin{pmatrix} j_x \\ j_y \\ j_z \end{pmatrix} = \sigma_0\begin{pmatrix} E_x \\ E_y \\ E_z \end{pmatrix} + \omega_c\tau\begin{pmatrix} -j_y \\ j_x \\ 0 \end{pmatrix} \ . \tag{5.6}$$

Solving Eq. 5.6 gives the current density

$$\begin{pmatrix} j_x \\ j_y \\ j_z \end{pmatrix} = \frac{\sigma_0}{1+(\omega_c\tau)^2}\begin{pmatrix} 1 & -\omega_c\tau & 0 \\ \omega_c\tau & 1 & 0 \\ 0 & 0 & 1+(\omega_c\tau)^2 \end{pmatrix}\begin{pmatrix} E_x \\ E_y \\ E_z \end{pmatrix} \ . \tag{5.7}$$

Based on Eq. 5.7, a generalized magnetoconductivity tensor $\boldsymbol{\sigma}(B)$ can be difined as

$$\boldsymbol{\sigma} = \frac{\sigma_0}{1+(\omega_c\tau)^2}\begin{pmatrix} 1 & -\omega_c\tau & 0 \\ \omega_c\tau & 1 & 0 \\ 0 & 0 & 1+(\omega_c\tau)^2 \end{pmatrix} \ . \tag{5.8}$$

The off-diagonal elements are the cause of the Hall effect and the cyclotron radius r_c becomes

$$r_c = \frac{m^* c}{qB_z} \ . \tag{5.9}$$

Assuming a simple picture where a magnetic field causes the charges to drift in the y direction and create an electric field E_y, it follows that

$$E_y = -\frac{\omega_c \tau j_x}{\sigma_0} \ , \tag{5.10}$$

The current measured in the x direction is given by

$$j_x = \sigma_0 E_x \ , \tag{5.11}$$

and the Hall coefficient R_H is defined as

$$R_H = \frac{E_y}{j_x B_z} = -\frac{\omega_c \tau}{\sigma_0 B_z} = \frac{1}{nq} \ . \tag{5.12}$$

Additionally, since the conductivity tensor $\boldsymbol{\sigma}$ is also defined from

$$\mathbf{J} = \boldsymbol{\sigma} \cdot \mathbf{E} = \begin{pmatrix} \sigma_{xx} & \sigma_{xy} & 0 \\ \sigma_{yx} & \sigma_{yy} & 0 \\ 0 & 0 & \sigma_{zz} \end{pmatrix} \begin{pmatrix} E_x \\ E_y \\ E_z \end{pmatrix} \ , \tag{5.13}$$

the individual components are thus given by

$$\sigma_{xx} = \sigma_{yy} = \frac{\sigma_0}{1 + (\omega_c \tau)^2} \tag{5.14}$$

$$\sigma_{xy} = -\sigma_{yx} = -\frac{\sigma_0 \omega_c \tau}{1 + (\omega_c \tau)^2} \ . \tag{5.15}$$

The Lorentz force acting on the current-carrying electrons increases the chance of scattering and thus the resistance of a sample also increases. Calculated magnetoconductance $\sigma_{xx}/\sigma_0 = 1/(1 + (\omega_c \tau)^2)$ implies that the magnetoresistance, which is inverse of the magnetoconductance, is proportional to $(1 + (\mu \mathbf{B})^2)$ in a simple semiconductor with a single carrier type, where μ is the semiconductor mobility.

5.2 Hall effect measurement

Hall effect measurements are used in this work for measuring the mobile carrier density in the heterostructures and determine the carrier mobility [136]. The first task is to verify that the total carrier number does indeed scale with the number of La dopants in the heterostructure, but the mobility analysis is equally important. The heterostructures contain three layers: the $SrTiO_3$ substrate, the delta-doping layer, and the $SrTiO_3$ cap layer. All of these layers can, in principle, contribute to the conductivity of the heterostructure. The substrate is a high-quality single crystal and is known to support high electron mobility at low temperatures. The $LaTiO_3$ delta doping layer can only be distinguished as a separate phase for layer thicknesses of over 2 unit cells, but the mobility of carriers in $LaTiO_3$ films grown at low temperatures is known to be several orders of magnitude lower than in bulk $SrTiO_3$. The cap layer also consists of $SrTiO_3$, but it is also grown at low temperature, which means that the cap layer has a high density of point defects, which dramatically reduce the carrier mobility. Mobility numbers determined by Hall measurements can thus be used to infer which parts of the heterostructure are contributing to the conductivity.

Fig. 5.1 shows the schematic of the Hall measurement used in this study. Samples with $LaTiO_3$ thickness of 1, 2, and 5 unit cells were used for carrier density analysis. The $LaTiO_3$ layer thicknesses were estimated by counting RHEED oscillations and also checked against Dektak profilometer measurements of thicker films.

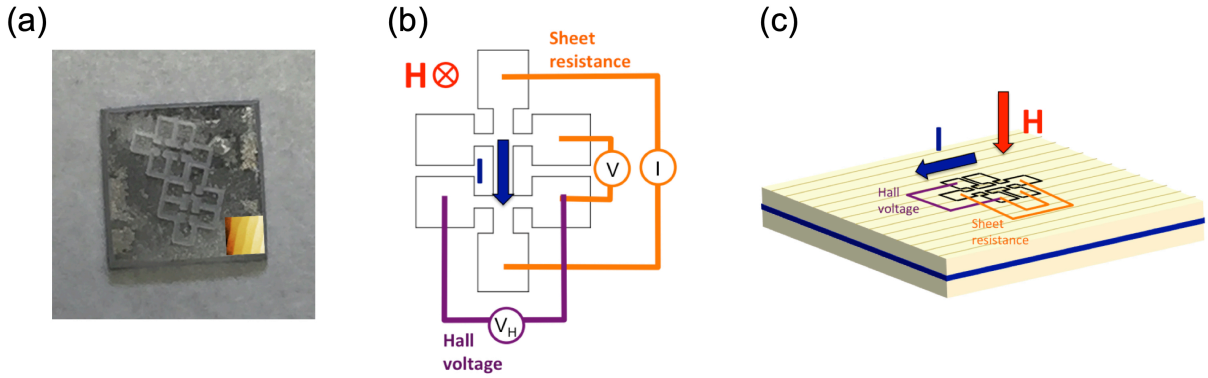

Figure 5.1: (a) A photograph of two Hall bars in a sample. The AFM image in the inset shows the step orientation of the substrate (b) Schematic figure of a Hall measurement. (c) Hall bar is aligned to the step direction.

The carrier accumulation layers that form in the delta-doped $SrTiO_3$ heterostructures

are not bounded on the substrate side, which means that a tail of carrier density can be expected in the $SrTiO_3$ substrate (Fig. 4.1). This effect can be significant in this case because the width of the accumulation gradient in a classical semiconductor picture is proportional to the square root of the dielectric permittivity of the semiconductor. For a $SrTiO_3$ single crystal, the room-temperature permittivity is 300, but increases to around 20000 at 10 K. Any space charge regions in $SrTiO_3$ can thus be much wider than in conventional semiconductors such as Si or GaAs which have permittivities of ~ 10. If a broad carrier accumulation tail does indeed form in a $SrTiO_3$ heterostructure, it may be possible to detect this phenomenon in Hall measurements because close to a single crystal surface, the carrier mobility is a function of depth. Scattering from charged surface defects always reduces the mobility of carriers close to surface or an interface, while carriers deeper inside a crystal experience no such additional scattering and can be expected to show enhanced mobility.

In addition to measuring carrier densities and mobilities, the purpose of the Hall experiments is thus to detect the presence of and to distinguish different types of carriers by measuring the Hall resistance and, in particular, examining the nonlinearity of the Hall resistance.

Three samples were used in the experiment, differing in the $LaTiO_3$ layer thickness, which was expected to determine the total carrier density in the doping layer. The Hall effect measurements were done in a PPMS system.

5.2.1 Two-carrier model

The analysis of Hall resistance is usually done by assuming that the current is carried by a single type of carriers, typically either electrons or holes in a semiconductor. There are, however, cases where several types of carriers may contribute to current flow. One such case is surface leak, where current flow in the bulk of a semiconductor and along the surface can be viewed as two parallel conduction paths. In such cases, both types of carrier may contribute to the Hall voltage and magnetoresistance [137]. It has been shown that, for example, in $Hg_{1-x}Cd_xTe$ [138], the parallel conduction paths lead to magnetic field dependent non-linear Hall resistance. This behavior can be analyzed by distinguishing between the different carrier populations, such as bulk and surface or interface carriers, by their different concentrations and mobilities [137]. For a simple two-layer structure with one layer having a thickness d_1 and conductivity σ_1 and a

second layer having a thickness d_2 and conductivity σ_2, the Hall resistance is given by

$$R_H = \frac{d[(R_{H1}{\sigma_1}^2 d_1 + (R_{H2}{\sigma_2}^2 d_2) + (R_{H1}{\sigma_1}^2 R_{H2}{\sigma_2}^2 (R_{H1}d_2 + (R_{H2}d_1)\mathbf{B}^2]}{(\sigma_1 d_1 + \sigma_2 n_2)^2 + \sigma_1^2\sigma_2^2(R_{H1}d_2 + R_{H2}d_1)^2 B^2} \quad , \tag{5.16}$$

which can be rewritten as

$$R_H = \frac{(\mu_1^2 n_1 + \mu_2^2 n_2) + (\mu_1\mu_2 B)^2(n_1 + n_2)}{e[(\mu_1|n_1| + \mu_2|n_2|)^2 + (\mu_1\mu_2 B)^2(n_1 + n_2)^2]} \quad , \tag{5.17}$$

where n_1 and n_2 are the sheet carrier densities in layers 1 and 2, and μ_1 and μ_2 are the respective mobilities. In the low magnetic field limit, the formula can be simplified to

$$R_{\mathrm{H}} \rightarrow \frac{({\mu_1}^2 n_1 + {\mu_2}^2 n_2)}{e\,(\mu_1|n_1| + \mu_2|n_2|)^2} \quad . \tag{5.18}$$

The results of Hall measurement for a heterostructure containing a single $LaTiO_3$ unit cell delta-doping layer is shown in Fig. 5.2 for various temperatures in the range of $2 \sim 50$ K. The Hall resistance (R_{xy}) plots are clearly nonlinear at low temperatures, and can be interpreted by assuming that the two carrier populations originate from distinct layers, as shown in Fig. 5.3.

The results of two-carrier fitting with Eq. 5.18 are shown in Table 5.1 for the three samples with different $LaTiO_3$ layer thicknesses, measured at 2 K. Increasing the $LaTiO_3$ layer thickness increases the carrier densities of both types of carriers and the increase of the total carrier density ($n_1 + n_2$) does indeed increase with the doping layer thickness, nearly saturating at 5 unit cells of $LaTiO_3$ (Fig. 5.4).

$LaTiO_3$ thickness	n_1 ($\times 10^{13}$cm^{-2})	μ_1 (cm^2 V^{-1} s^{-1})	n_2 ($\times 10^{13}$cm^{-2})	μ_2 (cm^2 V^{-1} s^{-1})
1 u.c.	2.46 ± 0.02	510± 10	0.80 ± 0.01	2400 ± 30
2 u.c.	2.58 ± 0.20	530± 50	1.78 ± 0.02	4500 ± 70
5 u.c.	2.77 ± 0.02	1300± 30	2.66 ± 0.03	11000 ± 30

Table 5.1: Carrier density and Hall mobility fitting results using the two carrier model for three $LaTiO_3$ thicknesses, measured at 2K.

The fitting of the nonlinear Hall resistance data converges well with small error estimates for the two-carrier model. The two carrier populations can be clearly distinguished by the large difference in mobility. It should be noted that as the nonlinearity of the Hall resistance disappears, the error estimates of the fit will increase rapidly or

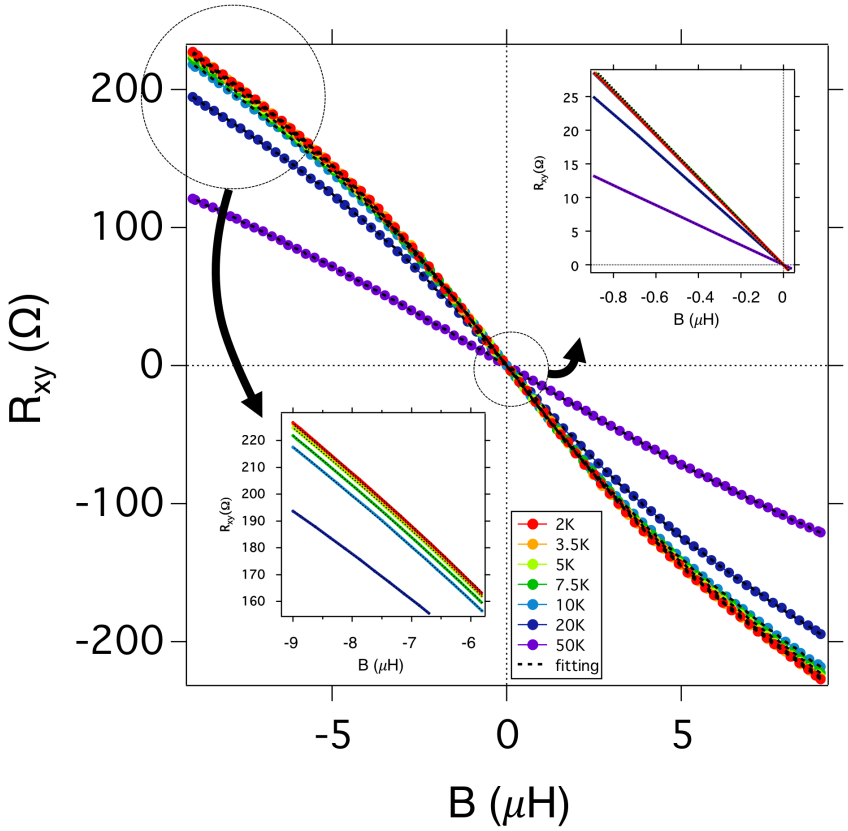

Figure 5.2: Hall resistance for a single unit cell $LaTiO_3$ delta doping layer embedded in $SrTiO_3$, measured at various temperatures.

the fitting fails to converge. No such problems were found in this fitting measured below 50 K.

The mobility numbers, especially for the heaviest doping, indicates that the mobility of about half the carriers is over 10^4 cm^2/Vs. Only the bulk $SrTiO_3$ substrate can support so high mobilities, which is why it is reasonable to assign the n_2,μ_2 carrier population to electrons distributed deep in the substrate, as illustrated in Fig. 5.3. The lower-mobility carriers are presumed to be located at the delta-doped interface. The interface layer that has been predicted to show orbital polarization due to the strong internal electric field is also the most disordered part of the heterostructure, therefore showing fairly low mobilities of less than 1,000 cm^2/Vs. As the La doping is increased by a factor of 5, the density of the low-mobility (interface) carriers changes only slightly, by no more than 10% (2.46→2.77×10^{13}cm^{-2}). The number of bulk-like high-mobility carriers, on the other hand, increases by more than 3 times (0.80→2.66×10^{13}cm^{-2}).

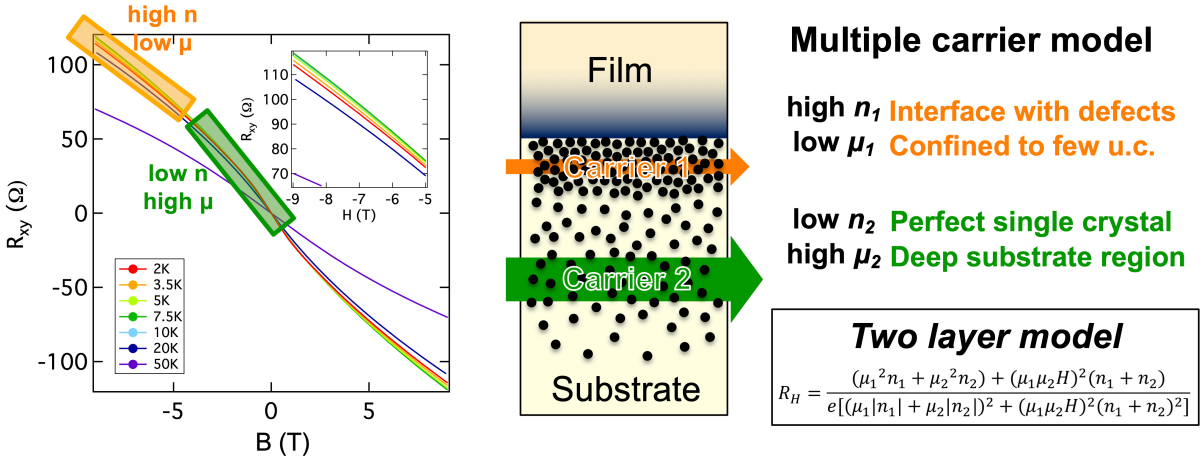

Figure 5.3: The depth profile of carriers used to interpret the results of the Hall resistance fitting by the two-carrier model. Interfacial carriers have high density and low mobility due to interface disorder, while deep carriers in the substrate have low density but much higher mobility.

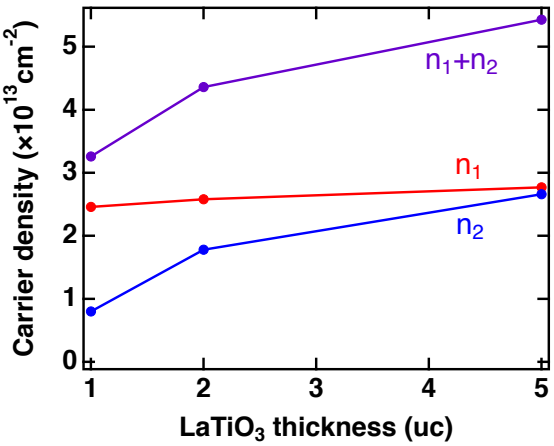

Figure 5.4: Carrier density as a function of $LaTiO_3$ thickness.

The potential profile near a symmetric $LaTiO_3$ delta-doping layer embedded in $SrTiO_3$ has been studied by Larson *et al.* by first principles calculations (Fig. 5.5) [100]. In this delta-doped quantum well, screening in $SrTiO_3$ due to the high permittivity at low temperature reduces the interface electric field and spreads the two-dimensional electron gas further away from the interface. Although electrons may spread to large distances of up to 100 nm from the interface, strong electric fields near the interface extend to about four or five unit cell layers into the $SrTiO_3$ bulk on either side of the interface. For a structurally relaxed structure, the orbital population of the first five Ti layers on either side of the interface is different from the deeper bulk-like $SrTiO_3$. Calculations show that due to the two-dimensional interface the energy of the d_{xy} orbitals is reduced compared to the other orbitals of the t_{2g} manifold. In the first few Ti layers, therefore, the electrons have mostly a d_{xy} character. An isotropic orbital population is reached at a depth of about 5 unit cells, as illustrated in Fig. 5.5. It is this selective orbital state at the interface that may support various forms of additional ordering, such as ferromagnetism or charge order.

The carrier density and mobility of the two carrier types in the heterostructure is illustrated by the depth profile in Fig. 5.6. Note that the potential shape is taken from the Poisson-Schrödinger calculations [132], and the depth scale will be discussed later. It is important to note here that the distribution is continuous and there is no sharp boundary between the two carrier populations as assumed in the two-carrier Hall fitting. This means that the carrier density and mobility numbers produced by a fit are effective population averages. Since the fitting is independent for each sample, the division of the two populations may also vary from fit to fit.

An interesting point here is that the carrier deisity measured from Hall analysis is 10 times smaller than the carriers expected by doping 1 unit cell of $LaTiO_3$ layer(6.6×10^{14} cm^{-2}). It appears that most of the carriers at the interface(~90%) remain in localized states below the mobility edge. A very similar situation exists in the $LaAlO_3$/$SrTiO_3$ heterostructures, where only about 1/10 of the expected carrier number is detectable in transport analysis. Since the mechanisms responsible for the conductivity are different in $LaAlO_3$ and $LaTiO_3$ interface, this similarity gives us a hint that the localization of carriers may be related to the surface defects of $SrTiO_3$ such as strain, intermixing, or oxygen vacancies. Additionally, the arguments for magnetic order generally make no assumption of localized electron states. The picture observed here could be similar to dilute magnetic semiconductors where the mobile carriers experience spin polarization due to interaction with magnetically-ordered scatterers. Although it is generally pos-

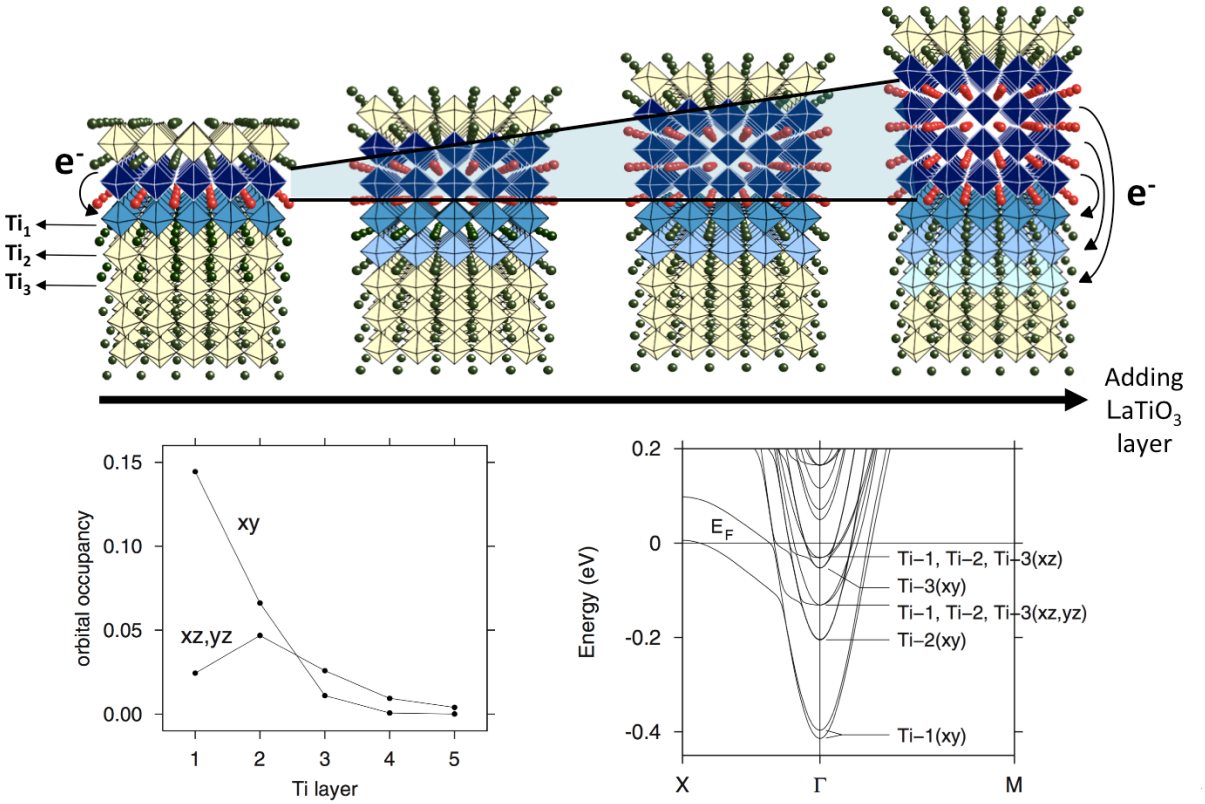

Figure 5.5: (Up) By changing the thickness of the $LaTiO_3$ doping layer, additional electrons are injected into the Ti d orbitals, spreading into $SrTiO_3$. (Bottom left) Individual occupancies of the Ti d orbitals near the interface, with the Ti layers numbered consecutively beginning at the interface. The occupancies of the xz and the yz orbitals are the same by symmetry, so that the total xz/yz occupancy is twice of the values shown in the plot. Mainly the d_{xy} orbitals, oriented parallel to the interface, are populated in the first Ti layer. (Bottom right) Conduction band states near the Γ point showing the interface sub-bands and their predominant orbital characters [100].

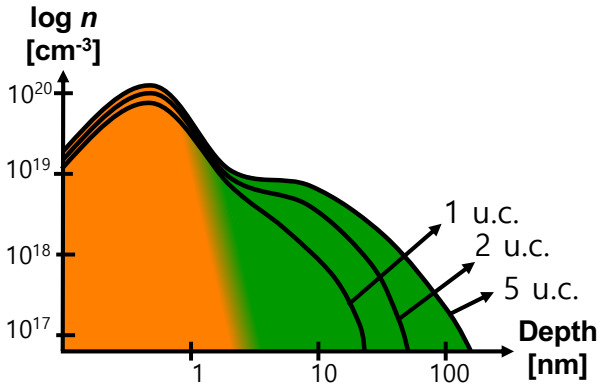

Figure 5.6: The schematic picture of carrier depth profile from two-layer Hall fitting measured at low temperature.

sible to detect a magnetic signature derived from the localized states from XMCD or PEEM-MCD, we need to investigate the magnetic order by aggregating the transport behavior by means of magnetotransport.

In conclusion of the Hall analysis, the carrier density of the interfacial carriers saturates as the lowest-energy Ti *d* orbitals are filled and excess carriers spill over deeper into the $SrTiO_3$ substrate. Since carrier scattering is much lower in the substrate than at the interface, the mobility of these carriers is correspondingly higher, reaching 11000 cm^2/Vs for the 5 unit cell $LaTiO_3$ layer sample.

The internal electric field confining the deep bulk-like carriers is much weaker and the carrier accumulation width may reach 100 nm, which will be discussed later. This means that although the Hall analysis shows that the sheet carrier densities for the two populations of carriers are similar, the effective carrier density per cm^3 is much lower. If the layer thickness ratio for the two carrier types is 1 nm vs 100 nm, the bulk-like carrier density for the 5 u.c. sample would average to 2.66×10^{18} cm^{-3}, which is just above the critical carrier density of about 10^{17} cm^{-3} for metallic conductivity in $SrTiO_3$. It is thus not surprising that these deep carriers exhibit bulk-like mobility at low temperature.

Finally, the Hall analysis shows that changing the thickness of the $LaTiO_3$ doping layer does not simply change the filling of a quantum well. Instead, adding carriers to the heterostructure leads to change of the depth distribution of carriers with different orbital characteristics.

5.2.2 Temperature and field dependences

The high-mobility carriers far from the interface, in a $SrTiO_3$ crystal substrate, would be expected to show temperature dependent transport properties that are similar to bulk $SrTiO_3$ [139]. $SrTiO_3$ is an incipient ferroelectric, and the dielectric constant diverges at low temperature from about 200 to 25 000. Due to the temperature dependent permimttivity, the width of the accumulation layer increase accordingly, since the thickness of the depletion layer (d_0) is proportional to the square root of the dielectric permittivity. Nearly 100 times increase in permittivity from room temperature to 4 K makes the conducting layer about 10 times deeper, which induces the increase of the carrier mobility. Also, the dielectric constant of $SrTiO_3$ is strongly dependent on the strength of the local electric field [40] induced by the transferred charges. At the interface region, the sharp increase of permittivity allows the width of the quantum well to be sharpened, supporting two-carrier model.

The nonlinear Hall behavior was generally seen at temperatures below 50 K, as shown in Fig. 5.2. Fig. 5.7 and Tables 5.2, 5.3, and 5.4 summarize the two-carrier fitting results for the 1, 2, and 5 u.c. $LaTiO_3$ thickness samples with varied temperatures. The temperature dependence of the high-mobility carriers (μ_2) does indeed show the expected bulk behavior with a sharp drop of mobility above 10 K. At the same time, the bulk dielectric permittivity of $SrTiO_3$ also drops, which means that the carrier accumulation layer becomes compressed and the orbital population at the interface equalizes within the t_{2g} manifold due to thermal excitations. Accordingly, the carrier density of the interfacial carriers (n_1) increases sharply above 10 K until the high-mobility carriers can no longer be detected above 50 K, at which point the system shows effectively a single carrier type.

Temperature	n_1 ($\times 10^{13}$cm^{-2})	μ_1 (cm^2 V^{-1} s^{-1})	n_2 ($\times 10^{13}$cm^{-2})	μ_2 (cm^2 V^{-1} s^{-1})
2 K	2.46 ± 0.02	510± 10	0.80 ± 0.01	2400
3.5 K	2.43 ± 0.02	530± 10	0.78 ± 0.01	2500
5 K	2.43 ± 0.01	540± 10	0.77 ± 0.01	2500
7.5 K	2.45 ± 0.01	560± 4	0.73 ± 0.004	2500
10 K	2.53 ± 0.004	560± 3	0.69 ± 0.003	2500
20 K	3.15 ± 0.004	440± 2	0.55 ± 0.002	2000
50 K	5.79 ± 0.02	180± 1	0.24 ± 0.004	870

Table 5.2: Fitting results of two-carrier model for the 1 u.c. $LaTiO_3$ thickness sample.

Temperature	n_1 ($\times 10^{13}$cm^{-2})	μ_1 (cm^2 V^{-1} s^{-1})	n_2 ($\times 10^{13}$cm^{-2})	μ_2 (cm^2 V^{-1} s^{-1})
2 K	2.58 ± 0.2	530± 50	1.78 ± 0.02	4500
3.5 K	2.47 ± 0.1	570± 50	1.76 ± 0.02	4500
5 K	2.40 ± 0.09	610± 40	1.74 ± 0.02	4400
7.5 K	2.34 ± 0.06	690± 40	1.66 ± 0.02	4200
20 K	3.50 ± 0.01	630± 10	1.11 ± 0.01	2900
50 K	8.20 ± 0.01	210± 1	0.39 ± 0.002	1270

Table 5.3: Fitting results of two-carrier model for the 2 u.c. $LaTiO_3$ thickness sample.

Temperature	n_1 ($\times 10^{13}$cm^{-2})	μ_1 (cm^2 V^{-1} s^{-1})	n_2 ($\times 10^{13}$cm^{-2})	μ_2 (cm^2 V^{-1} s^{-1})
2 K	2.77 ± 0.02	1300± 30	2.66 ± 0.03	11000
3.5 K	2.68 ± 0.02	1300± 30	2.67 ± 0.03	11000
5 K	2.60 ± 0.02	1300± 30	2.71 ± 0.03	10000
7.5 K	2.58 ± 0.02	120± 30	2.73 ± 0.02	9200
50 K	9.95 ± 0.02	270± 1	0.66 ± 0.005	1400

Table 5.4: Fitting results of two-carrier model for the 5 u.c. $LaTiO_3$ thickness sample.

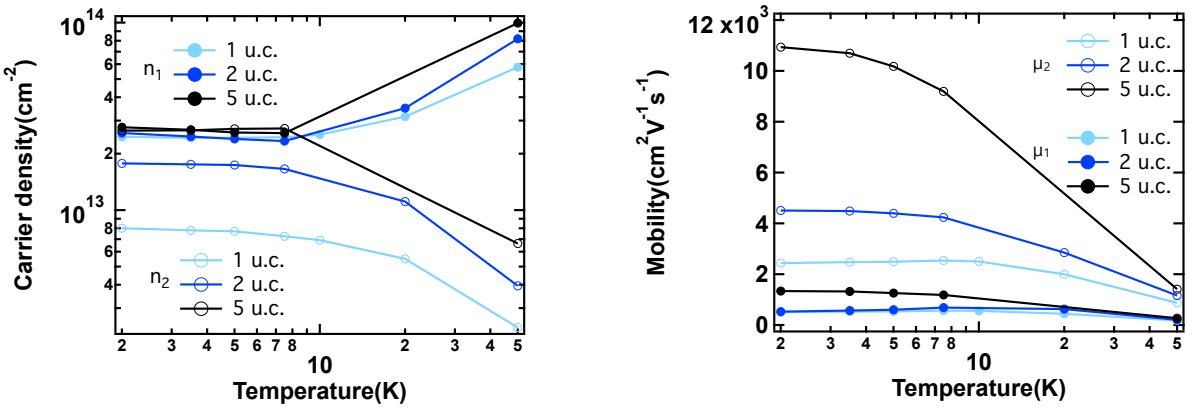

Figure 5.7: Summary of fitting results.

5.3 Out of plane magnetoresistance measurement

The magnetoresistance (MR) response was measured for different $LaTiO_3$ thickness samples while applying a magnetic field along the surface normal direction. Hall bars were cut on the sample surface by mechanical milling machine to prevent undesirable conductifity from the ion milling process. The step direction on each sample was checked by AFM and the Hall bars were oriented so that the current flow direction was parallel to the surface steps(Fig. 5.8). In the following discussion, the magnetoresistance is defined as

$$\frac{\Delta R(H)}{R(0)} = \frac{R(H) - R(0)}{R(0)} \times 100[\%] \tag{5.19}$$

for all samples.

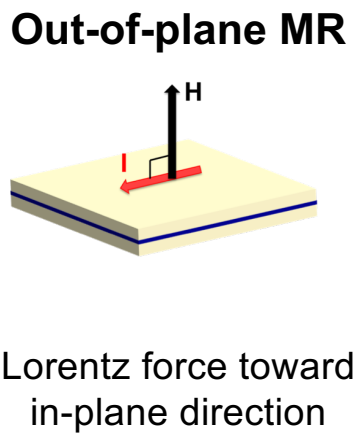

Figure 5.8: Detail of the magnetic field orientations used in this thesis.

As discussed in relation to Hall effect measurements, carriers with high electron mobility are expected to exist at the heterostructures. Out-of-plane MR measurement is a good method to probe the presence of those carriers, because high-mobility carreires are expected to make cyclotron motion loops in the plane, and therefore we can probe the mobility and the scattering mechanisms of those carriers independently from the measured Hall effect.

Fig. 5.9 shows the temperature dependence of the MR for three different samples where the $LaTiO_3$ thickness was either 1, 2, or 5 uc. Strong positive MR of up to 280% is seen in the thickest $LaTiO_3$ sample.

As was discussed in Section 5.1, in a simple model considering geometrical effect of MR with a single carrier type, the MR is proportional to $(1 + (\mu \mathbf{B})^2)$, where μ is

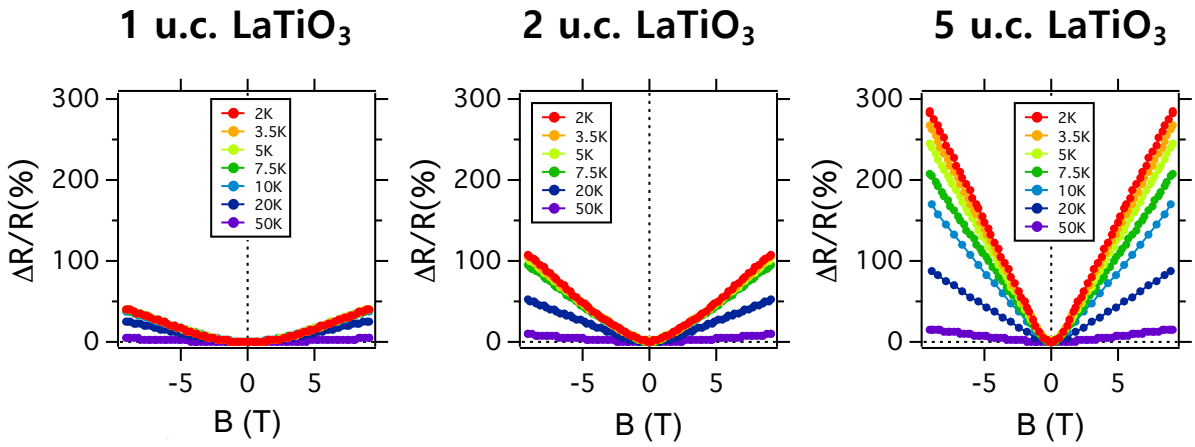

Figure 5.9: Temperature and step direction dependence of magnetoresistance when applying an out-of-plane magnetic field for different $LaTiO_3$ thicknesses samples. The magnetoresistance shows a parabolic shape at low magnetic fields and becomes linear with increasing magnetic field. The slope is steeper for thicker $LaTiO_3$ films.

the mobility ($m^2/V\cdot s$) and **B** is the magnetic field (Tesla). At low fields, quadratic MRdependence, which is usually expected for normal metallic samples, is observed within about one Tesla. This parabolic dependence are fitted and the mobility numbers are obtained, similar to the mobility numbers of the interface carriers.

In the high field region, the measured MR response is almost linear without any indication of saturation. Linear MR can occur when the electron distribution enters the so-called quantum limit, in which only the lowest Landau level is occupied, that is, when the cyclotron energy, $\hbar\omega_c$, exceeds the Fermi energy, E_F, and when $\hbar\omega_c$, $E_F \gg k_BT$ [140]. However, the transition of the MR to a linear B-dependence occurs at B_z ~1 T below the value satisfying the quantum limit condition $\hbar\omega_c = E_F$, that is, $B_z = \hbar(3\pi^2 n)^{2/3}/2e$. This limit corresponds to fields of over ~800T for the electron density measured from Hall effect, whcih cannot be the case in this system.

Monte-Carlo simulation [141] has reported that this type of non-saturating MR can originate from classical effects in highly scattering samples, where the distorted current paths arising from disorder-induced ihnomogeneities and macroscopic variations. Assuming the presence of low-mobility islands in a high-mobility conductor, the stochastic dynamics of the electron trajectory around low-mobility islands caused by multiple scattering at the islands and cause the classical linear MR (Fig. 5.10).

Also, similar behavior with mixed parabolic and linear MR has been reported to

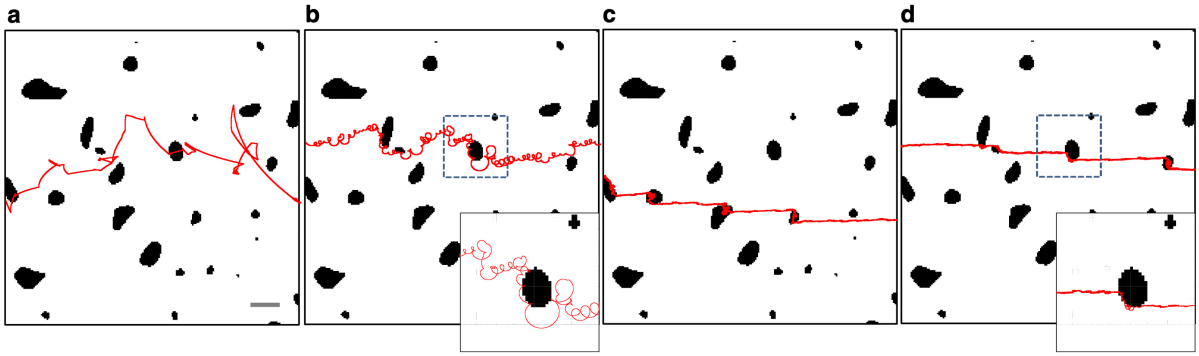

Figure 5.10: Calculated electron trajectories (red lines) in InAs for an applied electric field E_x = 0.5 kV cm^{-1} and under various applied magnetic fields B_z: (a) B_z = 0, (b) 1, (c) 10 and (d) 20 T. The black areas correspond to regions of low mobility. As shown in the magnified trajectories in the insets of panels (b) and (d), in the vicinity of a low-mobility island, the electron undergoes multiple scattering events, which act to deflect the cycloidal motion. The bar in panel (a) corresponds to 1 μm [141].

occur in few-layer graphene/BN interfaces. By assuming certain combination of n and μ, it is possible to reproduce the MR shape as shown in Fig. 5.11.

As the whole carrier density of the system increased, the slope of the linear MR seemed to increase accordingly, indicating the possibility of the change in carrier mobility. Unfortunately, the two-carrier model which was discussed in the previous section does not seem to be fit very well, which means that multiple components should taken into account to explain the linear MR.

In all samples, the magnetoresistance increases with decreasing temperature, possibly due to the increase of the high-mobility carriers.

To summarize out-of-plane MR, although we have the high-mobility carrier distributed deep into the $SrTiO_3$ substrate, it shows that the MR is still influenced by defects or other scattering processes.

5.4 In-plane magnetoresistance

When the magnetic field is applied in the plane of the heterostructure, the MR behavior may be affected by the geometry of the current and the magnetic field. Fig. 5.12 shows two in-plane orientations of the magnetic field and current used in this thesis. When the magnetic field is parallel to the current, no Lorentz force is expected. In this case,

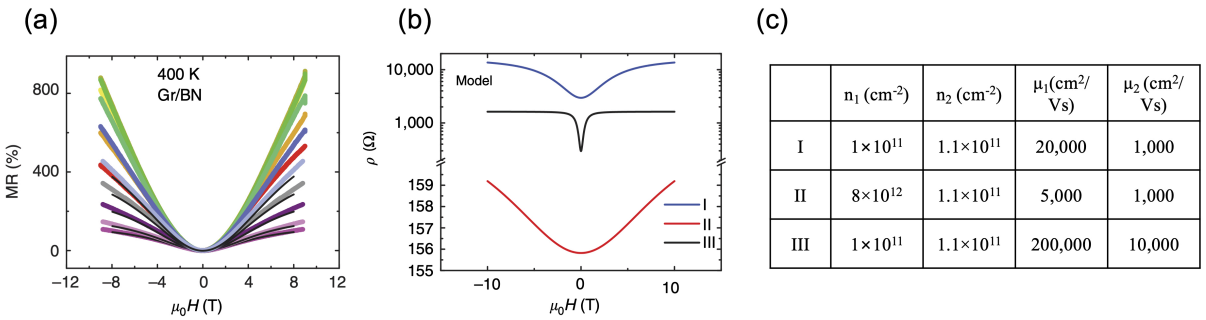

(c)

	n_1 (cm^{-2})	n_2 (cm^{-2})	μ_1(cm^2/Vs)	μ_2 (cm^2/Vs)
I	1×10^{11}	1.1×10^{11}	20,000	1,000
II	8×10^{12}	1.1×10^{11}	5,000	1,000
III	1×10^{11}	1.1×10^{11}	200,000	10,000

Figure 5.11: (a)The MR versus external magnetic field of four-layer graphene/BN. (b) Resistivity versus external magnetic field based on the theoretical prediction for a certain combination of carrier densities and mobilities in two effective channels(conditions are shown in (c)) [142].

MR may come from the interaction between magnetic field and the electron spin. On the other hand, if the magnetic field is applied in the plane of the heterostructure but perpendicular to the current flow direction, and the system is not truely-two-dimentional, a geometric MR component becomes non-zero, and the classical Lorentz force arises toward plane normal direction. As a consequence, a positive resistance can possibly be observed when the magnetic field is perpendicular to the current flow.

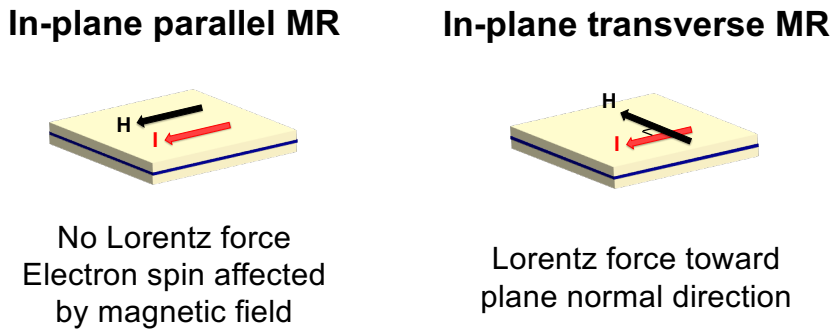

Figure 5.12: (Left) In-plane MR when H // I. (Right) In-plane MR when H ⊥ I.

Magnetic field applied parallel to the current flow

The high-mobility bulk-like carriers should not be subjected to a Lorentz force in this measurement configuration and would not be expected to give a significant contribu-

tion to the MR behavior. Measurements performed in H // I configuration for 5 u.c. $LaTiO_3$ sample are shown in Fig. 5.13. A strong negative magnetoresistance of up to 60% was observed below 50 K. The negative MR saturates at high fields and strongly depends on the temperature. A literature survey showed that multiple mechanisms are expected to influence the low-temperature in-plane negative MR behavior.

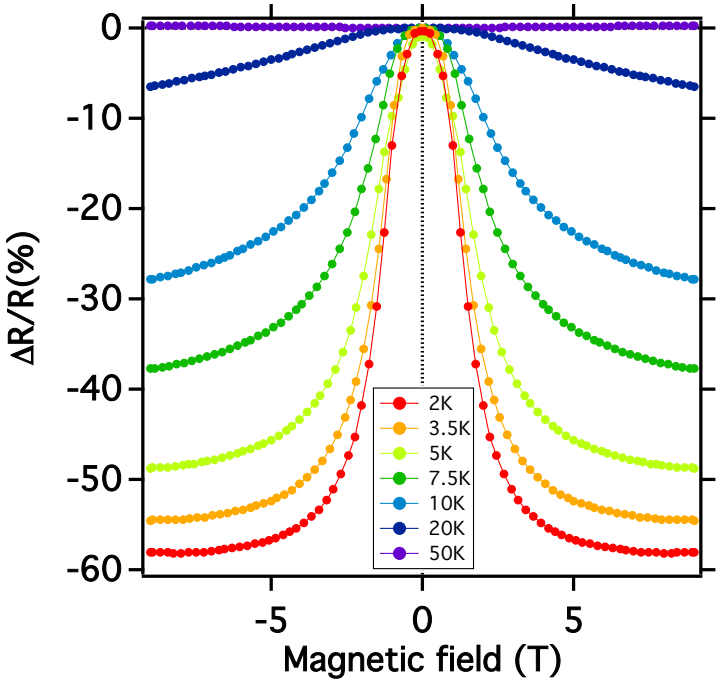

Figure 5.13: Magnetic field dependence of the in-plane magnetoresistance for the 5 u.c. $LaTiO_3$ sample at various temperatures.

The $LaTiO_3$ thickness dependence of the in-plane magnetoresistance measurements is summarized in Fig. 5.14. In thicker $LaTiO_3$ samples, the low temperature (5 K) negative component is dominant in the low magnetic field region. The low-field MR slope is strongly dependent to the $LaTiO_3$ thickness and the 1 u.c. $LaTiO_3$ film shows a wide flat region at low fields.

Since the quantum well forming at the $LaTiO_3/SrTiO_3$ interface is strongly asymmetric, the presence of significant Rashba-type spin-orbit coupling is possible. Diez *et al.* have studied the effect of spin-orbit coupling and scattering from finite-range impurities and have predicted that ~50% negative magnetoresistance may occur as shown in Fig. 5.15 [143]. The calculation gives a qualitatively similar behavior to what has observed in the experiment, both for the temperature dependence and for the

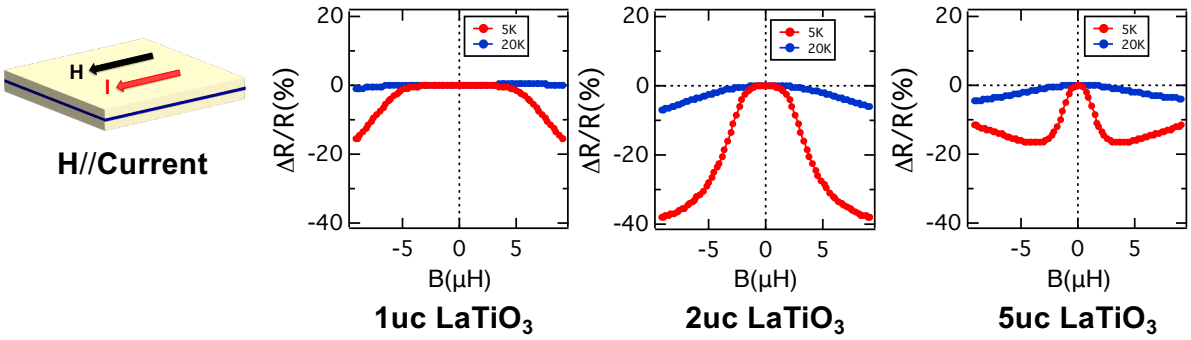

Figure 5.14: In-plane magnetoresistance for different $LaTiO_3$ thicknesses when magnetic field is parallel to the current flow.

carrier densities, considering that the Hall analysis gave a interface carrier density of $n_1 = 2.77 \times 10^{13}$ cm^{-2} for the 5 u.c. $LaTiO_3$ sample.

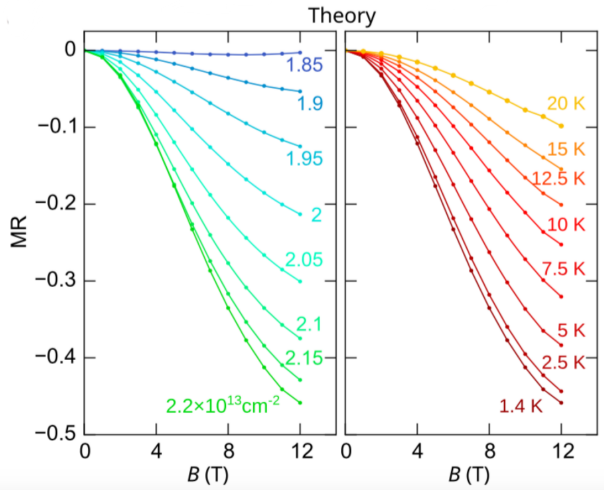

Figure 5.15: Magnetoresistance calculated from the Boltzmann equation at fixed T=1.4 K(left panel) and at fixed $n_1 = 2.2 \times 10^{13}$ cm^{-2} (right panel)[143].

So far, few experiments and calculations have reported the evolution of spin-orbit coupling when the Fermi level is driven to approach or depart from the Lifshitz point, i.e., the crossing point of the d_{xy} and $d_{yz,zx}$ orbitals. Fig. 5.16 show three different band structures by taking into account more terms of Hamiltonians. The carrier density at the Lifshitz transition point is reported about $1.4 \sim 1.7 \times 10^{13}$cm^{-2}[63, 144], which is smaller than the carrier density of the 1 u.c. $LaTiO_3$ sample. It is thus favorable to

construct lower doping samples as the further study for precise electronic structure analysis.

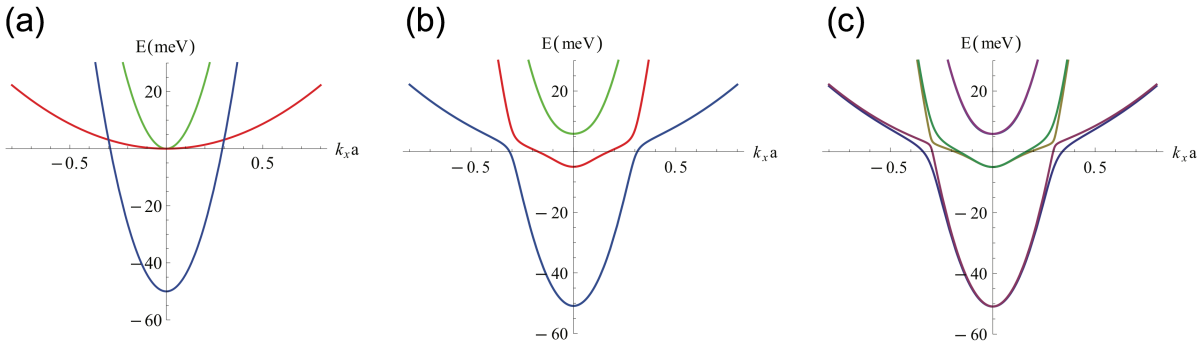

Figure 5.16: Band structure correponding to the different Hamiltonians (a) H_0, (b) $H_0 + H_{ASO}$, and (c) $H_0 + H_{ASO} + H_a$ where H_0: nearest-neighbor hopping and on- site interaction, H_{ASO}: atomic spin-orbit coupling, H_a: interorbital nearest-neighbor hopping [145].

Magnetic field applied perpendicular to the current flow

As shown in Fig. 5.17, when the magnetic field was applied in the in-plane transverse direction, a weak positive MR arose at high temperature, at above 20 K. This behavior can be attributed to the cyclotron motion of carriers in the out-of-plane direction, and can thus be used for determining the conducting layer thickness.

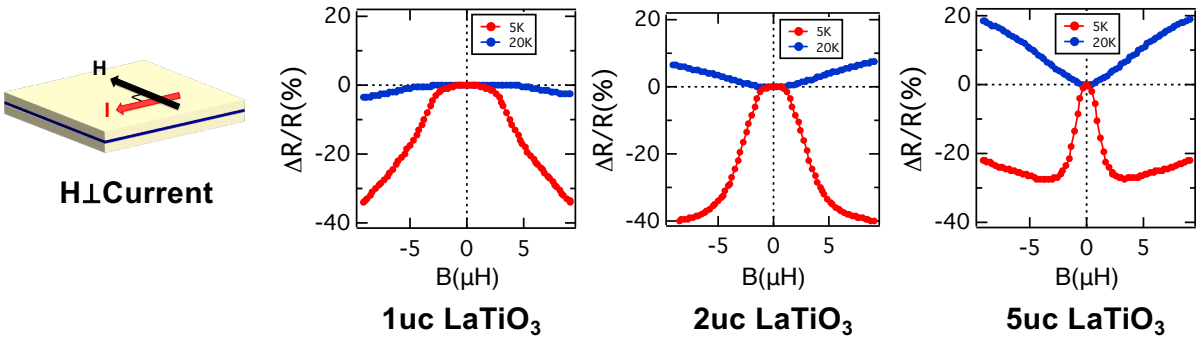

Figure 5.17: In-plane magnetoresistance for different $LaTiO_3$ thicknesses when the magnetic field was in the plane of the heterostructure and perpendicular to the current flow.

The cyclotron radius r_c is given by

$$r_c = \frac{m^* v_F}{eB} \quad , \tag{5.20}$$

where m^* is the electron effective mass [146], v_F is Fermi velocity, e is the elementary charge. With reasonable parameters for $SrTiO_3$, this equation gives a cyclotron radius estimate of about 90 nm under an applied magnetic field of 1 T. As shown in the magnified figures of the in-plane MR (Fig. 5.18), one important feature can be found especially for low-doping level sample, that is, the existence of a flat area in the low-field regime.

The schematic illustration of the way how to estimate the thickness of a conducting layer is shown in Fig. 5.19. For samples with low doping levels, where the metallic conducting layer is thin enough, the conducting layer becomes thinner than the cyclotron radius at low fields. In this case, the electrons cannot make a full cyclotron loop, and therefore the MR response is almost flat. As the magnetic field is increased, this cyclotron radius becomes smaller, and at some point it will become comparable to the conducting layer thickness. At that point, the MR signal will start to increase

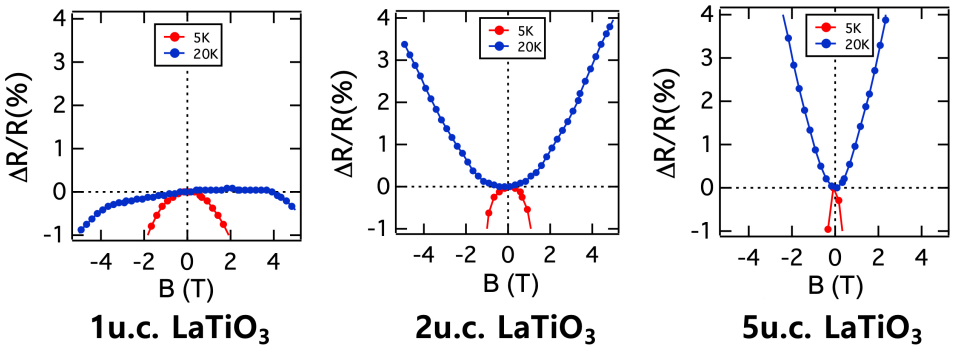

Figure 5.18: Magnified figures of the in-plane magnetoresistance.

with the field. For thicker films, the critical field value is close to zero and it becomes difficult to estimate the layer thickness. The estimated conducting layer thickness is about 15 nm for the 1 uc $LaTiO_3$ sample, and more than 100 nm for the 5 uc $LaTiO_3$ sample, supporting the conclusion from the Hall analysis that carriers are distributed over a large distance in the highly-doped heterostructures.

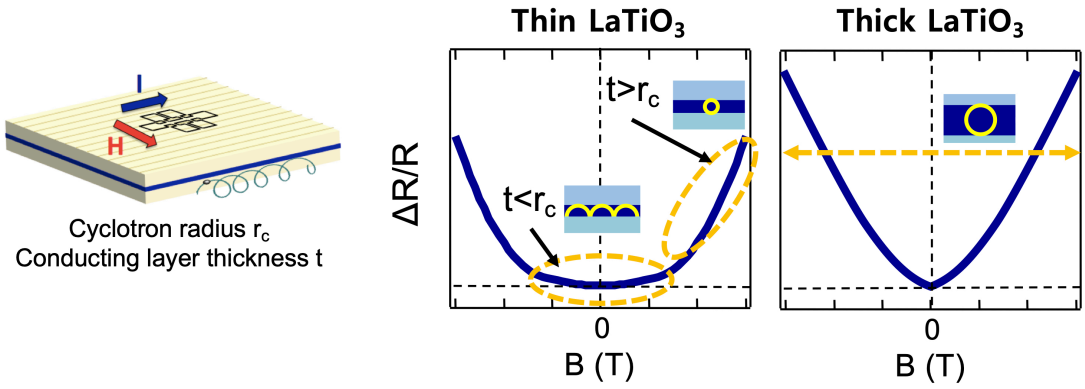

Figure 5.19: Schematic illustration of the way how to estimate the thickness of a conducting layer.

5.5 Summary

The Hall resistance and magnetoresistance were measured for heterostructures with different $LaTiO_3$ doping layer thicknesses embedded in $SrTiO_3$.

From Hall measurement, two types of carriers with different carrier densities and mobilities were found. The positive out-of-plane and strong negative in-plane magnetoresistance were observed ad assigned to the deep high-mobility and interface carriers, respectively.

From MR measurement, linear and positive MR is observed for out-of-plane measurement, indicating the scattering behavior of the high-mobility carrier distributed deep into the $SrTiO_3$ substrate. In-plane shows strong negative MR, possibly due to the spin-orbit interaction from broken inversion symmetry at the interface.

The $LaTiO_3$ layer thickness was shown to influence the total carrier number injected into the quantum well. A strong temperature and $LaTiO_3$ layer thickness dependence was found for both MR and Hall measurements.

Chapter 6

Back gate bias effect

6.1 Introduction

As was shown by the Hall and magnetotransport analysis, the transport characteristics of the heterostructures depend on the total number of carriers injected into the interface quantum well. Structurally, the carrier number can be changed by increasing or decreasing the thickness of the $LaTiO_3$ layer in a range of 0.3 to 5 u.c. Another option for continuously tuning the carrier density without affecting the structure of the quantum well is to use electrostatic gating.

There are several possible device geometries for applying an electrostatic field on a thin film interface. The most common types are known as back-gating and top-gating. However, considering the high sheet carrier density of the $LaTiO_3$ / $SrTiO_3$ interface, it is nearly impossible to apply a sufficiently high top-gate bias to significantly modulate the carrier density. In practice, common gate insulator oxides can reach a sheet carrier modulation of around 10^{12} cm^{-2}, which is only about 10% of the sheet carrier density of the $LaTiO_3$ quantum wells.

Another option is to use a back gate, which is made easier in $SrTiO_3$ devices due to the large low-temperature permittivity of $SrTiO_3$, which reaches 20,000 below 10 K. Since the substrate is 0.5 mm thick and an excellent insulator, gate bias values of several hundred Volts can be used. The role of a back gate is fundamentally different, however, from a top gate in that the field applied by a back gate has little effect on the carrier density near the interface. The back gate bias mostly affects the shape of the quantum well, changing the sharpness of the confinement potential at the interface and affecting the spread of carriers into deeper layers of the substrate. In terms of the two-carrier model discussed earlier, the back gate field should affect the ratio between the interface

and bulk-like carriers in the heterostructures.

Samples with 1, 2, and 5 u.c. $LaTiO_3$ layer were used for back-gating measurements. A copper sheet was attached onto the 44-pin ceramic packages as the back-gate electrode and the heterostructure samples were mounted on the copper sheet with silver paste (Fig. 6.1). After making contact with the heterostructure by Al wire bonding, the ceramic package was inserted into a low-temperature dipping probe and slowly dipped into a liquid helium vessel, cooling the sample down to 4.2 K.

A schematic illustration of a back-gated heterostructure is shown in Fig. 6.2. The gate bias is applied relative to the metallic interface, which is held close to ground potential. The gate bias modifies the electron confinement profile and thus modulates the transport properties. A positive gate bias ($V_G > 0$) is expected to broaden the quantum well, while a negative bias ($V_G < 0$) can narrow the quantum well. A broadened quantum well under a positive back-gate bias allows the carriers to travel deeper in a clean single crystal and the sample resistance may thus decrease due to the larger number carriers in the high-mobility region of the heterostructure. In the opposite way, a sharper quantum well is expected to increase the sample resistance.

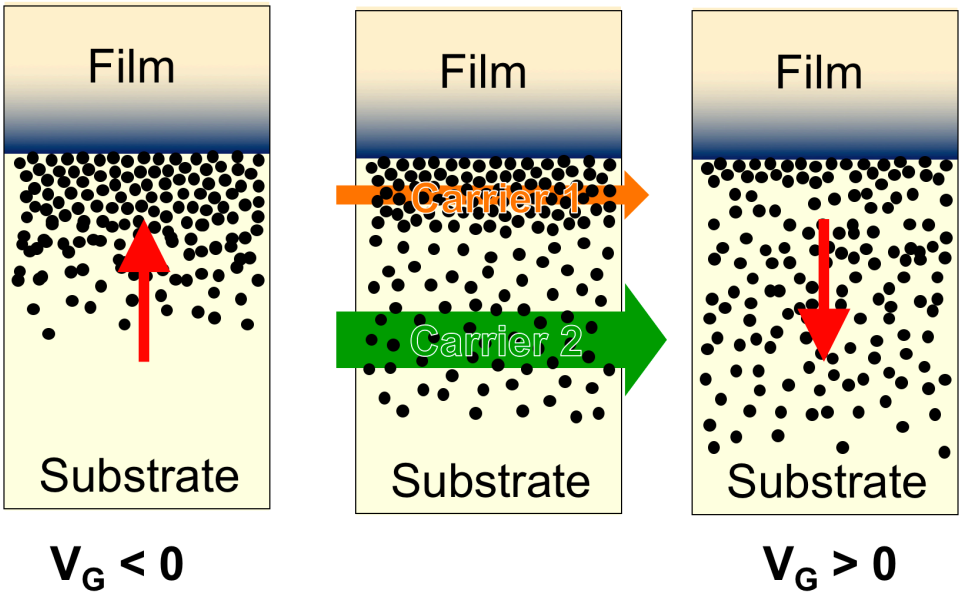

Figure 6.1: Schematic diagram of a back-gated $LaTiO_3/SrTiO_3$ heterostructure for positive, zero, and negative gate bias polarities.

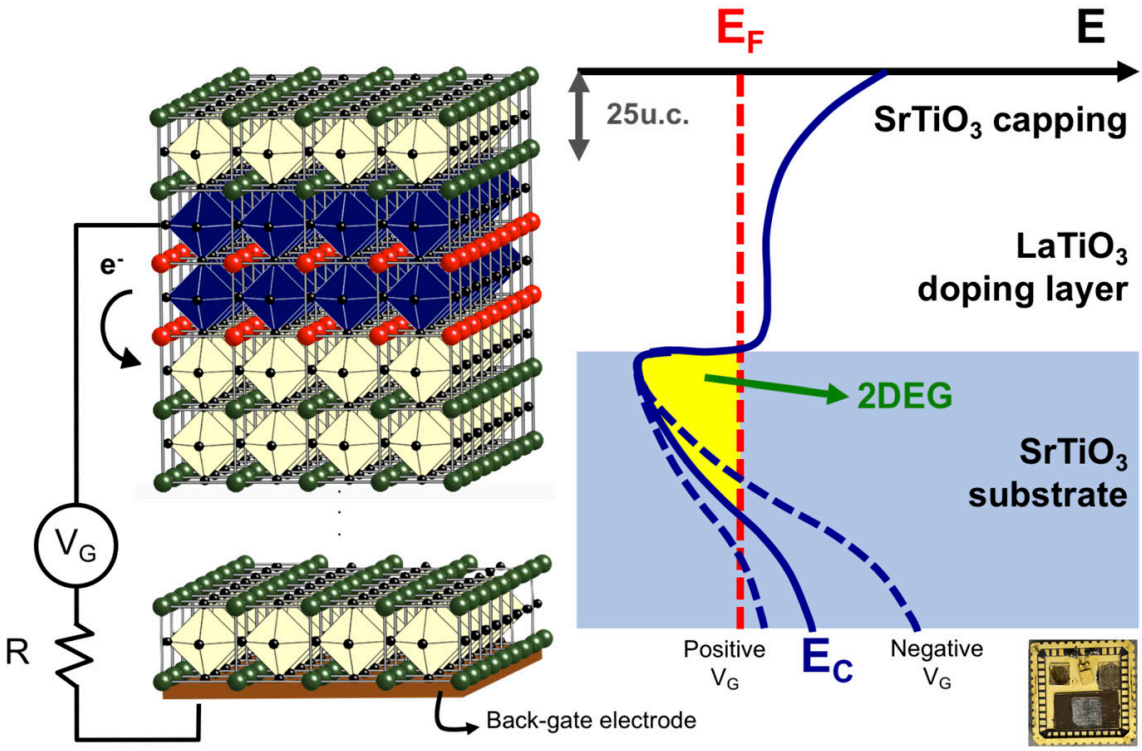

Figure 6.2: Schematic diagram of a back-gated $LaTiO_3$ / $SrTiO_3$ heterostructure for different gate bias polarities. A sample photograph is also shown.

6.2 Memory effect of the sample resistance

As was shown in Fig. 6.1, applying a backside gate field does not simply deplete or accumulate carriers at the interface, but is expected to alter the depth distribution of carriers in the heterostructure. Interestingly, the back gating experiments offer a way to probe such depth distribution change through the observation of non-reversible gate bias cycles, i.e., the memory effect of the sample resistance.

Fig. 6.3 shows the irreversible resistance change upon positive back-gate biasing. While the negative back gate bias can be reversibly applied, once a strong positive bias is applied, the heterostructure resistance increases irreversibly and a hysteresis effect appears, implying that the maximum doping level of this interface is limited at low temperature.

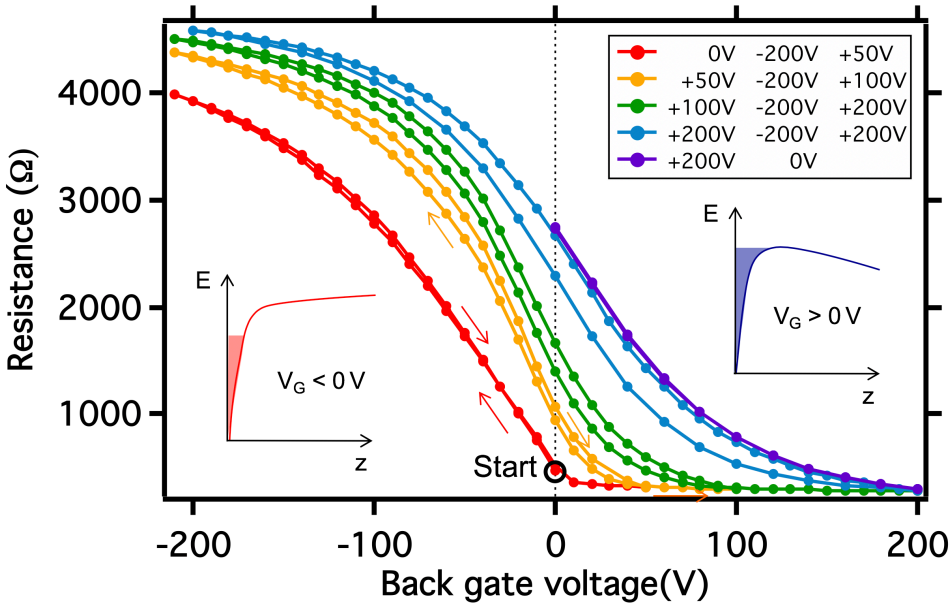

Figure 6.3: Irreversible resistance change that occurs upon positive back-gate biasing. The bias scan directions are shown in the inset. For each loop, the maximum positive bias was increased to +50, +10, and +200 V

Fig. 6.4 shows the results of a time-dependent gating experiment for 5 unit cell $LaTiO_3$ sample. The sample was cooled to 4.2 K at zero gate bias. The gating experiment starting point is thus the same as for the other Hall effect measurement samples. The

gate bias was then applied to approximately 100-second intervals.

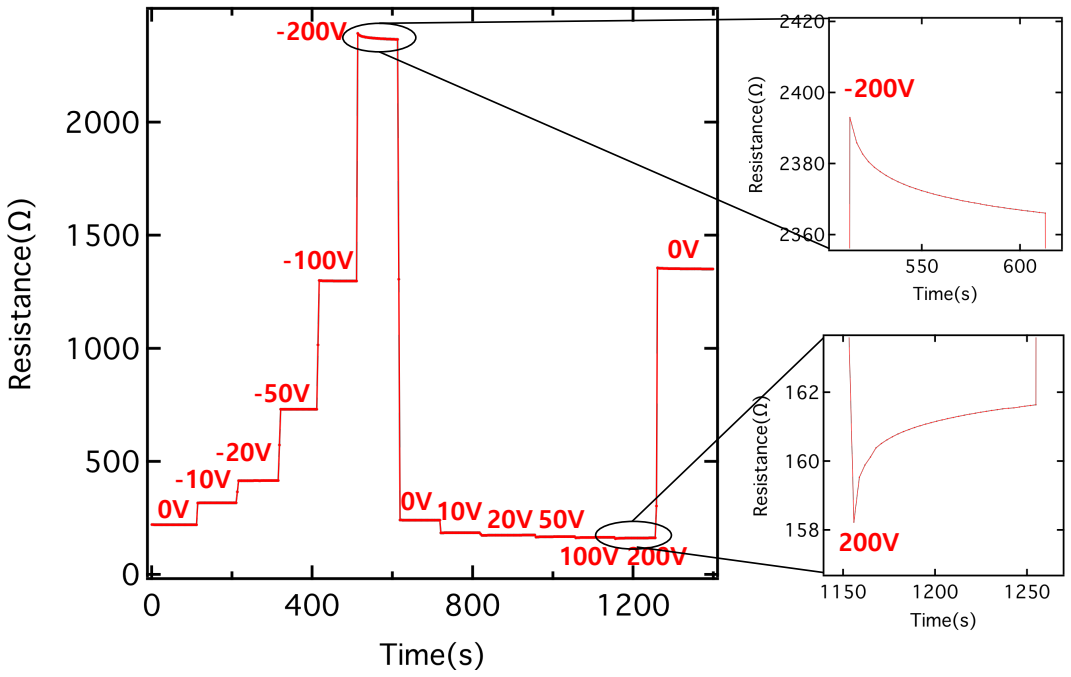

Figure 6.4: The resistance of a 5 u.c. $LaTiO_3$ / $SrTiO_3$ quantum well as a function of applied back-gate voltage at 4.2 K. Magnified figures show the logarithmical resistance relaxation after the change of applied back-gate bias.

At first, a negative gate bias loop was measured. The gate bias values were V_G=-10, -20, -50, -100, and -200 V. The sample resistance increased nearly proportionally to the bias voltage, which would correspond to the reduction of the number of high-mobility carriers in the heterostructure. When the bias voltage was returned to 0 V, the interface layer resistance returned to the original value. Similar biasing loops could be repeated several times without affecting the zero-bias resistance of the channel.

However, the behavior was quite different when a positive bias was applied. When the gate bias V_G increased to +10, +20, +50, +100, and +200 V (applied for 100 s each), the resistance decreased only slightly, which can be interpreted as a widening of the confining potential well at the interface. It appears that during positive biasing the confining potential quickly reaches the Fermi level and the resistance change saturates, as shown in Fig. 6.5.

When the gate bias returns to zero from +200 V, the heterostructure resistance increases sharply and remains higher than the initial value before the start of the

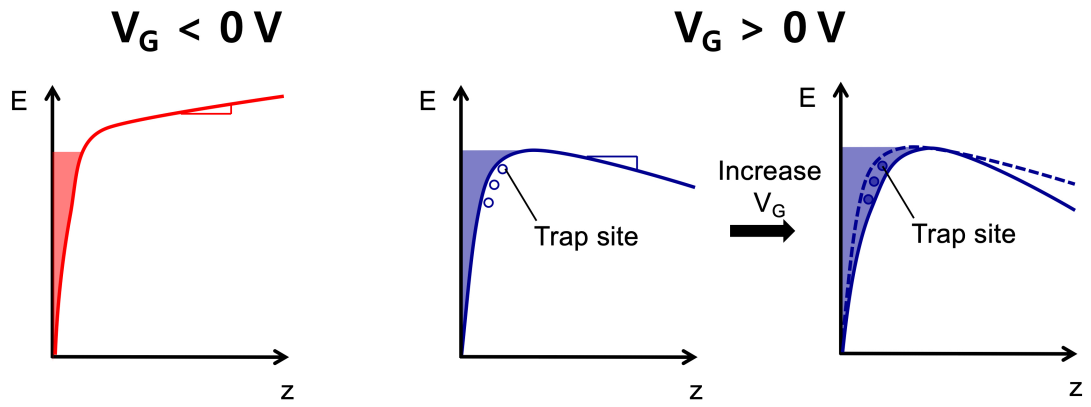

Figure 6.5: Schematic illustration of filling the quantum well for different V_G values. z denotes the distance from the interface.

positive bias loop. Just after applying a positive (negative) bias voltage, the resistance values are increased (decreased) slightly and quickly reach a steady state. The time dependence of the response after a bias step follows a logarithmic time dependence of 2-dimensional Drude resistivity when the electrons are escaping from the well [147]:

$$R(t) = \frac{1}{e\mu n(t)} \approx R_{0+}\left[1 + \frac{N_F k_B T}{n_{0+}} ln\left(1 + \frac{t}{t_E}\right)\right], \tag{6.1}$$

where k is the kinetic factor following the Arrhenius law, N_F is the total density of states at the Fermi energy, and t_E is the escape time. n_{0+} and $R_{0+} = (e\mu n_{0+})^{-1}$ denotes the carrier density and resistivity at $t = 0$, respectively. The gating memory effect can thus be understood in terms of bulk carrier trapping in the $SrTiO_3$ substrate. When a metallic state is induced in an oxide like $SrTiO_3$ by doping, the Fermi level shifts into the conduction band and any defect states with energies below the conduction band minimum would be filled or inactive from the point of view of transport behavior. It is thus possible to observe carrier mobilities of 10,000 cm^2/Vs in electron-doped $SrTiO_3$ at cryogenic temperatures.

The situation is very different when carriers are introduced into $SrTiO_3$ by other means, such as charge transfer, as happens in the $LaTiO_3/SrTiO_3$ heterostructures. In this case, the Fermi level position in the deeper part of the substrate corresponds to the bulk value, which is usually found to be a few hundred meV below the conduction band minimum. It is thus entirely possible, that unoccupied in-gap or band edge states remain in the substrate. When a positive back-gate bias is applied to the heterostructures, the carrier distribution becomes broader, stretching further into the substrate, as

shown in Fig. 6.1 for $V_G > 0$. Since empty trap states exist in this part of the substrate, some of the carriers pushed into the deeper layers will be trapped and remain in the trap states when the gate bias is removed. The gating experiments show that the resistance may increase by as much as a factor of 10, which suggests that a very large proportion of the high-mobility carriers in the heterostructures are effectively localized in spatially deep but energetically shallow trap states in the $SrTiO_3$ substrate.

Fig. 6.6 shows the doping layer thickness dependence of the memory effect. Depletion behavior at negative bias is similar, regardless of the total carrier number but for the carrier accumulation region ($V_G > 0$), the point where the resistance change saturates is shallower for the samples with higher doping levels. For the 5 unit cell $LaTiO_3$ sample, the resistivity saturation occurs at 20 V, while nearly twice that is required for the 1 unit cell $LaTiO_3$ heterostructure, possibly due to a difference of the Fermi level height.

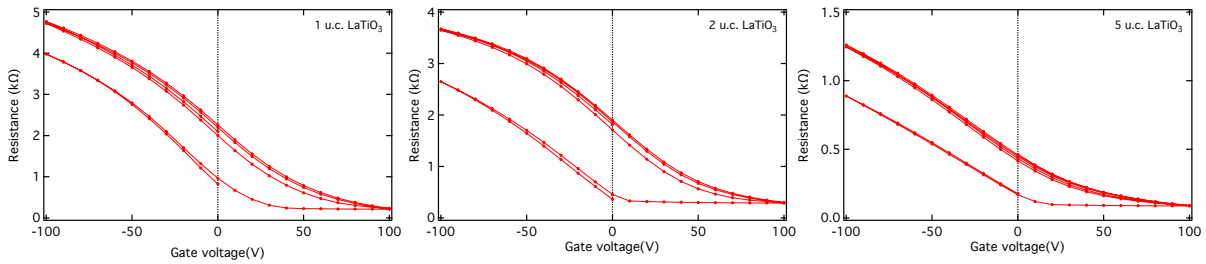

Figure 6.6: Irreversible resistance change that occurs upon positive back-gate biasing for 1, 2, and 5u.c. $LaTiO_3$ sample measured at 4.2 K.

It seems that the carrier trapping occurs at the conduction band edge, but the precise nature of the trap states is not known. This behavior appears to be related to the formation of Sr vacancies or oxygen vacancy [148] clusters in the surface layer of the substrate [134, 133] that cannot be eliminated by a simple post-annealing treatment in air [149](Fig. 6.9). Defects such as oxygen vacancies(V_O), Sr vacancies(V_{Sr}), V_O clusters can affect dramatic effect on mobility[150]. The substrate defects may be the main cause for the large variation of reported carrier densities for $LaAlO_3/SrTiO_3$ heterostructures [149] and even the dimensionality of the confined carriers [151].

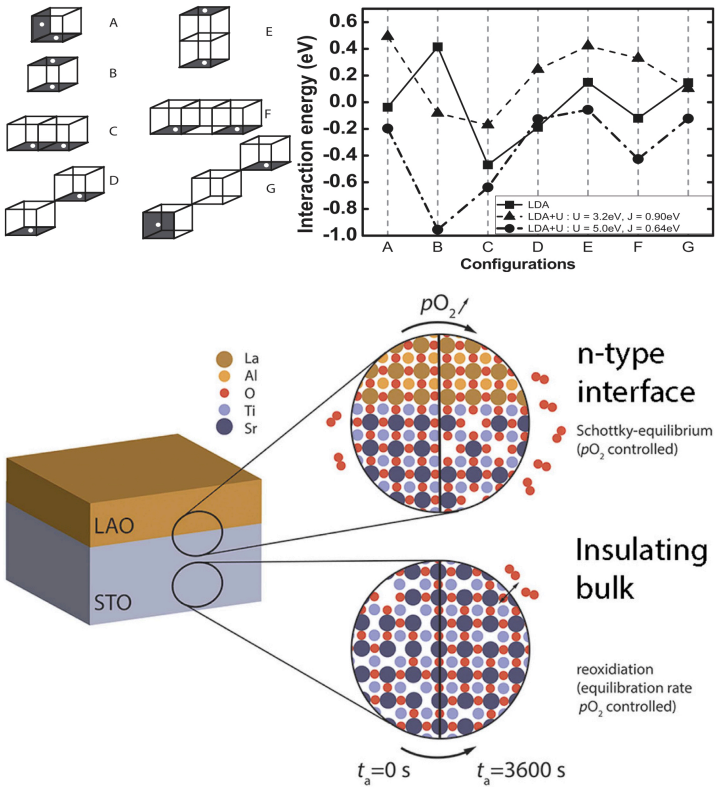

Figure 6.7: (Upper) Schematic configuration of two oxygen vacancies(blank circle) in the unit cell cube of $SrTiO_3$ and corresponding calculated interaction energy [148]. (Lower) Two distinct thermodynamic processes in $LaAlO_3/SrTiO_3$ heterostructures via annealing time(t_a). 1)Reoxidation of the STO substrate after reduction during the PLD process; 2) incorporation of strontium vacancies in the near-surface region upon high-pressure annealing [149].

6.3 Detrapping carriers

Once carriers are trapped in the substrate, it is impossible to detrap them by applying a negative gate bias. As shown by the temperature-dependent resistance data in Fig. 6.8, the original resistance of the device can be recovered by warming the sample to room temperature. The trapped carriers are released throughout the whole heating process. One prominent detrapping behavior is shown at around 80 K, which corresponds to the trapping energy of $k_BT \approx 7$ meV, and much shallower than the energy state of oxygen vacancies.

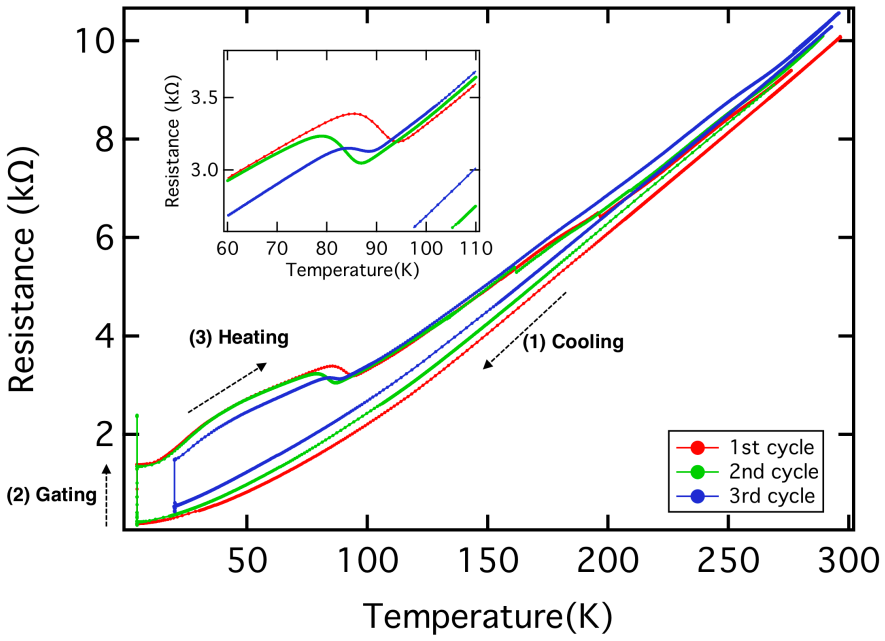

Figure 6.8: Resistance vs temperature change during cooling (before gating) and warming (after positive bias gating). The inset shows a magnified plot of the resistance in the vicinity of 80 K.

Another method to detrap carriers is optical excitation. To investigate whether the carrier can be detrapped by light, transport measurements were done under light illumination in an optical cryostat where the sample could be illuminated with light between 300 ~ 1100 nm, obtained from a monochromator. In this vacuum chamber, the sample temperature could be reduced to 10 K.

Before measurement, a positive bias of 100 V was applied for more than 200 seconds to trap carriers in the substrate. Fig. 6.9(upper panel) shows the effect of illuminating

the sample with 500 nm light, corresponding to a photon energy of 2.48 eV. Before illuminating the sample, the resistance showed a very slow logarithmic relaxation. A sharp exponential resistance drop occurred upon 500 nm light exposure, which implies that a simple optical detrapping occurred. The 2.48 eV photon energy is significantly lower than the $SrTiO_3$ band gap of 3.2 eV, which means that this illumination did not create carriers by band-to-band excitation. It could only detrap carriers trapped due to the gating.

After the initial 500 nm light illumination, carriers were repeatedly trapped by +100 V gate pulses and the detrapping was observed for several wavelengths. The photon energies were 300 nm (4.13 eV), 500 nm (2.48 eV), 700 nm (1.77 eV), 900 nm (1.38 eV), and 1100 nm (1.13 eV). Exponential decay was observed in all cases, as shown in Fig. 6.9(lower panel). Only the 300 nm light could generate more carriers by band gap excitation since the band gap of $SrTiO_3$ is 3.2 eV. There was no significant difference between the response to light with different wavelengths, which implies that the carrier trapping occurred close to the surface of the sample, i.e., at the $LaTiO_3$ interface and not at the back electrode interface. However, additional experimental work would be required to determine if the trapping and light-induced trap release affects only the deep carriers or also affects the interfacial carriers, i.e., the magnetotransport behavior. However, the magnetotransport measurements under light illumination cannot be performed in a standard PPMS instrument, which has no optical access port.

6.4 In-plane magnetoresistance with back-gating

It was found that by applying a back-gate bias, the in-plane magnetoresistance (MR) measured in the $I \parallel B$ configuration changed dramatically. The enhancement of the negative MR contribution under a positive back gate bias is shown in Fig. 6.10. It is obvious that saturating negative MR occurs at lower magnetic fields at high gate bias. The plots appear to have two components, a dominating negative MR and a weaker positive MR, as hinted by slight upturns for the 75 V and 100 V scans close to 10 T. Unfortunately, the field limit did not allow closer analysis of this behavior.

The carrier distribution change model inferred from the Hall analysis concluded that carriers are redistributed deeper into the substrate by the positive gate voltage. The effect of positive gate bias is thus essentially similar to adding more layers of $LaTiO_3$ to increase the total carrier number, which also leads to the growth of the deep carrier population. Indeed, the MR behavior is qualitatively similar, as can be seen with a

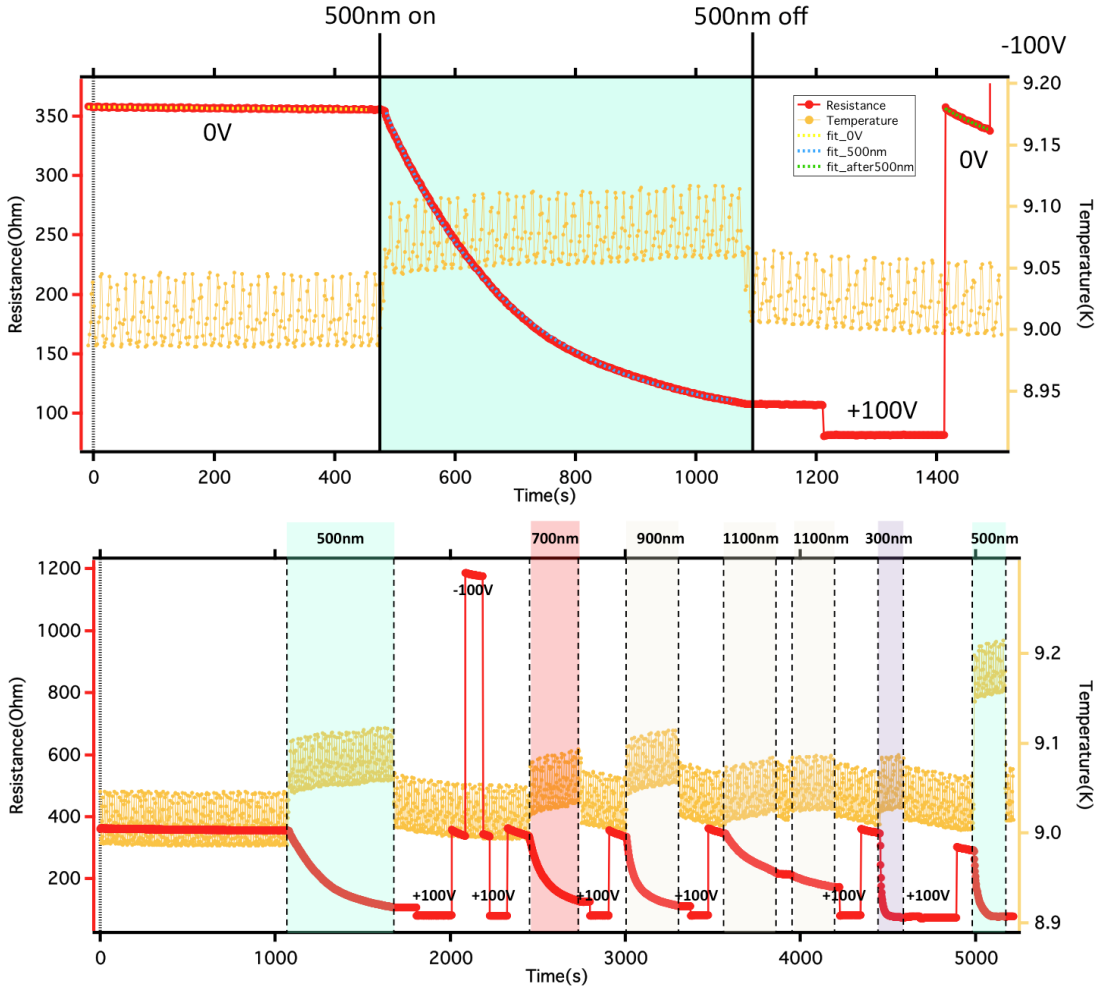

Figure 6.9: (Upper) Resistance vs time during a gating and light exposure experiment. The sample had been gated at +100V prior to light exposure. 500 nm light rapidly de-trapped carriers. (Lower) Resistance vs time during repeated gating and light exposure experiments.

comparison of the measurements in Fig. 5.14

The negative MR behavior has a similar gating memory effect as was seen for zero-field transport analysis. After trapping carriers by applying a positive gate bias, the negative MR component nearly disappeared, but could be recovered by re-applying the gate bias. The gating effect on negative in-plane MR shows that the depth distribution and the total number of carriers are important parameters for interfacial spin-orbit coupling, supporting the models predicting an increased spin-orbit coupling strength in the vicinity of the level-crossing Lifshitz point.

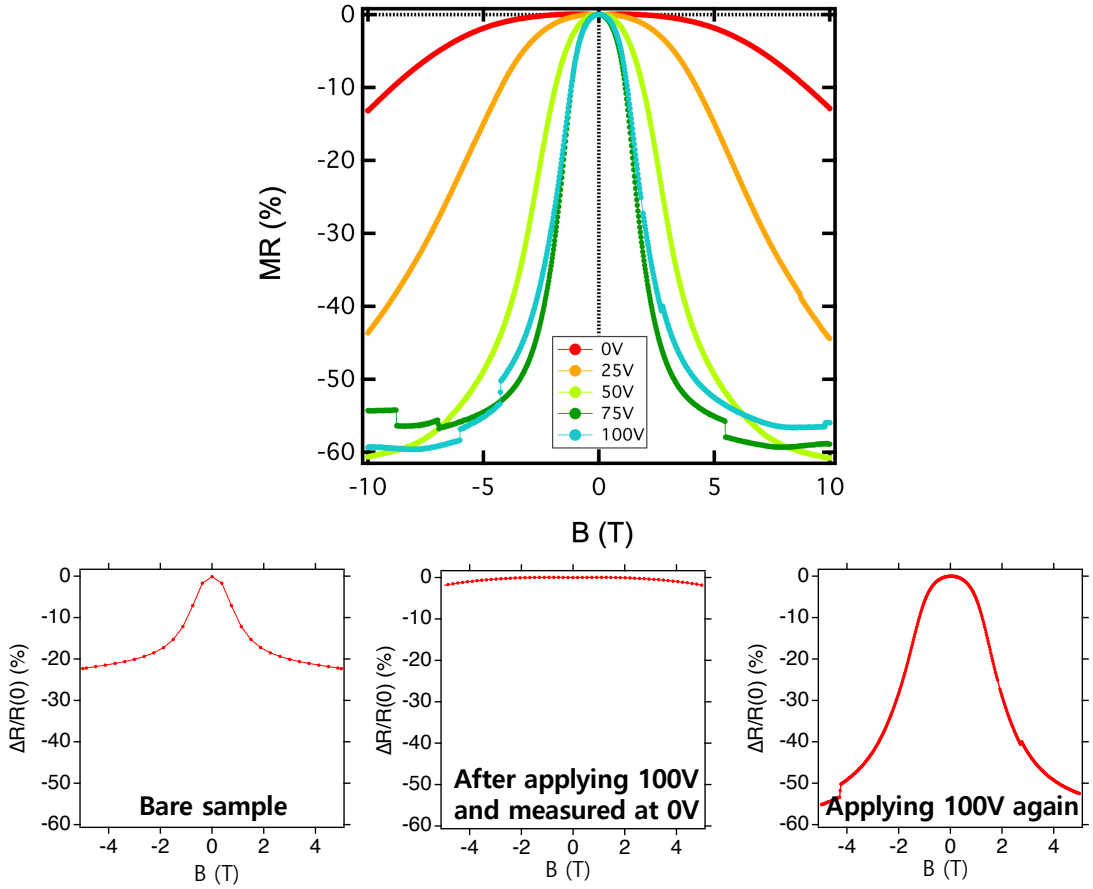

Figure 6.10: (Upper) In-plane negative magnetoresistance change upon the application pf a positive back-gate bias. (Lower) In-plane negative magnetoresistance change before/after applying a 100 V back-gate bias.

6.5 Summary

The electric field effect was used to tune the carrier confinement potential profile of the heterostructures. By applying a negative bias voltage, the quantum well can be compressed and the sample resistance grew rapidly. A positive gate bias appears to broaden the quantum well, which induced the spilling of carriers out of the interfacial quantum well and trapping of those spilled carriers deeper in the substrate, leading to only a slight decrease of resistance. Electrons that escaped from the quantum well could not be recovered by negative biasing and a strong irreversible resistance change was observed.

The memory effect could be reset by warming a sample to room temperature or by illuminating a sample with light. Due to the shallow trap energy, as estimated from the temperature dependence of resistance recovery, the detrapping behavior was not sensitive to the particular wavelength of the light used in the detrapping experiments.

Chapter 7

Conclusion

The original purpose of this study was to fabricate atomically controlled oxide thin film heterostructures and to investigate signatures of magnetism derived from the two-dimensional confinement of carriers at the interface by using magnetotransport analysis. Delta-doped $SrTiO_3$ / $LaTiO_3$ / $SrTiO_3$ heterostructures were fabricated and characterized. Hall effect and magnetotransport measurements were performed at 2 ~ 300 K in different applied magnetic field configurations.

Samples were grown with different $LaTiO_3$ thicknesses by pulsed laser deposition. The thickness of the atomic layer was evaluated by counting RHEED oscillations and a clear step-and-terrace structure was confirmed by AFM even on the surface of the final $SrTiO_3$ capping layer, ensuring that the heterostructure interfaces were atomically flat.

With those samples, transport properties were confirmed to be tunable from a metallic to an insulating state by a simple adjustment of either the number of La atoms in the doping layer or the thickness of a $SrTiO_3$ cap layer.

Non-linear Hall resistance was analyzed with the help of a two-carrier model that applies to systems with several types of carriers that contribute to the current flow in a parallel circuit configuration. The parallel conduction paths lead to a magnetic field dependent non-linear Hall resistance. The fitting showed that there is a set of carriers with a high carrier density but low mobility at the interface, and low carrier density with high mobility deeper in the $SrTiO_3$ substrate.

Since only ~10% of the carriers doped from $LaTiO_3$ layer were found to contribute the conductivity, it is important to investigate the carrier behavior in the applied magnetic field. The positive out-of-plane magnetoresistance was parabolic at low magnetic fields and became linear for high fields. This tendency became stronger in heterostructures with thicker $LaTiO_3$ films, i.e. higher total carrier number. In contrast, the strong

negative in-plane magnetoresistance observed at low temperature, possibly due to the interface spin-orbit interaction.

A strong temperature and $LaTiO_3$ layer thickness dependence was found in both Hall and magnetoresistance measurements. The temperature dependent transport properties followed the strongly temperature-dependent permittivity of bulk $SrTiO_3$. The $LaTiO_3$ thickness was shown to influence the total carrier number injected into the quantum well.

The electric field effect was used to tune the carrier confinement potential profile of the heterostructures. By applying a negative bias voltage, the quantum well could be compressed and the sample resistance grew rapidly. A positive gate bias appears to broaden the quantum well, which induced the spilling of carriers out of the interfacial quantum well and trapping of those spilled carriers deeper in the substrate, leading to only a slight decrease of resistance. Electrons that escaped from the quantum well could not be recovered by negative biasing and a strong irreversible resistance change was observed. The memory effect could be reset by warming a sample to room temperature or by illuminating a sample with light.

To conclude, $LaTiO_3/SrTiO_3$ heterostructures are suitable for obtaining controlled carrier densities by changing the layer thickness or by applying gate bias. With broad tunability that may allow easier observation of filling-dependent spin-orbit interaction, this system is shown to be a great stage to test the spin physics and to construct spintronic devices.

Bibliography

[1] H. Y. Hwang, Y. Iwasa, M. Kawasaki, B. Keimer, N. Nagaosa, and Y. Tokura. Emergent phenomena at oxide interfaces. *Nature Materials*, 11(2):103–113, January 2012. doi: 10.1038/nmat3223. URL https://doi.org/10.1038/nmat3223.

[2] Elbio Dagotto. Complexity in strongly correlated electronic systems. *Science*, 309(5732):257–262, 2005. ISSN 0036-8075. doi: 10.1126/science.1107559. URL https://science.sciencemag.org/content/309/5732/257.

[3] J. F. Mitchell, D. N. Argyriou, A. Berger, K. E. Gray, R. Osborn, and U. Welp. Spin, charge, and lattice states in layered magnetoresistive oxides. *The Journal of Physical Chemistry B*, 105(44):10731–10745, 2001. doi: 10.1021/jp011419u. URL https://doi.org/10.1021/jp011419u.

[4] S. Nakatsuji and Y. Maeno. Quasi-two-dimensional mott transition system $Ca_{2-x}Sr_xRuO_4$. *Physical Review Letters*, 84:2666–2669, Mar 2000. doi: 10.1103/PhysRevLett.84.2666. URL https://link.aps.org/doi/10.1103/PhysRevLett.84.2666.

[5] S. Nakatsuji, V. Dobrosavljević, D. Tanasković, M. Minakata, H. Fukazawa, and Y. Maeno. Mechanism of hopping transport in disordered mott insulators. *Physical Review Letters*, 93:146401, Sep 2004. doi: 10.1103/PhysRevLett.93.146401. URL https://link.aps.org/doi/10.1103/PhysRevLett.93.146401.

[6] Maw Lin Foo, Yayu Wang, Satoshi Watauchi, H. W. Zandbergen, Tao He, R. J. Cava, and N. P. Ong. Charge ordering, commensurability, and metallicity in the phase diagram of the layered Na_xCoO_2. *Physical Review Letters*, 92(24), June 2004. doi: 10.1103/physrevlett.92.247001. URL https://doi.org/10.1103/physrevlett.92.247001.

[7] URL https://en.wikipedia.org/wiki/Yttrium_barium_copper_oxide.

[8] Neeraj Khare. *Handbook of High-Temperature Superconductor Electronics (Applied Physics)*. CRC Press, 2003. ISBN 0824708237.

[9] Satoshi Okamoto, Andrew J. Millis, and Nicola A. Spaldin. Lattice relaxation in oxide heterostructures: $LaTiO_3/SrTiO_3$ superlattices. *Physical Review Letters*, 97 (5):4–7, 2006. ISSN 00319007. doi: 10.1103/PhysRevLett.97.056802. URL https://doi.org/10.1103/PhysRevLett.97.056802.

[10] Satoshi Okamoto and Andrew J. Millis. Electronic reconstruction at an interface between a Mott insulator and a band insulator. *Nature*, 428(6983):630–633, 2004. ISSN 00280836. doi: 10.1038/nature02450.

[11] N. Reyren, M. Bibes, E. Lesne, J. M. George, C. Deranlot, S. Collin, A. Barthélémy, and H. Jaffrès. Gate-controlled spin injection at $LaAlO_3/SrTiO_3$ interfaces. *Physical Review Letters*, 108(18):1–5, 2012. ISSN 00319007. doi: 10.1103/PhysRevLett.108.186802.

[12] Diogo C. Vaz, Paul Noël, Annika Johansson, Börge Göbel, Flavio Y. Bruno, Gyanendra Singh, Siobhan McKeown-Walker, Felix Trier, Luis M. Vicente-Arche, Anke Sander, Sergio Valencia, Pierre Bruneel, Manali Vivek, Marc Gabay, Nicolas Bergeal, Felix Baumberger, Hanako Okuno, Agnès Barthélémy, Albert Fert, Laurent Vila, Ingrid Mertig, Jean-Philippe Attané, and Manuel Bibes. Mapping spin–charge conversion to the band structure in a topological oxide two-dimensional electron gas. *Nature Materials*, 18(11):1187–1193, 2019. doi: 10.1038/s41563-019-0467-4. URL https://doi.org/10.1038/s41563-019-0467-4.

[13] Mark Fox and Radu Ispasoiu. Quantum wells, superlattices, and band-gap engineering. In *Springer Handbook of Electronic and Photonic Materials*, pages 1–1. Springer International Publishing, 2017. doi: 10.1007/978-3-319-48933-9_40. URL https://doi.org/10.1007/978-3-319-48933-9_40.

[14] Y. Kozuka, A. Tsukazaki, D. Maryenko, J. Falson, S. Akasaka, K. Nakahara, S. Nakamura, S. Awaji, K. Ueno, and M. Kawasaki. Insulating phase of a two-dimensional electron gas in $Mg_xZn_{1-x}O/ZnO$ heterostructures below $\nu = \frac{1}{3}$. *Physical Review B*, 84:033304, Jul 2011. doi: 10.1103/PhysRevB.84.033304. URL https://link.aps.org/doi/10.1103/PhysRevB.84.033304.

[15] A. Tsukazaki, S. Akasaka, K. Nakahara, Y. Ohno, H. Ohno, D. Maryenko, A. Ohtomo, and M. Kawasaki. Observation of the fractional quantum Hall effect

in an oxide. *Nature Materials*, 9(11):889–893, 2010. doi: 10.1038/nmat2874. URL https://doi.org/10.1038/nmat2874.

[16] Joseph Falson, Yusuke Kozuka, Masaki Uchida, Jurgen H. Smet, Taka-hisa Arima, Atsushi Tsukazaki, and Masashi Kawasaki. MgZnO/ZnO heterostructures with electron mobility exceeding $1 \times 10^{6} \mathrm{cm}^2/\mathrm{vs}$. *Scientific Reports*, 6(1):26598, 2016. doi: 10.1038/srep26598. URL https://doi.org/10.1038/srep26598.

[17] J. Betancourt, J. J. Saavedra-Arias, J. D. Burton, Y. Ishikawa, E. Y. Tsymbal, and J. P. Velev. Polarization discontinuity induced two-dimensional electron gas at ZnO/Zn(Mg)O interfaces: A first-principles study. *Physical Review B*, 88:085418, Aug 2013. doi: 10.1103/PhysRevB.88.085418. URL https://link.aps.org/doi/10.1103/PhysRevB.88.085418.

[18] Joseph Falson and Masashi Kawasaki. A review of the quantum Hall effects in MgZnO/ZnO heterostructures. *Reports on Progress in Physics*, 81(5):056501, March 2018. doi: 10.1088/1361-6633/aaa978. URL https://doi.org/10.1088/1361-6633/aaa978.

[19] A Ohtomo and H Y Hwang. A high-mobility electron gas at the $LaAlO_3/SrTiO_3$ heterointerface. *Nature*, 427(6973):423–426, jan 2004. ISSN 0028-0836. doi: 10.1038/nature02308. URL http://www.nature.com/articles/nature02308.

[20] A. Bhattacharya, S. J. May, S. G. E. te Velthuis, M. Warusawithana, X. Zhai, Bin Jiang, J.-M. Zuo, M. R. Fitzsimmons, S. D. Bader, and J. N. Eckstein. Metal-insulator transition and its relation to magnetic structure in $(LaMnO_3)_{2n}/(SrMnO_3)_n$ superlattices. *Physical Review Letters*, 100:257203, Jun 2008. doi: 10.1103/PhysRevLett.100.257203. URL https://link.aps.org/doi/10.1103/PhysRevLett.100.257203.

[21] Clayton A. Jackson and Susanne Stemmer. Interface-induced magnetism in perovskite quantum wells. *Physical Review B - Condensed Matter and Materials Physics*, 88(18):88–91, 2013. ISSN 10980121. doi: 10.1103/PhysRevB.88.180403. URL https://doi.org/10.1103/PhysRevB.88.180403.

[22] Jaekwang Lee, Na Sai, and Alexander A. Demkov. Spin-polarized two-dimensional electron gas through electrostatic doping in $LaAlO_3$/EuO heterostructures. *Physical Review B*, 82:235305, Dec 2010. doi: 10.1103/PhysRevB.82.235305. URL https://link.aps.org/doi/10.1103/PhysRevB.82.235305.

[23] M. A. Peña and J. L. G. Fierro. Chemical structures and performance of perovskite oxides. *Chemical Reviews*, 101(7):1981–2018, 07 2001. doi: 10.1021/cr980129f. URL https://doi.org/10.1021/cr980129f.

[24] P Granger. *Perovskites and related mixed oxides : concepts and applications*. Wiley-VCH, Weinheim, 2016. ISBN 9783527337637.

[25] V. M. Goldschmidt. Geochemische verteilungsgesetze der elemente. *Skrifter Norske Videnskaps*, 1926.

[26] Masashi Kawasaki, Kazuhiro Takahashi, Tatsuro Maeda, Ryuta Tsuchiya, Makoto Shinohara, Osamu Ishiyama, Takuzo Yonezawa, Mamoru Yoshimoto, and Hideomi Koinuma. Atomic control of the $SrTiO_3$ crystal surface. *Science*, 266 (5190):1540–1542, 1994. ISSN 0036-8075. doi: 10.1126/science.266.5190.1540. URL https://science.sciencemag.org/content/266/5190/1540.

[27] Farrel W. Lytle. X-ray diffractometry of low-temperature phase transformations in strontium titanate. *Journal of Applied Physics*, 35(7):2212–2215, 1964. doi: 10.1063/1.1702820. URL https://doi.org/10.1063/1.1702820.

[28] Hiromi Unoki and Tunetaro Sakudo. Electron spin resonance of Fe^{3+} in $SrTiO_3$ with special reference to the 110°K phase transition. *Journal of the Physical Society of Japan*, 23(3):546–552, 1967. doi: 10.1143/JPSJ.23.546. URL https://doi.org/10.1143/JPSJ.23.546.

[29] L. F. Mattheiss. Effect of the 110°k phase transition on the $SrTiO_3$ conduction bands. *Physical Review B*, 6:4740–4753, Dec 1972. doi: 10.1103/PhysRevB.6.4740. URL https://link.aps.org/doi/10.1103/PhysRevB.6.4740.

[30] James A. Noland. Optical absorption of single-crystal strontium titanate. *Physical Review*, 94:724–724, May 1954. doi: 10.1103/PhysRev.94.724. URL https://link.aps.org/doi/10.1103/PhysRev.94.724.

[31] E. Heifets, R. I. Eglitis, E. A. Kotomin, J. Maier, and G. Borstel. First-principles calculations for $SrTiO_3$ (100) surface structure. *Surface Science*, 513 (1):211–220, 2002. doi: https://doi.org/10.1016/S0039-6028(02)01730-2. URL http://www.sciencedirect.com/science/article/pii/S0039602802017302.

[32] Feng Pan, David Olaya, John C. Price, and Charles T. Rogers. Thin-film field-effect transistors based on La-doped $SrTiO_3$ heterostructures. *Applied Physics Letters*, 84

(9):1573–1575, 2004. doi: 10.1063/1.1651647. URL https://doi.org/10.1063/1.1651647.

[33] L. Pellegrino, I. Pallecchi, D. Marré, E. Bellingeri, and A. S. Siri. Fabrication of submicron-scale $SrTiO_{3-\delta}$ devices by an atomic force microscope. *Applied Physics Letters*, 81(20):3849–3851, 2002. doi: 10.1063/1.1521583. URL https://doi.org/10.1063/1.1521583.

[34] H. P. R. Frederikse, W. R. Thurber, and W. R. Hosler. Electronic transport in strontium titanate. *Physical Rev.*, 134:A442–A445, Apr 1964. doi: 10.1103/PhysRev.134.A442. URL https://link.aps.org/doi/10.1103/PhysRev.134.A442.

[35] O. N. Tufte and P. W. Chapman. Electron mobility in semiconducting strontium titanate. *Physical Review*, 155(3):796–802, 1967. ISSN 0031899X. doi: 10.1103/PhysRev.155.796. URL https://doi.org/10.1103/PhysRev.155.796.

[36] Xiao Lin, German Bridoux, Adrien Gourgout, Gabriel Seyfarth, Steffen Krämer, Marc Nardone, Benoît Fauqué, and Kamran Behnia. Critical doping for the onset of a two-band superconducting ground state in $SrTiO_{3-\delta}$. *Physical Review Letters*, 112(20), May 2014. doi: 10.1103/physrevlett.112.207002. URL https://doi.org/10.1103/physrevlett.112.207002.

[37] J. F. Schooley, W. R. Hosler, E. Ambler, J. H. Becker, Marvin L. Cohen, and C. S. Koonce. Dependence of the superconducting transition temperature on carrier concentration in semiconducting $SrTiO_3$. *Physical Review Letters*, 14:305–307, Mar 1965. doi: 10.1103/PhysRevLett.14.305. URL https://link.aps.org/doi/10.1103/PhysRevLett.14.305.

[38] B. K. Choudhury, K. V. Rao, and R. N. P. Choudhury. Dielectric properties of $SrTiO_3$ single crystals subjected to high electric fields and later irradiated with X-rays or γ-rays. *Journal of Materials Science*, 24(10):3469–3474, 1989. doi: 10.1007/BF02385726. URL https://doi.org/10.1007/BF02385726.

[39] T. Sakudo and H. Unoki. Dielectric properties of $SrTiO_3$ at low temperatures. *Physical Review Letters*, 26:851–853, Apr 1971. doi: 10.1103/PhysRevLett.26.851. URL https://link.aps.org/doi/10.1103/PhysRevLett.26.851.

[40] R. C. Neville, B. Hoeneisen, and C. A. Mead. Permittivity of strontium titanate. *Journal of Applied Physics*, 43(5):2124–2131, 1972. ISSN 00218979. doi: 10.1063/1.1661463. URL https://doi.org/10.1063/1.1661463.

[41] Hiromoto Uwe and Tunetaro Sakudo. Stress-induced ferroelectricity and soft phonon modes in $SrTiO_3$. *Physical Review B*, 13:271–286, Jan 1976. doi: 10.1103/PhysRevB.13.271. URL https://link.aps.org/doi/10.1103/PhysRevB.13.271.

[42] Seung-Gu Lim, Stas Kriventsov, Thomas N. Jackson, J. H. Haeni, D. G. Schlom, A. M. Balbashov, R. Uecker, P. Reiche, J. L. Freeouf, and G. Lucovsky. Dielectric functions and optical bandgaps of high-K dielectrics for metal-oxide-semiconductor field-effect transistors by far ultraviolet spectroscopic ellipsometry. *Journal of Applied Physics*, 91(7):4500–4505, 2002. doi: 10.1063/1.1456246. URL https://doi.org/10.1063/1.1456246.

[43] J. Konopka and I. Wolff. Dielectric properties of substrates for deposition of high-t_c thin films up to 40 GHz. *IEEE Transactions on Microwave Theory and Techniques*, 40(12):2418–2423, 1992. URL https://doi.org/10.1109/22.179911.

[44] P. D. Eerkes, W. G. Van Der Wiel, and H. Hilgenkamp. Modulation of conductance and superconductivity by top-gating in $LaAlO_3/SrTiO_3$ 2-dimensional electron systems. *Applied Physics Letters*, 103(20):2–6, 2013. ISSN 00036951. doi: 10.1063/1.4829555. URL https://doi.org/10.1063/1.4829555.

[45] S. Hurand, A. Jouan, C. Feuillet-Palma, G. Singh, J. Biscaras, E. Lesne, N. Reyren, A. Barthélémy, M. Bibes, J. E. Villegas, C. Ulysse, X. Lafosse, M. Pannetier-Lecoeur, S. Caprara, M. Grilli, J. Lesueur, and N. Bergeal. Field-effect control of superconductivity and Rashba spin-orbit coupling in top-gated $LaAlO_3/SrTiO_3$ devices. *Sci. Rep.*, 5(August):1–9, 2015. ISSN 20452322. doi: 10.1038/srep12751. URL http://dx.doi.org/10.1038/srep12751.

[46] Masayuki Hosoda, Yasuyuki Hikita, Harold Y. Hwang, and Christopher Bell. Transistor operation and mobility enhancement in top-gated $LaAlO_3/SrTiO_3$ heterostructures. *Applied Physics Letters*, 103(10):3–6, 2013. ISSN 00036951. doi: 10.1063/1.4820449. URL https://doi.org/10.1063/1.4820449.

[47] A. E.M. Smink, J. C. De Boer, M. P. Stehno, A. Brinkman, W. G. Van Der Wiel, and H. Hilgenkamp. Gate-Tunable Band Structure of the $LaAlO_3$-$SrTiO_3$ Interface. *Physical Review Letters*, 118(10):3–8, 2017. ISSN 10797114. doi: 10.1103/PhysRevLett.118.106401. URL https://doi.org/10.1103/PhysRevLett.118.106401.

[48] W. Liu, S. Gariglio, A. Fête, D. Li, M. Boselli, D. Stornaiuolo, and J. M. Triscone. Magneto-transport study of top- and back-gated $LaAlO_3/SrTiO_3$ heterostructures. *APL Mater.*, 3(6):062805, 2015. ISSN 2166532X. doi: 10.1063/1.4921068. URL https://doi.org/10.1063/1.4921068.

[49] S Thiel, G Hammerl, A Schmehl, C. W. Schneider, and J Mannhart. Tunable quasi-two-dimensional electron gases in oxide heterostructures. *Science*, 313(5795): 1942–1945, sep 2006. ISSN 00368075. doi: 10.1126/science.1131091. URL https://www.sciencemag.org/lookup/doi/10.1126/science.1131091.

[50] G. Herranz, M. Basletić, M. Bibes, C. Carrétéro, E. Tafra, E. Jacquet, K. Bouzehouane, C. Deranlot, A. Hamzić, J.-M. Broto, A. Barthélémy, and A. Fert. High Mobility in $LaAlO_3/SrTiO_3$ Heterostructures: Origin, Dimensionality, and Perspectives. *Physical Review Letters*, 98:216803, May 2007. doi: 10.1103/PhysRevLett.98.216803. URL https://link.aps.org/doi/10.1103/PhysRevLett.98.216803.

[51] N. Reyren, S. Thiel, A. D. Caviglia, L. F. Kourkoutis, G. Hammerl, C. Richter, C. W. Schneider, T. Kopp, A.-S. Ruetschi, D. Jaccard, M. Gabay, D. A. Muller, J.-M. Triscone, and J. Mannhart. Superconducting Interfaces Between Insulating Oxides. *Science*, 317(5842):1196–1199, aug 2007. ISSN 0036-8075. doi: 10.1126/science.1146006. URL https://www.sciencemag.org/lookup/doi/10.1126/science.1146006.

[52] M. Basletic, J. L. Maurice, C. Carrétéro, G. Herranz, O. Copie, M. Bibes, É. Jacquet, K. Bouzehouane, S. Fusil, and A. Barthélémy. Mapping the spatial distribution of charge carriers in $LaAlO_3/SrTiO_3$ heterostructures. *Nature Materials*, 7(8):621–625, 2008. doi: 10.1038/nmat2223. URL https://doi.org/10.1038/nmat2223.

[53] O. Copie, V. Garcia, C. Bödefeld, C. Carrétéro, M. Bibes, G. Herranz, E. Jacquet, J.-L. Maurice, B. Vinter, S. Fusil, K. Bouzehouane, H. Jaffrès, and A. Barthélémy. Towards two-dimensional metallic behavior at $LaAlO_3/SrTiO_3$ interfaces. *Physical Review Letters*, 102:216804, May 2009. doi: 10.1103/PhysRevLett.102.216804. URL https://link.aps.org/doi/10.1103/PhysRevLett.102.216804.

[54] S Gariglio, N Reyren, A D Caviglia, and J-M Triscone. Superconductivity at the $LaAlO_3/SrTiO_3$ interface. *Journal of Physics: Condensed Matter*, 21(16):164213, mar 2009. doi: 10.1088/0953-8984/21/16/164213. URL https://doi.org/10.1088%2F0953-8984%2F21%2F16%2F164213.

[55] Julie A. Bert, Beena Kalisky, Christopher Bell, Minu Kim, Yasuyuki Hikita, Harold Y. Hwang, and Kathryn A. Moler. Direct imaging of the coexistence of ferromagnetism and superconductivity at the $LaAlO_3/SrTiO_3$ interface. *Nature Physics*, 7(10):767–771, 2011. ISSN 17452473. doi: 10.1038/nphys2079. URL https://doi.org/10.1038/nphys2079.

[56] Lu Li, C. Richter, J. Mannhart, and R. C. Ashoori. Coexistence of magnetic order and two-dimensional superconductivity at $LaAlO_3/SrTiO_3$ interfaces. *Nature Physics*, 7(10):762–766, 2011. ISSN 17452473. doi: 10.1038/nphys2080. URL https://doi.org/10.1038/nphys2080.

[57] A. Brinkman, M. Huijben, M. Van Zalk, J. Huijben, U. Zeitler, J. C. Maan, W. G. Van Der Wiel, G. Rijnders, D. H.A. Blank, and H. Hilgenkamp. Magnetic effects at the interface between non-magnetic oxides. *Nature Materials*, 6(7):493–496, 2007. ISSN 14764660. doi: 10.1038/nmat1931. URL https://doi.org/10.1038/nmat1931.

[58] W. D. Rice, P. Ambwani, M. Bombeck, J. D. Thompson, G. Haugstad, C. Leighton, and S. A. Crooker. Persistent optically induced magnetism in oxygen-deficient strontium titanate. *Nature Materials*, 13(5):481–487, March 2014. doi: 10.1038/nmat3914. URL https://doi.org/10.1038/nmat3914.

[59] Yoshihito Motoyui, Toshiyuki Taniuchi, Philipp Scheiderer, Jiyeon N. Lee, Judith Gabel, Florian Pfaff, Michael Sing, Mikk Lippmaa, Ralph Claessen, and Shik Shin. Imaging the formation of ferromagnetic domains at the $LaAlO_3/SrTiO_3$ interface. *Journal of the Physical Society of Japan*, 88(3):034717, March 2019. doi: 10.7566/jpsj.88.034717. URL https://doi.org/10.7566/jpsj.88.034717.

[60] M. Salluzzo, J. C. Cezar, N. B. Brookes, V. Bisogni, G. M. De Luca, C. Richter, S. Thiel, J. Mannhart, M. Huijben, A. Brinkman, G. Rijnders, and G. Ghiringhelli. Orbital reconstruction and the two-dimensional electron gas at the $LaAlO_3/SrTiO_3$ interface. *Physical Review Letters*, 102:166804, Apr 2009. doi: 10.1103/PhysRevLett.102.166804. URL https://link.aps.org/doi/10.1103/PhysRevLett.102.166804.

[61] M. Salluzzo, S. Gariglio, D. Stornaiuolo, V. Sessi, S. Rusponi, C. Piamonteze, G. M. De Luca, M. Minola, D. Marré, A. Gadaleta, H. Brune, F. Nolting, N. B. Brookes, and G. Ghiringhelli. Origin of interface magnetism in $BiMnO_3/SrTiO_3$ and $LaAlO_3/SrTiO_3$ heterostructures. *Physical Review Letters*, 111:087204, Aug

2013. doi: 10.1103/PhysRevLett.111.087204. URL https://link.aps.org/doi/10.1103/PhysRevLett.111.087204.

[62] Masatoshi Imada Youhei Yamaji, Takahiro Misawa. Quantum and topological criticalities of Lifshitz transition in two-dimensional correlated electron systems. *Journal of the Physical Society of Japan*, 75(9):1–16, 2006. ISSN 00319015. doi: 10.1143/JPSJ.75.094719. URL https://doi.org/10.1143/JPSJ.75.094719.

[63] Arjun Joshua, S. Pecker, J. Ruhman, E. Altman, and S. Ilani. A universal critical density underlying the physics of electrons at the $LaAlO_3/SrTiO_3$ interface. *Nature Communications*, 3, 2012. ISSN 20411723. doi: 10.1038/ncomms2116. URL https://doi.org/10.1038/ncomms2116.

[64] Naoyuki Nakagawa, Harold Y. Hwang, and David A. Muller. Why some interfaces cannot be sharp. *Nature Materials*, 5(3):204–209, 2006. ISSN 14764660. doi: 10.1038/nmat1569. URL https://doi.org/10.1038/nmat1569.

[65] Y. Segal, J. H. Ngai, J. W. Reiner, F. J. Walker, and C. H. Ahn. X-ray photoemission studies of the metal-insulator transition in $LaAlO_3/SrTiO_3$ structures grown by molecular beam epitaxy. *Physical Review B*, 80:241107, Dec 2009. doi: 10.1103/PhysRevB.80.241107. URL https://link.aps.org/doi/10.1103/PhysRevB.80.241107.

[66] J. Verbeeck, S. Bals, A. N. Kravtsova, D. Lamoen, M. Luysberg, M. Huijben, G. Rijnders, A. Brinkman, H. Hilgenkamp, D. H. A. Blank, and G. Van Tendeloo. Electronic reconstruction at *n*-type $SrTiO_3/LaAlO_3$ interfaces. *Physical Review B*, 81:085113, Feb 2010. doi: 10.1103/PhysRevB.81.085113. URL https://link.aps.org/doi/10.1103/PhysRevB.81.085113.

[67] K. Yoshimatsu, R. Yasuhara, H. Kumigashira, and M. Oshima. Origin of metallic states at the heterointerface between the band insulators $LaAlO_3$ and $SrTiO_3$. *Physical Review Letters*, 101:026802, Jul 2008. doi: 10.1103/PhysRevLett.101.026802. URL https://link.aps.org/doi/10.1103/PhysRevLett.101.026802.

[68] P. R. Willmott, S. A. Pauli, R. Herger, C. M. Schlepütz, D. Martoccia, B. D. Patterson, B. Delley, R. Clarke, D. Kumah, C. Cionca, and Y. Yacoby. Structural basis for the conducting interface between $LaAlO_3$ and $SrTiO_3$. *Physical Review Letters*, 99:155502, Oct 2007. doi: 10.1103/PhysRevLett.99.155502. URL https://link.aps.org/doi/10.1103/PhysRevLett.99.155502.

[69] M. L. Reinle-Schmitt, C. Cancellieri, D. Li, D. Fontaine, M. Medarde, E. Pomjakushina, C. W. Schneider, S. Gariglio, Ph. Ghosez, J. M. Triscone, and P. R. Willmott. Tunable conductivity threshold at polar oxide interfaces. *Nature Communications*, 3(1):932, 2012. doi: 10.1038/ncomms1936. URL https://doi.org/10.1038/ncomms1936.

[70] Won-joon Son, Eunae Cho, Bora Lee, Jaichan Lee, and Seungwu Han. Density and spatial distribution of charge carriers in the intrinsic *n*-type $LaAlO_3/SrTiO_3$ interface. *Physical Review B*, 79:245411, Jun 2009. doi: 10.1103/PhysRevB.79.245411. URL https://link.aps.org/doi/10.1103/PhysRevB.79.245411.

[71] A. Savoia, D. Paparo, P. Perna, Z. Ristic, M. Salluzzo, F. Miletto Granozio, U. Scotti di Uccio, C. Richter, S. Thiel, J. Mannhart, and L. Marrucci. Polar catastrophe and electronic reconstructions at the $LaAlO_3/SrTiO_3$ interface: Evidence from optical second harmonic generation. *Physical Review B*, 80:075110, Aug 2009. doi: 10.1103/PhysRevB.80.075110. URL https://link.aps.org/doi/10.1103/PhysRevB.80.075110.

[72] Yanwu Xie, Christopher Bell, Takeaki Yajima, Yasuyuki Hikita, and Harold Y. Hwang. Charge writing at the $LaAlO_3/SrTiO_3$ surface. *Nano Letters*, 10(7): 2588–2591, 07 2010. doi: 10.1021/nl1012695. URL https://doi.org/10.1021/nl1012695.

[73] Yanwu Xie, Yasuyuki Hikita, Christopher Bell, and Harold Y. Hwang. Control of electronic conduction at an oxide heterointerface using surface polar adsorbates. *Nature Communications*, 2(1):494, 2011. doi: 10.1038/ncomms1501. URL https://doi.org/10.1038/ncomms1501.

[74] A. D. Caviglia, S. Gariglio, C. Cancellieri, B. Sacépé, A. Fête, N. Reyren, M. Gabay, A. F. Morpurgo, and J.-M. Triscone. Two-dimensional quantum oscillations of the conductance at $LaAlO_3/SrTiO_3$ interfaces. *Physical Review Letters*, 105:236802, Dec 2010. doi: 10.1103/PhysRevLett.105.236802. URL https://link.aps.org/doi/10.1103/PhysRevLett.105.236802.

[75] M. Ben Shalom, C. W. Tai, Y. Lereah, M. Sachs, E. Levy, D. Rakhmilevitch, A. Palevski, and Y. Dagan. Anisotropic magnetotransport at the $SrTiO_3/LaAlO_3$ interface. *Physical Review B*, 80:140403, Oct 2009. doi: 10.1103/PhysRevB.80.140403. URL https://link.aps.org/doi/10.1103/PhysRevB.80.140403.

[76] C. Bell, S. Harashima, Y. Kozuka, M. Kim, B. G. Kim, Y. Hikita, and H. Y. Hwang. Dominant mobility modulation by the electric field effect at the $LaAlO_3/SrTiO_3$ interface. *Physical Review Letters*, 103(22):25–28, 2009. ISSN 00319007. doi: 10.1103/PhysRevLett.103.226802. URL https://doi.org/10.1103/PhysRevLett.103.226802.

[77] G. Berner, A. Müller, F. Pfaff, J. Walde, C. Richter, J. Mannhart, S. Thiess, A. Gloskovskii, W. Drube, M. Sing, and R. Claessen. Band alignment in $laalo_3/srtio_3$ oxide heterostructures inferred from hard x-ray photoelectron spectroscopy. *Physical Review B*, 88:115111, Sep 2013. doi: 10.1103/PhysRevB.88.115111. URL https://link.aps.org/doi/10.1103/PhysRevB.88.115111.

[78] E. Slooten, Zhicheng Zhong, H. J. A. Molegraaf, P. D. Eerkes, S. de Jong, F. Massee, E. van Heumen, M. K. Kruize, S. Wenderich, J. E. Kleibeuker, M. Gorgoi, H. Hilgenkamp, A. Brinkman, M. Huijben, G. Rijnders, D. H. A. Blank, G. Koster, P. J. Kelly, and M. S. Golden. Hard x-ray photoemission and density functional theory study of the internal electric field in $SrTiO_3/LaAlO_3$ oxide heterostructures. *Physical Review B*, 87:085128, Feb 2013. doi: 10.1103/PhysRevB.87.085128. URL https://link.aps.org/doi/10.1103/PhysRevB.87.085128.

[79] M. Takizawa, S. Tsuda, T. Susaki, H. Y. Hwang, and A. Fujimori. Electronic charges and electric potential at $LaAlO_3/SrTiO_3$ interfaces studied by core-level photoemission spectroscopy. *Physical Review B*, 84:245124, Dec 2011. doi: 10.1103/PhysRevB.84.245124. URL https://link.aps.org/doi/10.1103/PhysRevB.84.245124.

[80] Yunzhong Chen, Nini Pryds, Josée E. Kleibeuker, Gertjan Koster, Jirong Sun, Eugen Stamate, Baogen Shen, Guus Rijnders, and Søren Linderoth. Metallic and insulating interfaces of amorphous $SrTiO_3$-based oxide heterostructures. *Nano Letters*, 11(9):3774–3778, 09 2011. doi: 10.1021/nl201821j. URL https://doi.org/10.1021/nl201821j.

[81] A. Annadi, Q. Zhang, X. Renshaw Wang, N. Tuzla, K. Gopinadhan, W. M. Lü, A. Roy Barman, Z. Q. Liu, A. Srivastava, S. Saha, Y. L. Zhao, S. W. Zeng, S. Dhar, E. Olsson, B. Gu, S. Yunoki, S. Maekawa, H. Hilgenkamp, T. Venkatesan, and Ariando. Anisotropic two-dimensional electron gas at the $LaAlO_3/SrTiO_3$ (110) interface. *Nature Communications*, 4(1):1838, 2013. doi: 10.1038/ncomms2804. URL https://doi.org/10.1038/ncomms2804.

[82] G. Herranz, F. Sánchez, N. Dix, M. Scigaj, and J. Fontcuberta. High mobility conduction at (110) and (111) $LaAlO_3/SrTiO_3$ interfaces. *Scientific Reports*, 2(1): 758, 2012. doi: 10.1038/srep00758. URL https://doi.org/10.1038/srep00758.

[83] F. Gunkel, S. Hoffmann-Eifert, R. Dittmann, S. B. Mi, C. L. Jia, P. Meuffels, and R. Waser. High temperature conductance characteristics of $LaAlO_3/SrTiO_3$-heterostructures under equilibrium oxygen atmospheres. *Applied Physics Letters*, 97(1):012103, July 2010. doi: 10.1063/1.3457386. URL https://doi.org/10.1063/1.3457386.

[84] A. Kalabukhov, Yu. A. Boikov, I. T. Serenkov, V. I. Sakharov, J. Börjesson, N. Ljustina, E. Olsson, D. Winkler, and T. Claeson. Improved cationic stoichiometry and insulating behavior at the interface of $LaAlO_3/SrTiO_3$ formed at high oxygen pressure during pulsed-laser deposition. *EPL (Europhysics Letters)*, 93(3):37001, February 2011. doi: 10.1209/0295-5075/93/37001. URL https://doi.org/10.1209/0295-5075/93/37001.

[85] J. F. Schooley, W. R. Hosler, and Marvin L. Cohen. Superconductivity in semiconducting $SrTiO_3$. *Physical Review Letters*, 12:474–475, Apr 1964. doi: 10.1103/PhysRevLett.12.474. URL https://link.aps.org/doi/10.1103/PhysRevLett.12.474.

[86] I.R. Shein and A.L. Ivanovskii. First principle prediction of vacancy-induced magnetism in non-magnetic perovskite $SrTiO_3$. *Physics Letters A*, 371(1-2):155–159, November 2007. doi: 10.1016/j.physleta.2007.06.013. URL https://doi.org/10.1016/j.physleta.2007.06.013.

[87] Z. Q. Liu, C. J. Li, W. M. Lü, X. H. Huang, Z. Huang, S. W. Zeng, X. P. Qiu, L. S. Huang, A. Annadi, J. S. Chen, J. M. D. Coey, T. Venkatesan, and Ariando. Origin of the two-dimensional electron gas at $LaAlO_3/SrTiO_3$ interfaces: The role of oxygen vacancies and electronic reconstruction. *Physical Rev. X*, 3:021010, May 2013. doi: 10.1103/PhysRevX.3.021010. URL https://link.aps.org/doi/10.1103/PhysRevX.3.021010.

[88] Alexey Kalabukhov, Robert Gunnarsson, Johan Börjesson, Eva Olsson, Tord Claeson, and Dag Winkler. Effect of oxygen vacancies in the $SrTiO_3$ substrate on the electrical properties of the $LaAlO_3/SrTiO_3$ interface. *Physical Review B*, 75:121404, Mar 2007. doi: 10.1103/PhysRevB.75.121404. URL https://link.aps.org/doi/10.1103/PhysRevB.75.121404.

[89] Masatoshi Imada, Atsushi Fujimori, and Yoshinori Tokura. Metal-insulator transitions. *Reviews of Modern Physics*, 70:1039–1263, Oct 1998. doi: 10.1103/RevModPhys.70.1039. URL https://link.aps.org/doi/10.1103/RevModPhys.70.1039.

[90] D. A. Crandles, T. Timusk, J. D. Garrett, and J. E. Greedan. Mott insulator to correlated metal: Optical study of $La_{1-x}TiO_3$. *Physical Review B*, 49:16207–16213, Jun 1994. doi: 10.1103/PhysRevB.49.16207. URL https://link.aps.org/doi/10.1103/PhysRevB.49.16207.

[91] F. Lichtenberg, D. Widmer, J. G. Bednorz, T. Williams, and A. Reller. Phase diagram of $LaTiO_x$: from 2D layered ferroelectric insulator to 3D weak ferromagnetic semiconductor. *Zeitschrift für Physik B Condensed Matter*, 82(2):211–216, 1991. doi: 10.1007/BF01324328. URL https://doi.org/10.1007/BF01324328.

[92] M. Cwik, T. Lorenz, J. Baier, R. Müller, G. André, F. Bourée, F. Lichtenberg, A. Freimuth, R. Schmitz, E. Müller-Hartmann, and M. Braden. Crystal and magnetic structure of $LaTiO_3$: Evidence for non degenerate $t2g$ orbitals. *Physical Review B*, 68(6), August 2003. doi: 10.1103/physrevb.68.060401. URL https://doi.org/10.1103/physrevb.68.060401.

[93] Y. Taguchi, T. Okuda, M. Ohashi, C. Murayama, N. Môri, Y. Iye, and Y. Tokura. Critical behavior in $LaTiO_{3+\delta/2}$ in the vicinity of antiferromagnetic instability. *Physical Review B*, 59:7917–7924, Mar 1999. doi: 10.1103/PhysRevB.59.7917. URL https://link.aps.org/doi/10.1103/PhysRevB.59.7917.

[94] David A. MacLean, Hok-Nam Ng, and J.E. Greedan. Crystal structures and crystal chemistry of the $RETiO_3$ perovskites: RE = La, Nd, Sm, Gd, Y. *Journal of Solid State Chemistry*, 30(1):35–44, October 1979. doi: 10.1016/0022-4596(79)90127-0. URL https://doi.org/10.1016/0022-4596(79)90127-0.

[95] Rossitza Pentcheva and Warren E. Pickett. Correlation-driven charge order at the interface between a mott and a band insulator. *Physical Review Letters*, 99:016802, Jul 2007. doi: 10.1103/PhysRevLett.99.016802. URL https://link.aps.org/doi/10.1103/PhysRevLett.99.016802.

[96] S. Thulasi and S. Satpathy. Jellium model of the two-dimensional Airy electron gas at the perovskite titanate interface. *Physical Review B*, 73:125307, Mar 2006.

doi: 10.1103/PhysRevB.73.125307. URL https://link.aps.org/doi/10.1103/PhysRevB.73.125307.

[97] Z. S. Popovic and S. Satpathy. Wedge-Shaped Potential and Airy-Function Electron Localization in Oxide Superlattices. *Physical Review Letters*, 94:176805, May 2005. doi: 10.1103/PhysRevLett.94.176805. URL https://link.aps.org/doi/10.1103/PhysRevLett.94.176805.

[98] Satoshi Okamoto and Andrew J. Millis. Spatial inhomogeneity and strong correlation physics: A dynamical mean-field study of a model Mott-insulator–band-insulator heterostructure. *Physical Review B*, 70:241104, Dec 2004. doi: 10.1103/PhysRevB.70.241104. URL https://link.aps.org/doi/10.1103/PhysRevB.70.241104.

[99] S. S. Kancharla and E. Dagotto. Metallic interface at the boundary between band and Mott insulators. *Physical Review B*, 74:195427, Nov 2006. doi: 10.1103/PhysRevB.74.195427. URL https://link.aps.org/doi/10.1103/PhysRevB.74.195427.

[100] P. Larson, Z. S. Popović, and S. Satpathy. Lattice relaxation effects on the interface electron states in the perovskite oxide heterostructures:$LaTiO_3$ monolayer embedded in $SrTiO_3$. *Physical Review B*, 77(24), June 2008. doi: 10.1103/physrevb.77.245122. URL https://doi.org/10.1103/physrevb.77.245122.

[101] A. Ohtomo, D. A. Muller, J. L. Grazul, and H. Y. Hwang. Artificial charge-modulation in atomic-scale perovskite titanate superlattices. *Nature*, 419(6905): 378–380, 2002. ISSN 00280836. doi: 10.1038/nature00977. URL https://doi.org/10.1038/nature00977.

[102] Keisuke Shibuya, Tsuyoshi Ohnishi, Masashi Kawasaki, Hideomi Koinuma, and Mikk Lippmaa. Metallic $LaTiO_3$/ $SrTiO_3$ superlattice films on the $SrTiO_3$ (100) surface. *Japanese Journal of Applied Physics*, 43(No. 9A/B):L1178–L1180, aug 2004. doi: 10.1143/jjap.43.l1178. URL https://doi.org/10.1143%2Fjjap.43.l1178.

[103] Y. Tokura, Y. Taguchi, Y. Okada, Y. Fujishima, T. Arima, K. Kumagai, and Y. Iye. Filling dependence of electronic properties on the verge of metal–mott-insulator transition in $Sr_{1-x}La_xTiO_3$. *Physical Review Letters*, 70:2126–2129, Apr 1993. doi: 10.1103/PhysRevLett.70.2126. URL https://link.aps.org/doi/10.1103/PhysRevLett.70.2126.

[104] M. Takizawa, H. Wadati, K. Tanaka, M. Hashimoto, T. Yoshida, A. Fujimori, A. Chikamatsu, H. Kumigashira, M. Oshima, K. Shibuya, T. Mihara, T. Ohnishi, M. Lippmaa, M. Kawasaki, H. Koinuma, S. Okamoto, and A. J. Millis. Photoemission from buried interfaces in $SrTiO_3/LaTiO_3$ superlattices. *Physical Review Letters*, 97(5):4–7, 2006. ISSN 00319007. doi: 10.1103/PhysRevLett.97.057601.

[105] S. S. A. Seo, W. S. Choi, H. N. Lee, L. Yu, K. W. Kim, C. Bernhard, and T. W. Noh. Optical study of the free-carrier response of $LaTiO_3/SrTiO_3$ superlattices. *Physical Review Letters*, 99:266801, Dec 2007. doi: 10.1103/PhysRevLett.99.266801. URL https://link.aps.org/doi/10.1103/PhysRevLett.99.266801.

[106] J. S. Kim, S. S.A. Seo, M. F. Chisholm, R. K. Kremer, H. U. Habermeier, B. Keimer, and H. N. Lee. Nonlinear Hall effect and multichannel conduction in $LaTiO_3/SrTiO_3$ superlattices. *Physical Review B - Condensed Matter and Materials Physics*, 82(20):2–5, 2010. ISSN 10980121. doi: 10.1103/PhysRevB.82.201407. URL https://doi.org/10.1103/PhysRevB.82.201407.

[107] D. G. Liu, C. P. Lee, K. H. Chang, J. S. Wu, and D. C. Liou. Delta-doped quantum well structures grown by molecular beam epitaxy. *Applied Physics Letters*, 57(18): 1887–1888, October 1990. doi: 10.1063/1.104001. URL https://doi.org/10.1063/1.104001.

[108] C. E. C. Wood, G. Metze, J. Berry, and L. F. Eastman. Complex free-carrier profile synthesis by "atomic-plane" doping of MBE GaAs. *Journal of Applied Physics*, 51 (1):383–387, January 1980. doi: 10.1063/1.327383. URL https://doi.org/10.1063/1.327383.

[109] Naoyuki Nakagawa, Mikk Lippmaa, Keisuke Shibuya, Hideomi Koinuma, and Masashi Kawasaki. Magnetic and transport properties of Mn-based fractional-layer oxide superlattices. *Japanese Journal of Applied Physics*, 41(Part 2, No. 3B): L302–L304, March 2002. doi: 10.1143/jjap.41.l302. URL https://doi.org/10.1143/jjap.41.l302.

[110] T. Mihara, K. Shibuya, T. Ohnishi, H. Koinuma, and M. Lippmaa. Transport properties of ultrathin oxide films and nanostructures. *Thin Solid Films*, 486 (1-2):63–66, 2005. ISSN 00406090. doi: 10.1016/j.tsf.2004.10.065. URL https://doi.org/10.1016/j.tsf.2004.10.065.

[111] A. Ohtomo and H. Y. Hwang. Surface depletion in doped $SrTiO_3$ thin films. *Applied Physics Letters*, 84(10):1716–1718, 2004. ISSN 00036951. doi: 10.1063/1.1668329. URL https://doi.org/10.1063/1.1668329.

[112] K. Nishio, M. Matvejeff, R. Takahashi, M. Lippmaa, M. Sumiya, H. Yoshikawa, K. Kobayashi, and Y. Yamashita. Delta-doped epitaxial La: $SrTiO_3$ field-effect transistor. *Applied Physics Letters*, 98(24):10–13, 2011. ISSN 00036951. doi: 10.1063/1.3600782. URL https://doi.org/10.1063/1.3600782.

[113] R. Ohtsuka, M. Matvejeff, K. Nishio, R. Takahashi, and M. Lippmaa. Transport properties of $LaTiO_3/SrTiO_3$ heterostructures. *Applied Physics Letters*, 96(19):3–6, 2010. ISSN 00036951. doi: 10.1063/1.3430006. URL https://doi.org/10.1063/1.3430006.

[114] T. Venkatesan, X. D. Wu, B. Dutta, A. Inam, M. S. Hegde, D. M. Hwang, C. C. Chang, L. Nazar, and B. Wilkens. High-temperature superconductivity in ultrathin films of $Y_1Ba_2Cu_3O_{7-x}$. *Applied Physics Letters*, 54(6):581–583, 1989. doi: 10.1063/1.101463. URL https://doi.org/10.1063/1.101463.

[115] D. Dijkkamp, T. Venkatesan, X. D. Wu, S. A. Shaheen, N. Jisrawi, Y. H. Min-Lee, W. L. McLean, and M. Croft. Preparation of Y-Ba-Cu oxide superconductor thin films using pulsed laser evaporation from high tc bulk material. *Applied Physics Letters*, 51(8):619–621, 1987. doi: 10.1063/1.98366. URL https://doi.org/10.1063/1.98366.

[116] A. Miotello and R. Kelly. Laser-induced phase explosion: new physical problems when a condensed phase approaches the thermodynamic critical temperature. *Applied Physics A*, 69(1):S67–S73, 1999. doi: 10.1007/s003399900296. URL https://doi.org/10.1007/s003399900296.

[117] M. R. Rashidian Vaziri, F. Hajiesmaeilbaigi, and M. H. Maleki. Monte Carlo simulation of the subsurface growth mode during pulsed laser deposition. *Journal of Applied Physics*, 110(4):043304, 2011. doi: 10.1063/1.3624768. URL https://doi.org/10.1063/1.3624768.

[118] S. Ohashi, M. Lippmaa, N. Nakagawa, H. Nagasawa, H. Koinuma, and M. Kawasaki. Compact laser molecular beam epitaxy system using laser heating of substrate for oxide film growth. *Review of Scientific Instruments*, 70(1):178–183, 1999. doi: 10.1063/1.1149562. URL https://doi.org/10.1063/1.1149562.

[119] T. Ohnishi and M. Lippmaa. RHEED intensity oscillation during oxide thin film growth. *Journal of Surface Science Society Japan*, 28(4):223–226, 2007. doi: 10.1380/jsssj.28.223. URL https://doi.org/10.1380/jsssj.28.223.

[120] Shuji Hasegawa. *Reflection High-Energy Electron Diffraction*, pages 1–14. 2012. ISBN 9780471266969. doi: 10.1002/0471266965.com139. URL https://onlinelibrary.wiley.com/doi/abs/10.1002/0471266965.com139.

[121] J.J. Harris, B.A. Joyce, and P.J. Dobson. Oscillations in the surface structure of Sn-doped GaAs during growth by MBE. *Surface Science Letters*, 103(1):L90 – L96, 1981. ISSN 0167-2584. doi: https://doi.org/10.1016/0167-2584(81)90682-4. URL http://www.sciencedirect.com/science/article/pii/0167258481906824.

[122] Mikk Lippmaa. Pulsed laser deposition and characterization of low-dimensional oxide structures. *Oyo Buturi*, 75(3):303–308, 2006. doi: 10.11470/oubutsu.75.3_303. URL https://doi.org/10.11470/oubutsu.75.3_303.

[123] T. Ohnishi, K. Shibuya, M. Lippmaa, D. Kobayashi, H. Kumigashira, M. Oshima, and H. Koinuma. Preparation of thermally stable TiO_2-terminated $SrTiO_3$(100) substrate surfaces. *Applied Physics Letters*, 85(2):272, 2004. ISSN 00036951. doi: 10.1063/1.1771461.

[124] M. Lippmaa, M. Kawasaki, A. Ohtomo, T. Sato, M. Iwatsuki, and H. Koinuma. Observation of $SrTiO_3$ step edge dynamics by real-time high-temperature STM. *Applied Surface Science*, 130-132:582 – 586, 1998. ISSN 0169-4332. doi: https://doi.org/10.1016/S0169-4332(98)00119-6. URL http://www.sciencedirect.com/science/article/pii/S0169433298001196.

[125] Growth of $La_2Ti_2O_7$ and $LaTiO_7$ thin films using pulsed laser deposition. *Journal of Crystal Growth*, 310(7):1985 – 1990, 2008.

[126] A. Ohtomo, D. A. Muller, J. L. Grazul, and H. Y. Hwang. Epitaxial growth and electronic structure of $LaTiO_x$ films. *Applied Physics Letters*, 80(21):3922–3924, 2002. ISSN 00036951. doi: 10.1063/1.1481767. URL https://doi.org/10.1063/1.1481767.

[127] S. M. Guo, Y. G. Zhao, C. M. Xiong, and P. L. Lang. Rectifying I-V characteristic of $LiNbO_3$/Nb-doped $SrTiO_3$ heterojunction. *Applied Physics Letters*, 89(22):223506, November 2006. doi: 10.1063/1.2393148. URL https://doi.org/10.1063/1.2393148.

[128] J. N. Lee, X. Hou, R. Takahashi, and M. Lippmaa. Tuning the carrier density in $SrTiO_3/LaTiO_3/SrTiO_3$ quantum wells. *Applied Physics Letters*, 116(17):171601, April 2020. doi: 10.1063/5.0006612. URL https://doi.org/10.1063/5.0006612.

[129] K. S. Takahashi, D. Matthey, D. Jaccard, J.-M. Triscone, K. Shibuya, T. Ohnishi, and M. Lippmaa. Electrostatic modulation of the electronic properties of Nb-doped $SrTiO_3$ superconducting films. *Applied Physics Letters*, 84(10):1722–1724, March 2004. doi: 10.1063/1.1667279. URL https://doi.org/10.1063/1.1667279.

[130] Yasuhide Tomioka, Naoki Shirakawa, Keisuke Shibuya, and Isao H. Inoue. Enhanced superconductivity close to a non-magnetic quantum critical point in electron-doped strontium titanate. *Nature Communications*, 10(1), February 2019. doi: 10.1038/s41467-019-08693-1. URL https://doi.org/10.1038/s41467-019-08693-1.

[131] Yeong Jae Shin, Claudia Lau, Sangjae Lee, Frederick J. Walker, and Charles H. Ahn. Surface-induced thickness limit of conducting La-doped $SrTiO_3$ thin films. *Applied Physics Letters*, 115(16):161601, October 2019. doi: 10.1063/1.5111771. URL https://doi.org/10.1063/1.5111771.

[132] Zhuoyu Chen, Hongtao Yuan, Yanwu Xie, Di Lu, Hisashi Inoue, Yasuyuki Hikita, Christopher Bell, and Harold Y. Hwang. Dual-Gate Modulation of Carrier Density and Disorder in an Oxide Two-Dimensional Electron System. *Nano Letters*, 16(10):6130–6136, 2016. ISSN 15306992. doi: 10.1021/acs.nanolett.6b02348. URL https://doi.org/10.1021/acs.nanolett.6b02348.

[133] René Meyer, Rainer Waser, Julia Helmbold, and Günter Borchardt. Cationic surface segregation in donor-doped $SrTiO_3$ under oxidizing conditions. *J. Electroceramics*, 9(2):101, 2002. ISSN 13853449. doi: 10.1023/A:1022898104375. URL https://doi.org/10.1023/A:1022898104375.

[134] A. Gentils, O. Copie, G. Herranz, F. Fortuna, M. Bibes, K. Bouzehouane, É Jacquet, C. Carrétéro, M. Basletić, E. Tafra, A. Hamzić, and A. Barthélémy. Point defect distribution in high-mobility conductive $SrTiO_3$ crystals. *Physical Review B*, 81(14): 144109, 2010. ISSN 1550235X. doi: 10.1103/PhysRevB.81.144109. URL https://doi.org/10.1103/PhysRevB.81.144109.

[135] Peter Y. Yu and Manuel Cardona. *Fundamentals of Semiconductors*. Springer Berlin

Heidelberg, 2010. doi: 10.1007/978-3-642-00710-1. URL https://doi.org/10.1007/978-3-642-00710-1.

[136] Y. Kozuka, Y. Hikita, C. Bell, and H. Y. Hwang. Dramatic mobility enhancements in doped $SrTiO_3$ thin films by defect management. *Applied Physics Letters*, 97: 012107, July 2010. doi: 10.1063/1.3457994. URL https://doi.org/10.1063/1.3457994.

[137] Dieter K. Schroder. *Semiconductor Material and Device Characterization*. John Wiley & Sons, Inc., April 2005. doi: 10.1002/0471749095. URL https://doi.org/10.1002/0471749095.

[138] L. F. Lou and W. H. Frye. Hall effect and resistivity in liquid-phase-epitaxial layers of HgCdTe. *Journal of Applied Physics*, 56(8):2253–2267, October 1984. doi: 10.1063/1.334259. URL https://doi.org/10.1063/1.334259.

[139] O. N. Tufte and P. W. Chapman. Electron mobility in semiconducting strontium titanate. *Physical Review*, 155:796–802, Mar 1967. doi: 10.1103/PhysRev.155.796. URL https://link.aps.org/doi/10.1103/PhysRev.155.796.

[140] A A Abrikosov. Quantum linear magnetoresistance; solution of an old mystery. *Journal of Physics A: Mathematical and General*, 36(35):9119–9131, aug 2003. doi: 10.1088/0305-4470/36/35/301. URL https://doi.org/10.1088%2F0305-4470%2F36%2F35%2F301.

[141] N.V. Kozlova, N. Mori, O. Makarovsky, L. Eaves, Q.D. Zhuang, A. Krier, and A. Patanè. Linear magnetoresistance due to multiple-electron scattering by low-mobility islands in an inhomogeneous conductor. *Nature Communications*, 3 (1), January 2012. doi: 10.1038/ncomms2106. URL https://doi.org/10.1038/ncomms2106.

[142] Kalon Gopinadhan, Young Jun Shin, Rashid Jalil, Thirumalai Venkatesan, Andre K. Geim, Antonio H. Castro Neto, and Hyunsoo Yang. Extremely large magnetoresistance in few-layer graphene/boron–nitride heterostructures. *Nature Communications*, 6(1), September 2015. doi: 10.1038/ncomms9337. URL https://doi.org/10.1038/ncomms9337.

[143] M. Diez, A. M.R.V.L. Monteiro, G. Mattoni, E. Cobanera, T. Hyart, E. Mulazimoglu, N. Bovenzi, C. W.J. Beenakker, and A. D. Caviglia. Giant Negative Magne-

toresistance Driven by Spin-Orbit Coupling at the $LaAlO_3$ /$SrTiO_3$ Interface. *Physical Review Letters*, 115(1):1–5, 2015. ISSN 10797114. doi: 10.1103/PhysRevLett.115.016803. URL https://doi.org/10.1103/PhysRevLett.115.016803.

[144] Chunhai Yin, Alexander E.M. Smink, Inge Leermakers, Lucas M.K. Tang, Nikita Lebedev, Uli Zeitler, Wilfred G. Van Der Wiel, Hans Hilgenkamp, and Jan Aarts. Electron Trapping Mechanism in $LaAlO_3$/$SrTiO_3$ Heterostructures. *Physical Review Letters*, 124(1):1–6, 2020. ISSN 10797114. doi: 10.1103/PhysRevLett.124.017702. URL https://doi.org/10.1103/PhysRevLett.124.017702.

[145] Younghyun Kim, Roman M. Lutchyn, and Chetan Nayak. Origin and transport signatures of spin-orbit interactions in one- and two-dimensional $SrTiO_3$-based heterostructures. *Physical Review B - Condensed Matter and Materials Physics*, 87 (24):1–11, 2013. ISSN 10980121. doi: 10.1103/PhysRevB.87.245121. URL https://doi.org/10.1103/PhysRevB.87.245121.

[146] Hiromoto Uwe, Ryozo Yoshizaki, Tunetaro Sakudo, Akio Izumi, and Takuya Uzumaki. Conduction band structure of $SrTiO_3$. *Japanese Journal of Applied Physics*, 24(S2):335, jan 1985. doi: 10.7567/jjaps.24s2.335. URL https://doi.org/10.7567%2Fjjaps.24s2.335.

[147] J. Biscaras, S. Hurand, C. Feuillet-Palma, A. Rastogi, R. C. Budhani, N. Reyren, E. Lesne, J. Lesueur, and N. Bergeal. Limit of the electrostatic doping in two-dimensional electron gases of $LaXO_3$(X = Al, Ti)/$SrTiO_3$. *Scientific Reports*, 4:1–7, 2014. ISSN 20452322. doi: 10.1038/srep06788. URL https://doi.org/10.1038/srep06788.

[148] Do Duc Cuong, Bora Lee, Kyeong Mi Choi, Hyo-Shin Ahn, Seungwu Han, and Jaichan Lee. Oxygen vacancy clustering and electron localization in oxygen-deficient $SrTiO_3$:LDA+U study. *Physical Review Letters*, 98(11), March 2007. doi: 10.1103/physrevlett.98.115503. URL https://doi.org/10.1103/physrevlett.98.115503.

[149] Chencheng Xu, Christoph Bäumer, Ronja Anika Heinen, Susanne Hoffmann-Eifert, Felix Gunkel, and Regina Dittmann. Disentanglement of growth dynamic and thermodynamic effects in $LaAlO_3$/$SrTiO_3$ heterostructures. *Scientific Reports*, 6(1), March 2016. doi: 10.1038/srep22410. URL https://doi.org/10.1038/srep22410.

[150] Shunsuke Kobayashi, Yuki Mizumukai, Tsuyoshi Ohnishi, Naoya Shibata, Yuichi Ikuhara, and Takahisa Yamamoto. High electron mobility of Nb-doped $SrTiO_3$ films stemming from rod-type Sr vacancy clusters. *ACS Nano*, 9(11):10769–10777, October 2015. doi: 10.1021/acsnano.5b05720. URL https://doi.org/10.1021/acsnano.5b05720.

[151] M. J. Veit, M. K. Chan, B. J. Ramshaw, R. Arras, R. Pentcheva, and Y. Suzuki. Three-dimensional character of the Fermi surface in ultrathin $LaTiO_3/SrTiO_3$ heterostructures. *Physical Review B*, 99:115126, Mar 2019. doi: 10.1103/PhysRevB.99.115126. URL https://link.aps.org/doi/10.1103/PhysRevB.99.115126.

Acknowledgments

Foremost, I would like to express my sincere gratitude to my advisor Prof. Mikk Lippmaa for the continuous support of my research and study. It was only due to his valuable guidance, patience, extensive knowledge, enthusiasm and consideration. I also owe him a great deal of emotional supports. He gave me many warm words of encouragement and comfort brightened me when I acutely need them. I admire Prof. Lippmaa not only as a true-scientist super-supervisor, but as a personal role model.

I would like to have Prof. Toshihito Osada, Dr. Kazuhito Uchida, Dr. Mitsuyuki Sato, Mr. Kenta Yoshimura to thank for helping back-gating measurement in their lab and useful discussions. I also owe thanks to Dr. Touru Yamauchi for many helps during using PPMS.

During these years I have also had the pleasure of collaborating with Mr. JeongRae Kim, Dr. Bongju Kim, Prof. Taewon Noh, Dr. Yoshihito Motoyui, Dr. Isao Ohkubo, and prof. Shik Shin. These are acknowledged as having given a valued contribution to my works.

I am grateful to Dr. Ryota Takanashi who never stopped challenging me and helping me to keep motivations for this two years. Non of this work would have been possible without his kind support. I also thank to prof. Yoshihiro Iwasa for valuable discussions, comments, and cares.

I also appreciate to our group member, Ms. Junko Nagayama, Ms. Junko Kawamura, Dr. Xiuyi Hou, Mr. Daiki Shono, Mr. Naoyuki Osawa, Dr. Mihee Lee, Dr. Seiji Kawasaki, Dr. Taizo Mori, Mr. Katsuya Kihara, Mr. Yoshihisa Hosokawa, Mr. Kodai Ogawa, Mr. Shuji Ezura, Mr. Xianming Yu, Ms. Hanako Kuramochi, Mr. Cong Wang, Dr. Takumi Ohtsuki, Dr. Enju Sakai, Mr. Alex Gwillim, Mr. Yuto Tsukahara, and Mr. Kaito Itou. The research life with them was really interesting and a valuable experience in my life. Each of them has an individual personality which always impressed me.

I sincerely appreciate the graduate school "MERIT" program coordinated by Prof. Masashi Kawasaki. The program gave me many valuable opportunities to communi-

cate with leading researchers and engineers working in industry, academia, and government. Each coursework, including camp, colloquiums, special lectures, joint-research, and internship in NEC helped me broaden my view and build deeper understanding of materials science.

I really would like to thank to all my friends in university of Tokyo, especially Yumi Hishinuma, Madoka Mochida, Nan Tang, Rie Mori, Ro-ya Liu, Sachiko Shinei, Kanako Takahashi, Ayuko Kobayashi, Ayumi Harasawa, Haruka Takizawam, prof. Hatsumi Mori, Yukiko Tan, Sachie Iimura, Kiwa Itoh, and ISSP office for their kind supports and encouragements. They stood by me when I was down and enrich my life in Kashiwa.

Finally, I would like to express my deepest gratitude to my family, ByoungHyun Lee and MyoungJa Choi; SeongGyun Lee, HakChan Lee, and JiSun Lee; Kazuhiro Noguchi and Fuyumi Noguchi; Koki Nakamura and Mizuho Nakamura. I express my sincire gratitude to my husband Ryo Noguchi for the endless support, sympathy and tolerance in all means.

July 2020
Kashiwa

Jiyeon N. Lee